NASA-TM-112826

IN-39-TM

PREDICTION AND VERIFICATION OF DUCTILE CRACK GROWTH FROM SIMULATED DEFECTS IN STRENGTH OVERMATCHED BUTT WELDS

A Thesis

Presented to

The Faculty of the Department of Materials Engineering

San José State University

In Partial Fulfillment

of the Requirements for the Degree

Master of Science

by

Owen S. Nishioka

May 1997

Sponsored by:

NASA-Ames Research Center
Moffett Field, California

Consortium #NCC2-5172

© 1997

Owen S. Nishioka

ALL RIGHTS RESERVED

APPROVED FOR THE DEPARTMENT OF MATERIALS ENGINEERING

Dr. Michael Lambert

Dr. Patrick Pizzo

Dr. Tina Panontin

To understand the answer,
one must first understand the question...

Abstract

Defects that develop in welds during the fabrication process are frequently manifested as embedded flaws from lack of fusion or lack of penetration. Fracture analyses of welded structures must be able to assess the effect of such defects on the structural integrity of weldments; however, the transferability of R-curves measured in laboratory specimens to defective structural welds has not been fully examined.

In the current study, the fracture behavior of an overmatched butt weld containing a simulated buried, lack-of-penetration defect is studied. A specimen designed to simulate pressure vessel butt welds is considered; namely, a center crack panel specimen, of 1.25 inch by 1.25 inch cross section, loaded in tension. The stress-relieved double-V weld has a yield strength 50% higher than that of the plate material, and displays upper shelf fracture behavior at room temperature. Specimens are precracked, loaded monotonically while load-CMOD measurements are made, then stopped and heat tinted to mark the extent of ductile crack growth.

These measurements are compared to predictions made using finite element analysis of the specimens using the fracture mechanics code Warp3D, which models void growth using the Gurson-Tvergaard dilitant plasticity formulation within fixed sized computational cells ahead of the crack front. Calibrating data for the finite element analyses, namely cell size and initial material porosities are obtained by matching computational predictions to experimental results from tests of welded compact tension specimens.

The R-curves measured in compact tension specimens are compared to

those obtained from multi-specimen weld tests, and conclusions as to the transferability of R-curves is discussed.

Acknowledgments

In the spring of 1993, I received my Bachelor of Science degree in Aerospace Engineering. At the time, I was employed at NASA-Ames Research Center through the San José State University Foundation College Cooperative Program. Having received my degree, it was time to move on - to either find a permanent position at NASA or find a job in the private sector. At this time, I was approached by who was then my acting branch chief. He proposed a third alternative: to remain in school, get my Master of Science degree, and stay at NASA in the NASA Student Career Experience Program. The rest, as they say, is history. I would like to thank Roy Hampton for presenting me with this opportunity, and all the people who made it possible for me to stay at NASA, including my current Branch Chief, Ron Mancini, Assistant Branch Chief, Paul Fusco, Group Leader, Tina Panontin, Student Programs Coordinator, Patricia Powell, and Graduate Advisor, Guna Selvaduray.

Of course, deciding to do a thesis and actually completing one are two completely different things. During the process of completing my thesis, I learned volumes about research, experimentation, and writing. I'd like to thank my thesis reading committee members: Chairman, Michael Lambert, Advisor, Patrick Pizzo, and Technical Advisor, Tina Panontin. They spent countless hours reading and rereading copies of my thesis, helping to improve and polish it to its final form, not to mention the many hours of assistance provided during planning and experimentation. I would also like to thank the personnel of the Failure Analysis and Materials Engineering Group who patiently listened to and critiqued my thesis presentation: Dan Dittman, Marc Rezin, Mickey Shanabarger, and Michael

Adamson.

Testing and research requires the efforts of many people, in the fabrication and preparation of test specimens. For their efforts in specimen fabrication, I would like to thank the NASA-Ames Machine Shop, including Shift Foremen, Bruce McMillan, Bob Stearns and Steve Cunningham, and Machinists Jesse Garibay, Robert Kornienko, Shawn Mesazros, and Lawrence Whiteside. I would also like to extend my appreciation to the NASA-Ames Test Engineering Laboratory personnel, including Frank Pichay and Lynn Hofland.

On a personal note, I would like to thank my parents, Richard and Hanae, my sister and brother, Cynthia and Alan, and my good friend Ann Keochinida. They provided me with emotional support when I was faced with what seemed like insurmountable problems, stayed out of my way (most of the time) when I was rushing to get things completed, and most of all, gave me the encouragement I needed to finish. I would also like to thank Wei Lin and Marc Rezin who brought me food on more than one of those long nights, reminding me how important it is to eat once in a while.

I would like to extend my thanks to NASA which funded this research under the research program "Life Prediction Methodology for High Toughness Metal Structures" and a university consortium agreement with San José State University. Last but not least, I would like to thank George Kidwell, Jr., who provided computational resources on the NASA-Ames Research Center Aeronautics Consolidated Supercomputing Facility Cray YMP-C90.

Table of Contents

Page

Abstract i
Acknowledgments iii
Table of Contents v
List of Figures vii
List of Tables xii
Introduction 1
1.1 Weld Defects 4
1.2 Modeling of Cracks 7
1.3 Effects of Inhomogeneity 12
1.4 Effects of Constraint 13
1.5 Additional Problems 14
1.6 Research Focus 15
1.7 Thesis Overview 16
Terminology 18
Previous Work 22
3.1 Finite Element Modeling 22
3.1.1 Bilinear Material Model 23
3.1.2 Power Law Hardening Material Model 25
3.1.3 Piecewise Linear Material Model 26
3.2 Micromechanics of Ductile Crack Growth 26
3.2.1 Rice-Tracey Model 28
3.2.2 Stress Modified Critical Strain Model 30
3.2.3 Gurson-Tvergaard Void Growth Model 32
3.3 Problems with Micromechanical Void Growth Models 35
3.4 Finite Elements and Micromechanics 37
3.4.1 Warp3D 37
3.4.2 Warp3D and Fracture Specimens 38
3.5 Consideration of Weld Inhomogeneity 38
3.6 Modeling Cracks in Welds 40
3.7 Characteristic Length for Ductile Fracture 42
Objectives and Approach 45
4.1 Objectives 45
4.2 Approach 45
Experimentation 48
5.1 Test Specimen Design 48
5.2 Materials Selection 49
5.2.1 A516 Grade 70 Steel 50
5.2.2 E7018 Weld Rod 50
5.3 Weld Fabrication 50
5.4 Specimen Fabrication 52

5.5 Tensile Testing....54
5.5.1 Specimens....54
5.5.2 Testing Procedures....55
5.5.3 Test Results....57
5.6 Single Edge Cracked Bend Specimen Testing....59
5.6.1 Specimens....59
5.6.2 Testing Procedures....61
5.7 Compact Tension C(T) Testing....63
5.7.1 Specimens....63
5.7.2 Testing Procedures....64
5.8 Center Cracked Panel M(T) Specimens....67
5.9 Center Cracked Panel M(T) Specimen Testing....72
5.10 Microscopy....74
Finite Element Modeling....77
6.1 Finite Element Software....77
6.2 Modeling Software....78
6.3 Material Stress-Strain Properties....78
6.4 Element Sizing (The Material Characteristic Length)....83
6.4.1 Metallographic and Fractographic Method....83
6.4.2 Stress Modified Critical Strain Method....85
Finite Element Analysis Calibration and Experimental Results....101
7.1 Two Dimensional Modeling....102
7.2 Compact Tension (CT) Model....103
Experimental Results and Verification....112
8.1 Analysis....112
8.2 Results....118
Summary, Conclusions, and Discussion....122
9.1 Summary....122
9.2 Conclusions....123
9.3 Discussion....125
9.3.1 Fabrication....125
9.3.2 Experimentation....125
9.3.3 Finite Element Modeling....127
9.4 Further Study....128
Reference List....130
Appendix A: Test Specimen Design....136
Appendix B: Tension Plus Bending Specimen Design....141
Appendix C: Warp3D Parameters....144

List of Figures

Figure — Page

1 Unitary Plan Wind Tunnel Complex - Three test sections provide researchers with all aspects of flight from subsonic to supersonic regimes 2

2 The original 12 Ft. Pressurized Wind Tunnel - Reopened in August 1995 after being torn down and rebuilt, the 12 Ft. PWT is used for supersonic flight research 3

3 a) Butt weld schematic. b) Cross section of butt weld showing heat affected zone (light gray) and base metal (dark gray) 5

4 Butt weld lack of penetration defect. In this defect, the base metal is not melted through the thickness 6

5 Butt weld lack of fusion defect. In this defect, the weld metal is flowed onto the base metal, instead of mixing with it 7

6 Effects of plasticity on crack tip stresses. L is the characteristic structure length and r is the crack tip radius. HRR refers to the elastic-plastic crack tip stress-strain solution of Hutchinson, Rice, and Rosengren 8

7 Infinite cracked plate 9

8 J-Integral resistance curve for a ductile material 11

9 CTOD-Resistance curve. Crack initiation occurs at 0.2 mm offset. 11

10 Minimum separation distance, x, between the fusion line and the crack tip allowing for homogeneous treatment of weld heat affected zone 13

11 Definition of crack aspect ratio. 14

12 Typical stress-strain curves for steel. (a) brittle, lower shelf and (b) ductile, upper shelf 24

13 Bilinear stress strain curve 24

14 Bilinear modeling of typical steel stress-strain curves. (a) brittle, lower shelf, and (b) ductile, upper shelf. 25

15 Power law hardening stress-strain curve **25**

16 Eight segment piecewise linear stress-strain curve **26**

17 Nucleation and coalescence of voids from inclusions and second phase particles **27**

18 SMCS failure criterion **31**

19 Failed length of cells as predicted by the stress modified critical strain void coalescence model **32**

20 Coalescence of initially spherical voids, results in loss of spherical appearance per Becker, et al **36**

21 Definition of material characteristic distance and process zone size **42**

22 Experimental approach flow chart **46**

23 Weld preparation guidelines for weld specimens **52**

24 Welded plate specimen layout **53**

25 Smooth weld metal tensile specimen **55**

26 Notched tensile specimens **55**

27 Tensile Round-Bar Test Setup **56**

28 Base metal true stress-strain curves with Bridgman correction factor applied **57**

29 Weld true stress-strain curves with Bridgman correction factor applied **58**

30 Shallow notched single edged bend specimen **60**

31 Deep notched single edged bend specimen **60**

32 Location of knife edges on single edged bend specimens **61**

33 single edged bend testing setup. Deep notched specimen shown **62**

34 Compact tension C(T) specimen **65**

35 Compact tension test setup **66**

36 Center cracked panel specimen for tension loading **67**

37 Center cracked panel specimen for tension plus bending loading.....**68**

38 Longitudinal and circumferential butt welds in the Unitary Pressurized Wind Tunnel at NASA-Ames Research Center.....**69**

39 Stress due to bending in circumferential butt welds near ring supports.....**70**

40 Position of strain gages on center cracked panel specimens. b) Measurement Group Precision Strain Gages of type EP-08-062AQ-350.....**72**

41 Center cracked panel test setup.....**73**

42 Weld micrograph showing hard particle (carbide) inclusions.....**75**

43 Weld grain structure after etching with 5% Nital.....**76**

44 Small notched round-bar tensile specimen.....**80**

45 Large notched round-bar tensile specimen.....**80**

46 Comparison of stress-strain experimental and analytical results for small notched specimens.....**81**

47 Comparison of stress-strain experimental and analytical results for large notched specimens.....**81**

48 Base metal piecewise linear flow curve used in finite element analysis, adjusted for element stiffening. Original experimental data shown for reference.....**82**

49 Weld metal piecewise linear flow curve used in finite element analysis, adjusted for element stiffening. Original experimental data shown for reference.....**82**

50 Fracture surface showing large (20 μm) inclusions surrounded by uniform smaller (2 μm) inclusions.....**84**

51 Weld metal failure criterion - equivalent plastic strain vs. triaxiality.....**86**

52 Deep notched (a/W = 0.7) SE(B) specimen model.....**88**

53 Micrograph of deep notched (a/W=0.7) SE(B) specimen showing fracture initiation. Specimen loaded to CMOD of 0.09 inches (2.3 mm), resulting in a load of123 pounds (55.8 kg).....**89**

54 Crack mouth opening displacement for deep notched (a/W=0.7) SE(B) specimens **90**

55 Compensation technique for knife edges not located on front-face. Rotation/location of circled nodes determines position of knife edge via vector a-b. **91**

56 Determination of weld metal characteristic material length through deep notched (a/W=0.7) SE(B) analysis. Curves represent increasing load **92**

57 Deep notched (a/W=0.7) SE(B) "Zero Crossing" as a function of CMOD. Used for verification of weld metal characteristic length **93**

58 Deep notched (a/W=0.7) SE(B) model: a) undeformed geometry. b) geometry after application of 118.33 pounds (53.68 kg) **94**

59 Shallow notched (a/W = 0.3) SE(B) specimen model **95**

60 Determination of weld metal characteristic material length through shallow notched (a/W=0.3) SE(B) analysis. Curves represent increasing CMOD or load **96**

61 Shallow notched (a/W=0.3) SE(B) "Zero Crossing" as a function of CMOD. Used for preliminary SMCS determined weld metal characteristic length. **97**

62 Micrograph of shallow notched (a/W=0.3) SE(B) specimen showing fracture initiation. Specimen loaded to a CMOD of 0.034 inches (0.86 mm), resulting in a load of 644 pounds (292.1 kg) **98**

63 Shallow notched (a/W=0.3) SE(B) model: a) undeformed geometry. b) geometry after loading to a CMOD of 0.018 inches (0.46 mm) **99**

64 Crack mouth opening displacement for shallow notched (a/W=0.3) SE(B) specimens **100**

65 Compact tension specimen model. **104**

66 Compact tension model: a) The parent metal, weld, and load application regions were assigned different material properties, as indicated by the shaded regions. b) The actual specimen end-view, etched with 5% Nital to reveal location of crack plane in weld. Line indicates modeled fusion line **105**

67 Crack tip opening displacement at initiation, based on 90° included angle method **106**

68 J-Integral area integration method. **109**

69 Weld metal J-R curve comparison of analysis and test results J-R curve for A516 Steel (f0=0.002) shown for comparison **109**

70 Compact tension crack mouth opening displacement vs. load **110**

71 Compact tension predicted crack front superimposed on actual fracture surfaces of three C(T) specimens. Conditions: a) J = 4,645 psi-in. (813.5 KPa-m), b) J = 8,923 psi-in (1,562.7 KPa-m) **111**

72 Center cracked panel tension specimen model **113**

73 Center Cracked Panel: a) The parent metal, weld, and load application regions were assigned different material properties, as indicated by the shaded regions. b) The actual specimen face-view, etched with 5% Nital to reveal location of the in weld crack plane. Lines indicate modeled fusion line **114**

74 Load - CMOD relationship for single material, tension loaded center cracked panel **115**

75 Determination of η factor for single material, tension loaded center cracked panel **116**

76 J-Resistance curve for tension loaded center cracked panel and compact tension specimen **117**

77 Center cracked panel tension CMOD results comparison **119**

78 Center cracked panel tension strain results comparison. Warp3D strain extracted from average strain over elements associated with strain gage location **119**

79 Center cracked panel predicted crack front superimposed on actual fracture surfaces. a) Fatigue cracked front, 0.04 inch (1.01 mm) CMOD, b) EDM notched crack front, 0.045 inch (1.14 mm) CMOD, c) EDM notched crack front, 0.06 inch (1.52 mm) CMOD. **121**

A-1 Tensile Round Bar Specimen **136**

A-2 Single edged bend specimen - deep notch **137**

A-3 Single edged bend specimen - shallow notch **138**

A-4 Compact tension specimen **139**

A-5 Center cracked panel tension specimen **140**

B-1 Center cracked panel tension plus bending specimen model **142**

B-2 Center cracked panel tension plus bending specimen **143**

List of Tables

Table Page

1 Material chemical requirements. 50

2 Required properties for analysis using Gurson-Tvergaard Model. 54

3 Fatigue precracking requirements for SE(B) specimens. 62

4 Fatigue precracking requirements for C(T) specimens. 66

5 Crack growth and weld material parameters for Warp3D model. 118

C-1 Crack growth and weld material parameters for Warp3D model. 144

C-2 Material true stress-strain curves. 145

Chapter 1

Introduction

What are the mechanical properties of a structural material? Most engineers, regardless of discipline will give the textbook response; that materials are isotropic, monolithic, homogeneous, and defect free. This would suggest that materials exhibit strength characteristics that are easily measured by uniaxial testing only. In addition, it may be implied that materials are single blocks, consisting of a single phase, and do not vary throughout the continuum. These assumptions are made for the sake of simplicity, but they cover a deeper truth.

In reality, all materials are complex structures. Although they can be approximated as isotropic due to their polycrystallinity, real materials are hardly ever fully isotropic and can have very different properties depending on orientation. They are hardly ever monolithic, usually consisting of many grains oriented in random directions. Finally, they are never entirely homogeneous, but instead may contain defects, impurities, discontinuities, and cracks.

Fabrication of metal structures often involves welding which introduces another interesting piece to the already complex puzzle. The process of welding adds several additional "degrees of freedom" to the material configuration which directly affect the material mechanical properties. Inclusions, such as weld slag can be contained in the weld, as can gas porosities and other debris. Improper welding techniques can result in mismatch of the weld land, for example, further increasing the probability of defects arising in the welds. Cracks that initiate at these weld defects are the subject of this study.

A quick tour of NASA-Ames Research Center in Mountain View would

reveal a large number of welded structures, to even the most casual observer. Large scale wind tunnels, pressure spheres, and high-pressure tank farms cover much of the real estate of the Center. The loss of any of these facilities, either in the form of catastrophe or down time for repair can lead to extreme losses in terms of both economics and research opportunity. For example, pictured in Figure 1 is the Unitary Plan Wind Tunnel (UPWT), a highly utilized facility that includes three test sections that simulate nearly all aspects of flight, ranging from the subsonic to the supersonic regimes. This facility was shut down for three years, starting in October of 1994. The purpose of the shutdown was partly to facilitate a massive overhaul effort to repair the more than 10 miles (16 km) of butt welds contained in the structure. The total cost to repair the facility: 8 million dollars.

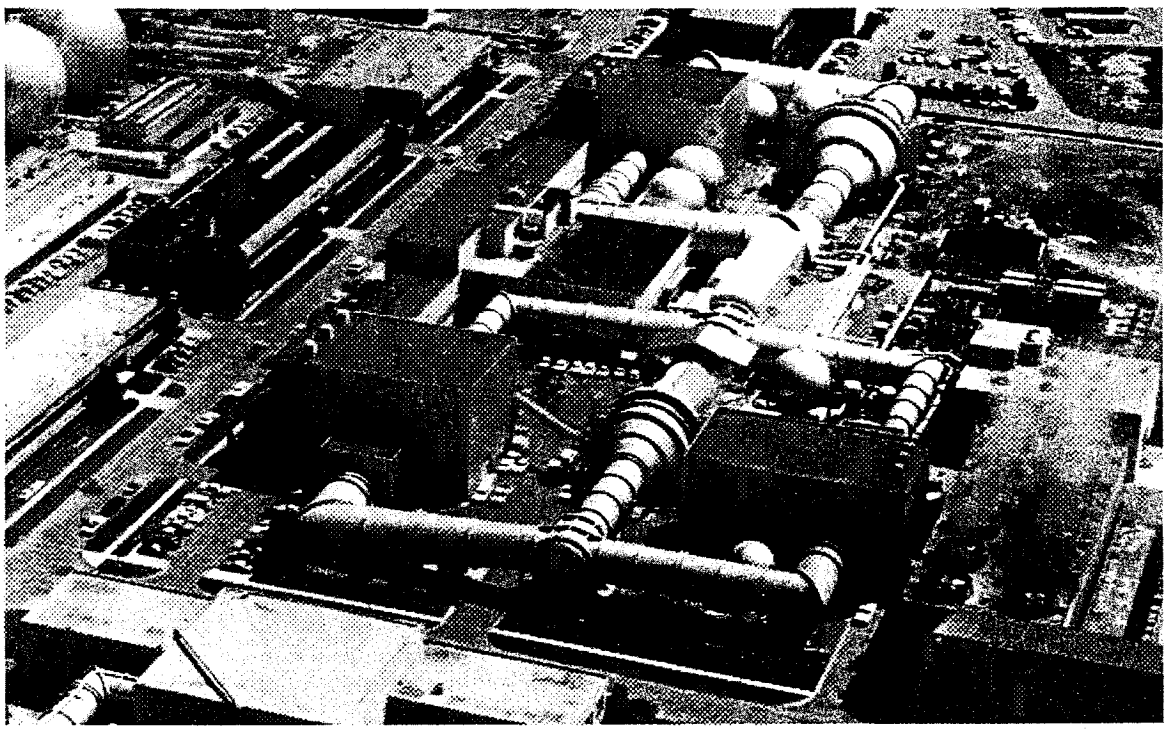

Figure 1: Unitary Plan Wind Tunnel Complex - Three test sections provide researchers with all aspects of flight from subsonic to supersonic regimes.

In another section of the Center is the 12 Foot Pressurized Wind Tunnel (PWT) shown in Figure 2. Opened in 1946, it was designed to operate at pressures up to six atmospheres (608 kPa gage) in order to conduct supersonic flight research. However due to safety concerns, in 1976 the certified operating pressure was derated to 5 atmospheres (506 kPa gage) for fear of catastrophic failure of the tunnel shell. In the event of a breach while operating the 12 Foot PWT at its original design pressure, it was estimated that the resulting blast would be equivalent to the detonation of 2000 pounds (900 kg) of TNT.[26] Minor structural damage, such as broken windows, would occur to a distance of 2 miles (3.2 km) from the blast site. It was also decided to continually decrease the operating pressure over the remaining life, thereby drastically reducing the usefulness of the facility.

The 12 Foot Pressurized Wind Tunnel was returned to service in August

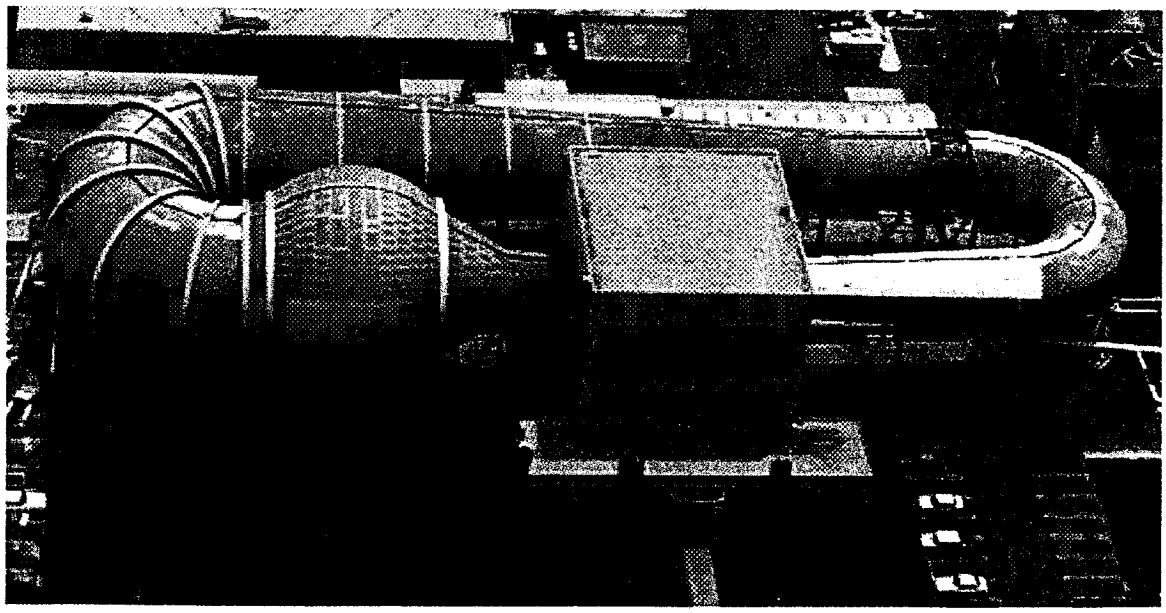

Figure 2: The original 12 Ft. Pressurized Wind Tunnel - Reopened in August 1995 after being torn down and rebuilt, the 12 Ft. PWT is used for supersonic flight research.

1995, after being completely demolished and rebuilt. The need to rebuild was partly a function of the poor quality of the materials used during its original construction. A second driving force, however, was a lack of confidence in the ability to identify and repair all of the defects in the welds. For example, one defect identified prior to its dismantling was a large crack measuring 114 inches (2.9 m) in length.

Both of the tunnels sited in the examples have served NASA for many years, the UPWT having begun operations in 1956, and the 12 Foot PWT having opened in 1946. The main drivers behind the repairs to both tunnels was the uncertainty in conventional fracture mechanics predictions of remaining structural life under fatigue loading and a need for recertification of the tunnels for another 30 year period. A large part of this uncertainty results from problems in applying data from laboratory testing to the actual complex structure in service.

1.1 Weld Defects

The joining of two plates can be accomplished in a number of ways, but a typical method involves welding, wherein heat is applied causing localized melting of the base metal. Butt welds are formed when two plate ends are "butted" up against one another. The addition of metal from a welding rod fills in the space between the two plates and makes for a very strong connection. The types of welds used in construction of pressure vessels are typically full penetration overmatched butt welds like the one shown schematically in Figure 3. Full penetration indicates that weld metal is continuous through the thickness of the plate.

The weld metal used can either be stronger, weaker, or have the same

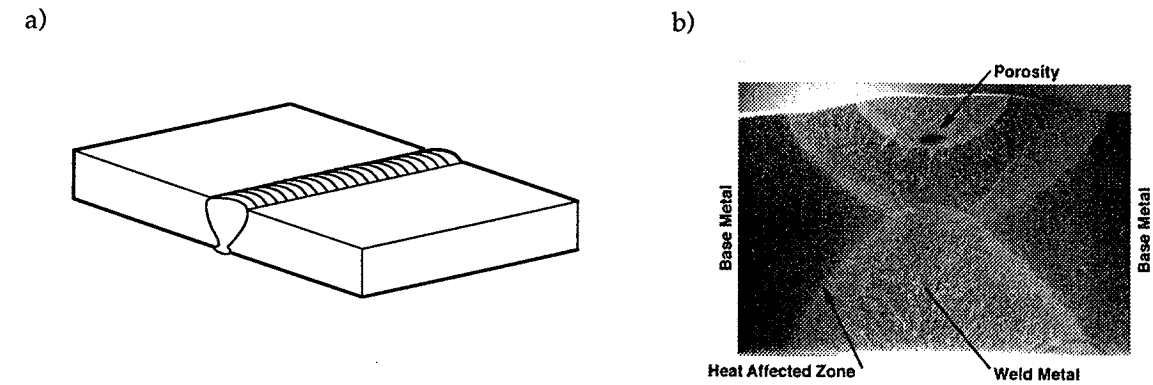

Figure 3: a) Butt weld schematic. b) Cross section of butt weld showing heat affected zone (light gray) and base metal (dark gray).

strength as the base metal. If the weld metal has strength characteristics stronger than the base metal, then the weld is said to be overmatched. Many welding codes require the use of overmatched weld material since the stronger weld metal prevents large deformations in the weld and forces plastic deformation into the lower strength base metal, where better fracture resistance and fewer defects can be expected.[31] Overmatching, however, is not the end all solution as there are significant technical and economic factors which must be considered. The welding of high strength steels with overmatched weld metal, for example, requires preheating to prevent hydrogen cracking, which decreases weld metal deposition rate and increases the lack of fusion/lack of penetration defect rate. These effects tend to significantly increase welding time and therefore cost, and the higher defect rate can necessitate large amounts of weld repair.

Weld undermatching occurs when the weld metal is weaker than the base metal. In contrast to overmatching, undermatching leads to more deformation and consequently, increased strain in the weld region when a welded component is loaded. This provides a larger applied driving force for crack extension in the weld region. For this reason, most codes do not allow weld undermatching.

However, unlike overmatched welds, undermatched welds are easier to prepare, do not require preheating, and have a lower lack of fusion/lack of penetration defect rate.[31]

Matched welds occur in situations where the strength of the base and weld metals are identical. For the same reasons as undermatched welds, this type of welding is often avoided, especially in applications where deformation in the weld would be undesirable. Due to degradation of mechanical properties in the weld region, matched welds inevitably lead to deformation concentrating at the weld.

A large number of different types of problems can occur whenever two materials are welded together. The principal defect of interest in this study is the incomplete or lack of penetration (LOP) defect. In this type of defect shown in Figure 4, the base metal has not been completely melted, leading to the formation of a discontinuity between the edges of the base metal at the root of the weld. This discontinuity acts as a stress concentration which promotes the formation of cracks.

Another important defect is the lack of fusion (LOF) defect depicted in Figure 5. This generally occurs when the hot weld metal is deposited on unheated base metal. A substandard bond forms which easily leads to cracking.[27]

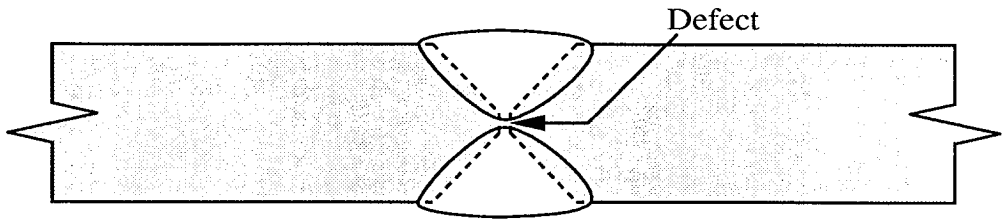

Figure 4: Butt weld lack of penetration defect. In this defect, the base metal is not melted through the thickness.

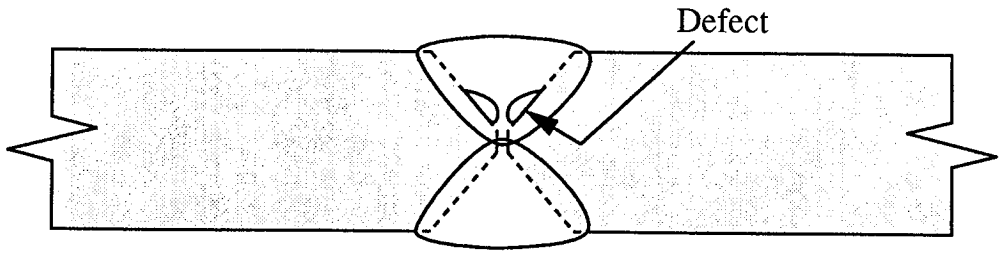

Figure 5: Butt weld lack of fusion defect. In this defect, the weld metal is flowed onto the base metal, instead of mixing with it.

1.2 Modeling of Cracks

Extensive effort has gone into the modeling of cracks and predicting ductile crack growth in engineering structures. Standard methods employ single parameter, geometry independent parameters such as stress intensity, *K*, the J-integral, *J*, and Crack Tip Opening Displacement, CTOD, to predict ductile crack growth.

Figure 6 illustrates the relative accuracy and applicability limits of linear-elastic fracture mechanics (LEFM) and elastic-plastic fracture mechanics (EPFM) in the prediction of fracture. The standard linear elastic fracture mechanics (LEFM) approach utilizes the Mode I, crack-tip, stress-intensity factor, K_I. For the simple case of an infinite plate under tension, with a crack in the center, as shown in Figure 7, the Mode I Stress intensity is:

$$K_I = \sigma\sqrt{\pi a} \tag{1}$$

where a is the crack length and σ is the far field stress in the plate. The load when fracture occurs can be easily determined by comparing the stress intensity factor with the fracture toughness, K_{Ic}, of the material. The fracture toughness is a

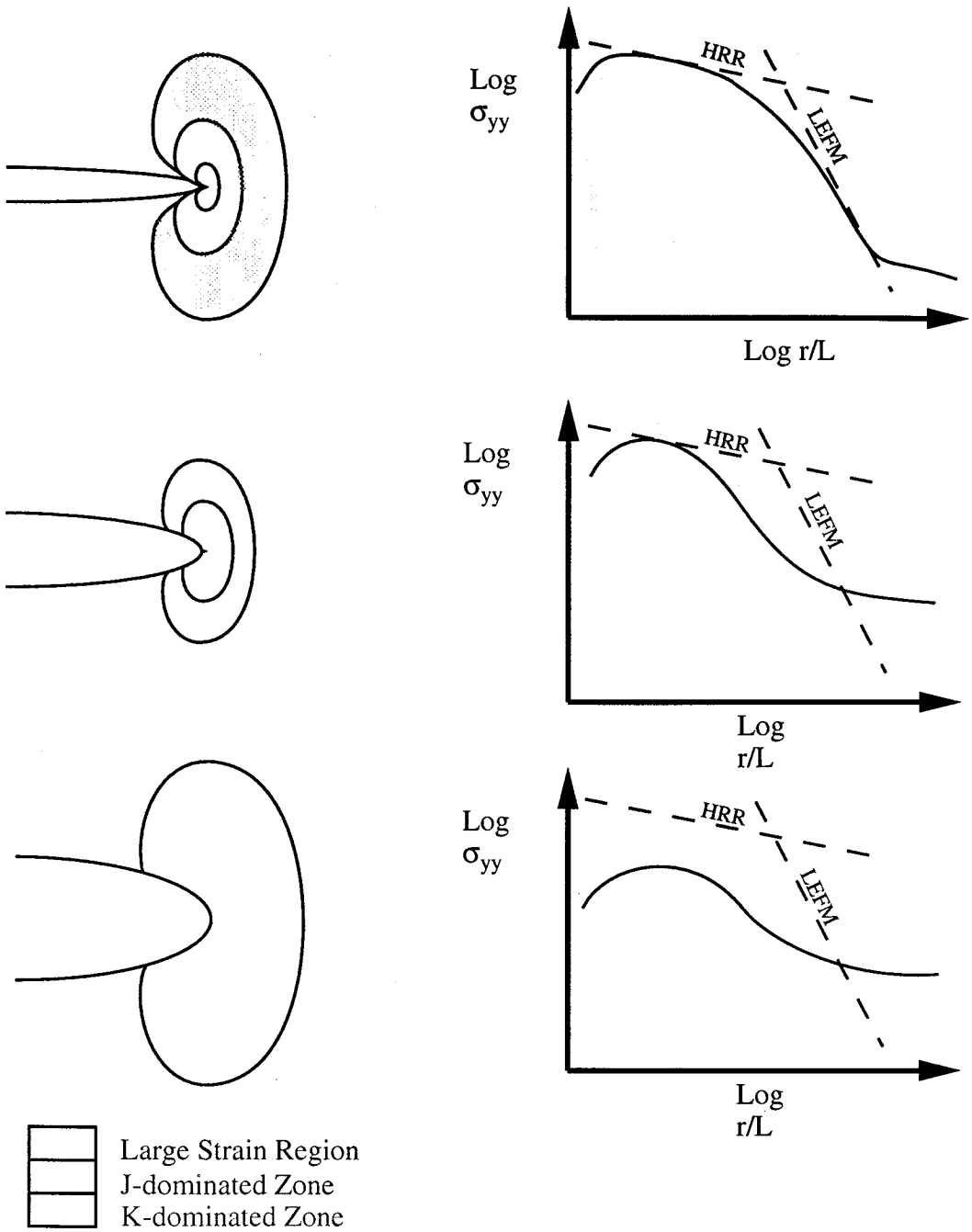

Figure 6: Effects of plasticity on crack tip stresses.[2] *L* is the characteristic structure length and *r* is the crack tip radius. HRR refers to the elastic-plastic crack tip stress-strain solution of Hutchinson, Rice, and Rosengren.

material property and not geometry dependent when crack tip plasticity is low (plastic zone « W, b_0). Under such conditions, LEFM produces good results as

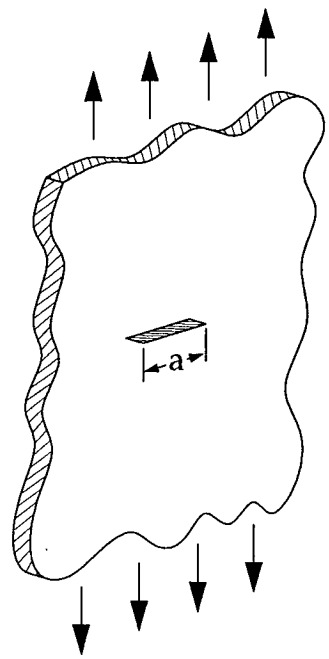

LEFM

$$K_I = \sigma\sqrt{\pi a}$$

$$J = \frac{K^2(1-\upsilon^2)}{E}$$

Figure 7: Infinite cracked plate.

shown in the K-dominated case at the top of Figure 6.[4,8]

One of the limitations of LEFM arises from the assumption that the stresses at the crack tip are infinite. However, the maximum stress in a material is limited by the material's yield strength such that instead of infinite stress, plastic deformation occurs. When crack tip plasticity becomes significant, the accuracy of fracture predictions with LEFM decreases. In this case, either the J-integral or CTOD approaches may be utilized. Both of these single parameter approaches provide good results under fully contained plasticity or small scale yielding, as illustrated in the middle of Figure 6. Small scale yielding, or "fully contained" plasticity occurs when plasticity is small compared to the ligament and has not reached a free surface. Generally, these conditions are met as long as the plastic zone is 50 times smaller than the specimen dimensions.[2]

As shown at the top of Figure 6, when the plastic zone is small, K (LEFM)

and J (EPFM) accurately predict the magnitude of crack tip stresses and strains. As crack tip plasticity increases, the K dominated zone disappears and LEFM no longer predicts the state of stress at the crack tip (Figure 6, center), while the region of applicability for J decreases. At even larger strains, large scale plasticity dominates and neither J nor K predict the stresses present at the crack tip (Figure 6, bottom).

The J-integral is similar to the stress intensity factor, K_I, except it more accurately predicts stresses and strains nearer to the crack tip, and under conditions where the plastic zone is larger than allowed in LEFM. In addition, through the use of a J-resistance (J-R) curve, the J-integral is used to determine the resistance to fracture during monotonic quasi-static loading. These predictions for the amount of stable ductile crack growth and critical crack length are much closer to observed behavior than those obtained through LEFM for upper shelf, high toughness materials. This is primarily a result of including the reduction of stress at the crack tip due to local plasticity in the J-integral approach. The initiation of stable crack extension occurs when the J-R curve deviates from linearity. Since the actual location of this deviation may be difficult to measure, fracture initiation is considered to occur based on a 0.008 inch (0.2 mm) crack tip opening offset. This is shown schematically in Figure 8, with the initiation J value, J_{Ic}.

A third approach used to model cracks and predict crack growth is the CTOD method. The basis of the CTOD approach is that the crack tip stress field and crack extension can be determined by the crack tip opening displacement. Shih has shown that there is a unique relationship between J and CTOD for a given material under elastic-plastic conditions:[2]

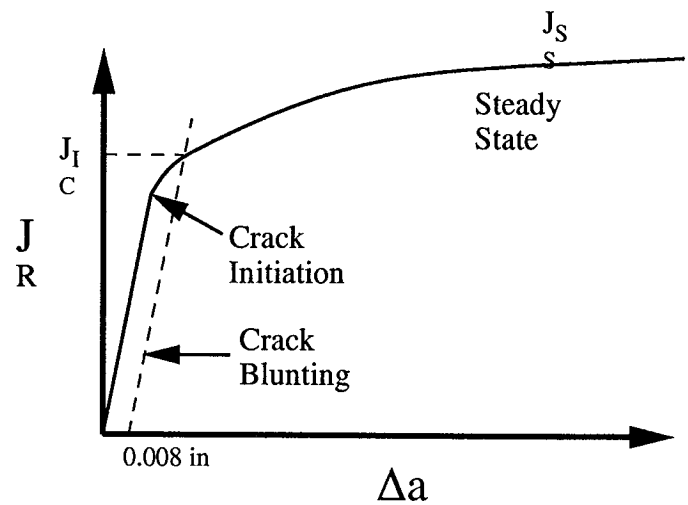

Figure 8: J-Integral resistance curve for a ductile material.

$$J = m\,\sigma_{ys}\,\delta \tag{2}$$

where m is a constraint factor equal to 2.0 for plane strain,[12] δ is the crack tip opening displacement, and σ_{ys} is the material yield stress, determined from uniaxial testing. A schematic CTOD resistance curve is shown in Figure 9. In comparison to the J-resistance curve of Figure 8, the CTOD-resistance curve is shallower and does not demonstrate as sharp a change in the performance variable at the onset of crack initiation. The change in crack length or crack extension, Δa,

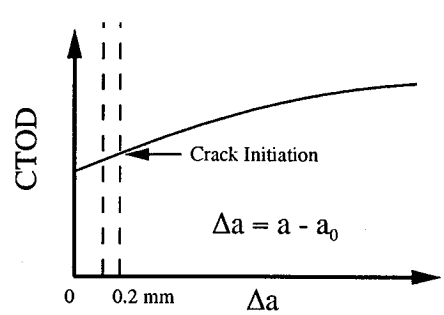

Figure 9: CTOD-Resistance curve. Crack initiation occurs at 0.2 mm offset.

is the same as it was defined for the J-resistance curve, namely the difference between the final and initial crack lengths.

1.3 Effects of Inhomogeneity

All of these single parameter methods, the stress intensity factor, the J-integral, and the crack tip opening displacement, are defined for homogeneous structures. The difficulty in modeling crack growth in welds is that welds, by their very nature, are inhomogeneous. As shown in Figure 3b, the weld consists of three regions: the base metal, weld metal, and the heat affected zone (HAZ). Although the base metal is homogeneous, the weld metal in the HAZ is never homogenous and usually has properties that vary across the weld. Even under simplifying assumptions of homogeneity in the HAZ, the weld and base metals will exhibit different properties, thereby making the entire weld inhomogeneous. ASTM Standard E813[10] provides a standard method for measuring J_{Ic}, although it is generally applied to homogeneous materials.

The effects of weld inhomogeneity on ductile crack growth were studied by Kirk, et al.[31] From analytical models, the minimum distance between the crack tip and the fusion line, above which the effects of HAZ inhomogeneity are negligible and can therefore be ignored, was determined.[31] The minimum distance, x, for a lack of penetration (LOP) defect, such as the one shown in Figure 4, is indicated in Figure 10. Figure 10 illustrates the separation distance, x, as the shortest distance between the fusion line and the crack tip. Kirk, et al. demonstrated that if the distance from the crack tip to the weld/base metal interface is large enough, there is minimal deviation between the analytical solutions for overmatched welds and bimetal plates.

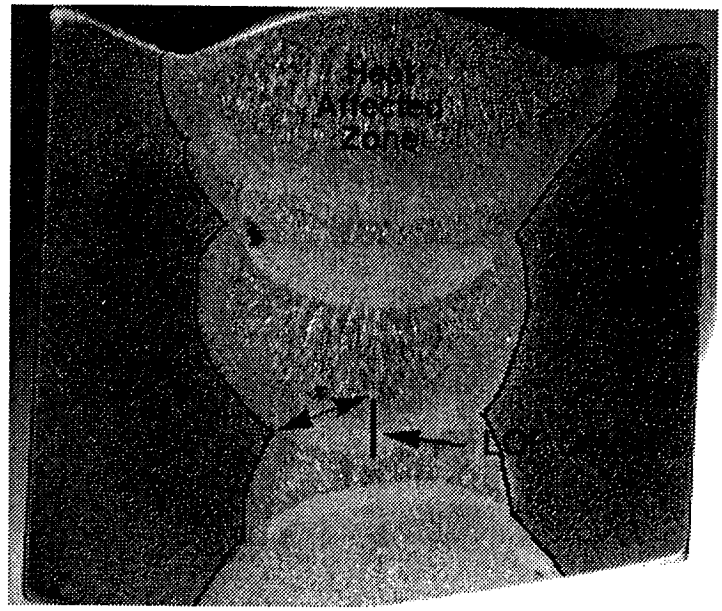

Figure 10: Minimum separation distance, *x*, between the fusion line and the crack tip allowing for homogeneous treatment of weld heat affected zone.

1.4 Effects of Constraint

Another problem with the various single parameter approaches lies in the fact that even before the crack propagates, the stress state, which may be strongly geometry dependent, changes, especially as the crack approaches the free surface of the material.[50,51,52] The crack aspect ratio is defined as the ratio of the crack length to the plate width, as shown in Figure 11. As the crack approaches the free surface, plasticity is no longer "fully contained." Under these conditions, stresses in the plastic zone decrease and tend toward plane stress conditions. This is true, whether the crack is an internal crack growing towards the surface (large a/W) or a small crack growing in from the surface (small a/W). For surface cracks, Sorem[51] has shown that in ductile materials, the CTOD can be as much as 2.5 times larger for a crack with an aspect ratio of 0.15 versus 0.5 at the same crack tip

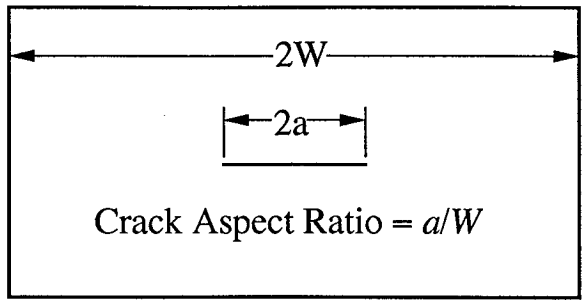

Figure 11: Definition of crack aspect ratio.

stress state, due to the loss of constraint in the short crack specimen. Geometry dependence of toughness is one of the reasons why single parameter approaches cannot be applied to structures such as wind tunnels, and makes the basis for part of this study.

1.5 Additional Problems

There are many other problems in creating accurate models of cracks that reflect reality in welded structures. Aside from general fabrication defects, such as those mentioned previously, there are many other types of defects that can be found in welded structures. Some of these can be easily modeled, while others are much more difficult.

A common problem, especially where automated welding is utilized is the offset or mismatched weld defect. This defect is a gross defect that occurs when the two plates to be welded are not initially aligned.

Other more common defects are slag and tungsten inclusions, gas porosities, voids, and various types of contamination, such as hydrogen or even dirt.

Although butt welds make up a large proportion of the welds found in pressure vessels, there are many other types of welds that are equally susceptible

to cracking. For example, support structures are often connected to the vessel using fillet welds, or combination fillet-butt welds. These configurations are equally difficult to model and to test.

Residual stresses related to welding can also influence crack extension, and must be modeled if they are present. These stresses, which result from localized heating and non-uniform cooling, can alter the ability of a crack to extend, depending on whether the crack is located in a residual compressive or tensile field. Compressive residual stresses, generally located near the middle of a weld, serve to retard crack growth. Conversely, near the surface, where residual stresses are predominantly tensile, crack growth is increased. Normalizing welds after welding can serve to reduce the effects of residual stresses on crack growth.

1.6 Research Focus

The focus of this research is to extend and test an existing finite element analysis methodology for predicting ductile crack growth in strength overmatched, defective butt welds. Research will include the modeling of ductile crack growth from cracks originating from lack of penetration defects in butt welded geometries. Crack mouth opening displacement (CMOD) will be determined as a function of load and crack extension. Laboratory testing will provide fundamental material constants that will be utilized by the modeling software.

Laboratory testing of standard geometries, such as compact tension specimens will then be used to calibrate the parameters of the finite element model. The calibrated model will then be applied to a structural configuration and experimentally verified through additional laboratory tests. From this information, limitations of the methodology and its applicability to real structures will

be determined.

Once the methodology developed here has been proven, the ability to use properties obtained from laboratory testing to model full scale structural behavior will be improved.

1.7 Thesis Overview

In the chapters to follow, the reader will be taken through the research that led up to this study, including discussions into the state of the art of finite element methods as they apply to fracture mechanics. The research will be presented in the order that it was conducted, starting with the modeling and testing of calibration specimens and concluding with prediction and verification of fracture in non-standard test specimens.

The chapters will be broken down as follows:

Chapter 1 - *Introduction*: introduces the problem and scope of the study. It includes the research focus and methodology, as well as background information and the source of motivation for the research.

Chapter 2 - *Terminology*: covers the terminology as it is used in the field of fracture mechanics and finite element analysis.

Chapter 3 - *Previous Work*: discusses relevant previous research in the fields of micromechanics and finite element analysis as it applies to fracture mechanics. It provides insight into the current methodologies utilized in finite element fracture mechanics analysis.

Chapter 4 -*Objectives and Approach*: provides the main objectives of the study, experimental rationale of the approach, and sets limits on the overall scope.

Chapter 5 - *Experimentation*: provides the experimental method and outlines

the various tests and test specimen designs utilized. This section describes the relevance and details the specific purpose of each specimen. Experimental data is presented for fundamental material properties.

Chapter 6 - *Finite Element Modeling*: introduces the finite element procedure and element formulation utilized by Warp3D. This chapter includes the basis for adjustments to material properties, determination of material characteristic length, and element sizing.

Chapter 7 - *Finite Element Analysis Calibration and Experimental Results*: presents the calibration tests and results and illustrates how the information is applied to the finite element model.

Chapter 8 - *Experimental Results and Verification*: covers the finite element predictions of crack growth for center cracked panels in tension, along with the results from laboratory testing.

Chapter 9 - *Summary, Conclusions, and Discussion*: summarizes the testing and analytical results and presents conclusions regarding the applicability of this method to other structures. Limitations of the finite element method and Warp3D are also discussed.

Chapter 2

Terminology

The terminology utilized in any field must be universally accepted if ideas are to be shared and understood. Fracture mechanics, being no exception, has a standard terminology, summarized in ASTM E616 - Standard Terminology Relating to Fracture Testing.[9]

Some terminology specific to this work include the following:

Characteristic Length/Distance - The mean distance over which fracture processes must occur before a crack can be said to have propagated, or grown incrementally.

Constraint - a condition wherein material is unable to deform until material around it deforms first. For example, material near a crack is at a higher stress state then the surrounding material. As a result of the higher stresses, the crack tip material tries to elongate in the direction of loading and contract in the orthogonal directions, but is held in place by the surrounding material. This conditions is called constraint.

Elemental Yield Criterion - a criterion that specifies the conditions (stress, strain, porosity, etc.) that must be present in an element, prior to yielding. Standard yield criteria are von Mises and Tresca, for example.

Heterogeneity - a volume of material contained within a larger uniform matrix, where material properties, composition, morphology, etc., deviate from that of the matrix. Inclusions and second phase particles are examples of heterogeneities.

Inhomogeneity - structures that have zones of differing microstructure and/or composition and thus differing mechanical properties.

Plane Strain - Stress state which results in non-zero strains in two orthogonal directions and zero strains in a third. A simple example of plane strain is a thick hexagonal beam where large deformations and therefore strains in the

thickness direction are constrained from occurring by other material in the thickness direction. Plane strain conditions, if they occur, tend to be located at the center of materials, away from the free surfaces.

Plane Stress - Stress state which results in non-zero stresses in two orthogonal directions and zero stresses in a third. A simple example of this situation is deformation of a thin flat plate. Since a thin flat plate has very little stiffness in the through thickness direction, it is incapable of carrying load in that direction and therefore, the surface normal stress is zero. Plane stress conditions occur at the free surface of materials.

Surface Finish - The root mean square of the peak heights and valley depths on a surface, expressed in microinches.

Triaxiality - in this study, the ratio of hydrostatic stress (σ_m) to von Mises stress (σ_e).

Some of the more important symbols used throughout this work includes the following:

Symbol	Description
η	J-Integral Energy Coefficient, (2+0.522 b_0/W for C(T) specimens)
σ_e	Von Mises Equivalent Stress
σ_m	Hydrostatic Stress
a	Crack Length. (Center cracked plates have a crack length of 2a and a width of 2W.)
B_N	Net specimen thickness
b_0	Uncracked ligament, W-a.
D	Characteristic Length (Process Zone)
E	Modulus of Elasticity
J	The J-integral

J_{el}	The elastic portion of the J-integral - Equivalent to $K^2(1-\nu^2)/E$
J_{pl}	The plastic portion of the J-integral
J_{Ic}	Critical J-integral in Mode I direction
K_I	Stress intensity factor in Mode I direction
K_{Ic}	Critical stress intensity factor in Mode I direction
L	Crack Front Element Length
W	Plate Width. Center cracked plates have a crack length of 2a and a width of 2W.
X_0	Mean inclusion spacing
f_n	Volume Fraction of Void Nucleating Particles
ε_n	Mean Value of Strain Required to Nucleate New Voids
s_n	Standard Deviation from Mean Value of Strain Required to Nucleate New Voids

Common abbreviations are as follows:

ASTM	American Society for Testing and Materials
AWS	American Welding Society
AWS D1.1	Structural Welding Code for Steel
CCP	Center Cracked Panel (also Middle Cracked Tension Panel)
CMOD	Crack Mouth Opening Displacement
C(T)	Compact Tension
CTOD	Crack Tip Opening Displacement
DBT	Ductile to Brittle Transition (Temperature)

EDM	Electron Discharge Machining
EPFM	Elastic Plastic Fracture Mechanics
HAZ	Heat Affected Zone
J-R	J-Resistance Curve (J vs. Change in Crack Length, Δa)
LEFM	Linear Elastic Fracture Mechanics
LLD	Load Line Displacement
M(T)	Middle Cracked Tension (also Center Cracked Panel)
PWHT	Post Weld Heat Treatment
SE(B)	Single Edged Bend
SMAW	Shielded Metal Arc Weld
SMCS	Stress Modified Critical Strain

Chapter 3

Previous Work

Although this work is directed towards the prediction of ductile crack growth in weldments, it is crucial to first review the existing relevant literative work that has led to this study. A logical starting point is the micromechanical modeling and finite element research that has preceded this study.

3.1 Finite Element Modeling

The finite element method is nothing new, having been first used over 2,000 years ago[35] by geometers attempting to measure the circumference of a circle. As calculus had not yet been invented, the problem was broken down into finite parts and solved, producing amazingly accurate results. Practically speaking, however, the use of finite elements in structural analysis had to wait until the mid 1950s when such pioneers as M.J. Turner, R.W. Clough, H.C. Martin, and L.J. Topp introduced this blossoming technology to the world.[35] Finite element analysis is the basis of calculating the stresses and strains, required for micromechanical modeling of mechanical behavior. A typical finite element analysis, usually calculates the deformations, strains, and stresses of structures under a given set of applied loads. The micromechanical approach is to then use these stresses and strains to compute the effect they have on the material properties. When coupled with finite element analysis, this leads to an iterative solution of stresses, strains, and material properties.

In addition to stresses, strains, and displacements, finite element analysis

can also be used to obtain global fracture mechanics parameters through two analysis techniques: point matching and energy methods.[2] The simpler of the two, point matching, is closely related to the stress/displacement solution typical of finite element analysis. In this type of solution, the stress intensity factor for a cracked membrane is inferred based on the stress gradient as the crack tip is approached. The stress intensity factor can be determined by extrapolating to the crack tip ($r = 0$) the plot:

$$K = \sigma_{22}\sqrt{2\pi r} \tag{3}$$

The second type of solution, the energy method, computes the energy release rate of the membrane associated with fracture and from this determines the stress intensity factor. The energy method, while requiring more computation time, has the added advantage that it can be applied to nonlinear problems, common to the field of fracture.

Regardless of whether finite element analysis is applied to micromechanical models of fracture or direct computation of global fracture parameters, an appropriate material model must first be selected. Modeling the material requires assigning physical properties to each element of the finite element array. Many models exist for accomplishing this, each with its own suitability. Some of the more popular models are the bilinear, power law hardening, and piecewise linear models.

3.1.1 Bilinear Material Model

The most basic model, the bilinear material model, is often used to model the deformation of brittle and elastic perfectly plastic materials. Figures 12a and 12b illustrate typical stress-strain curves for brittle and ductile materials, respec-

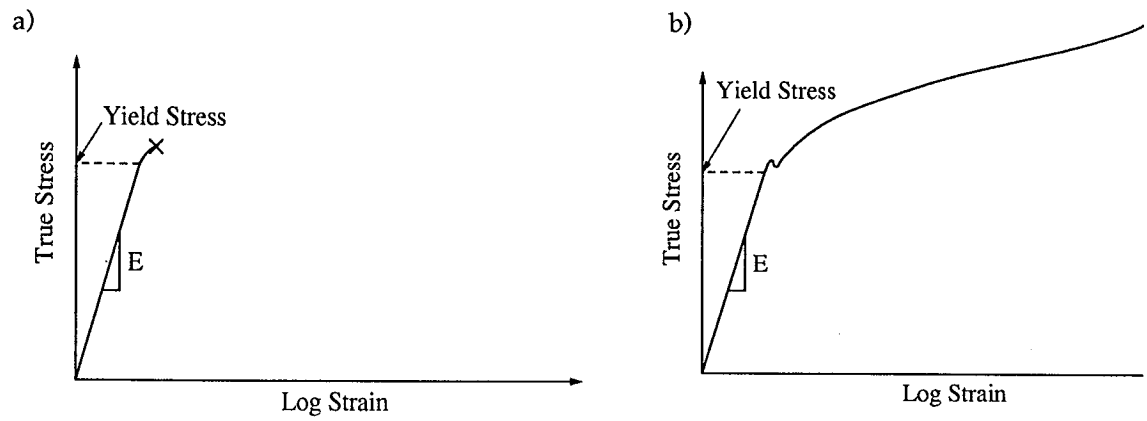

Figure 12: Typical stress-strain curves for steel. (a) brittle, lower shelf and (b) ductile, upper shelf.

tively. Since most materials do not deform linearly in the plastic region, the bilinear material model is normally not well suited for ductile materials. A typical bilinear curve is shown in Figure 13. As can be seen in Figure 14a, the bilinear curve closely represents the brittle material, which could have been steel below the ductile-to-brittle transition temperature, for example. However, for the ductile material shown in Figure 14b, such as steels above the ductile-to-brittle transition temperature, the bilinear model poorly represents the actual stress-strain curve. Although strain hardening is accounted for, it is assumed to be linear. As an alternative, the power law hardening model is sometimes used.

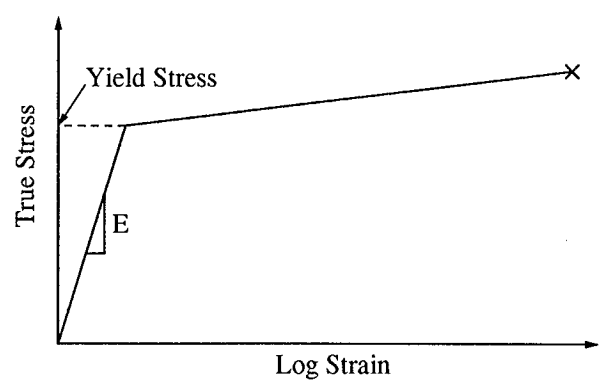

Figure 13: Bilinear stress strain curve.

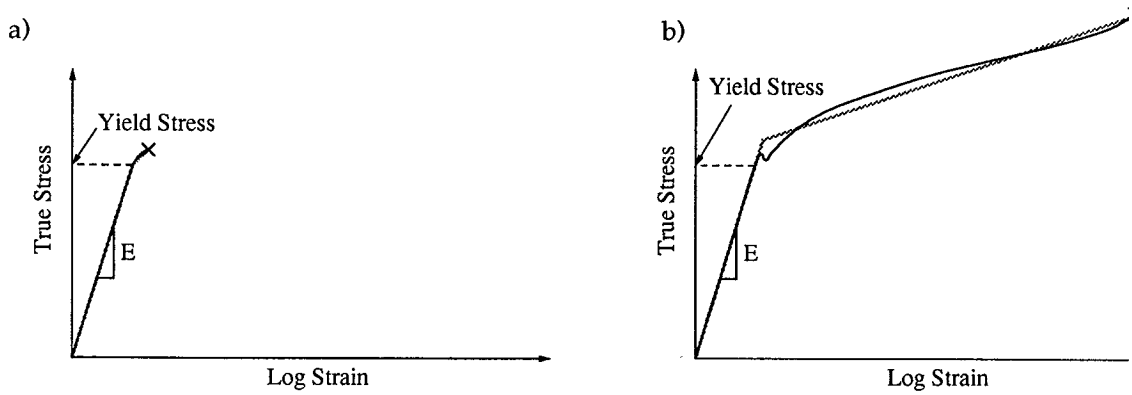

Figure 14: Bilinear modeling of typical steel stress-strain curves. (a) brittle, lower shelf, and (b) ductile, upper shelf.

3.1.2 Power Law Hardening Material Model

The power law hardening curve, shown in Figure 15, is used where a bilinear model does not produce the desired accuracy. This model more accurately models strain hardening then the bilinear model. Unfortunately, power law curves are not well suited to the stress-strain response of many steels.

The problem with both the bilinear model and the power law hardening model is that they are approximations of actual material behavior. These approximations are made to reduce the number of equations required to model the mechanical behavior of materials. One model specifically designed to limit the

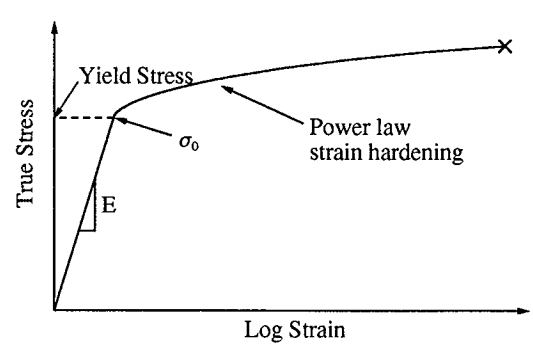

Figure 15: Power law hardening stress-strain curve.

extent of the approximation is the piecewise linear model.

3.1.3 Piecewise Linear Material Model

The piecewise linear model is constructed of multiple linear segments, with each segment closely matched to experimentally measured mechanical properties. Accuracy can then be increased as necessary simply by increasing the number of segments used to describe the entire stress-strain curve. An eight segment piecewise linear curve is shown in Figure 16. Using piecewise linear curves may be more accurate than other mathematical approximations, however the use of more equations can result in longer computational times and unsolvable (divergent) problems.

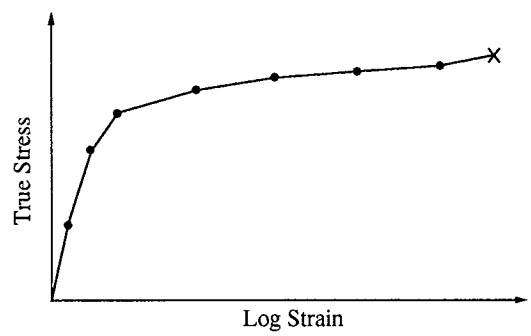

Figure 16: Eight segment piecewise linear stress-strain curve.

3.2 Micromechanics of Ductile Crack Growth

Micromechanics is the modeling of material processes on the microstructural scale. It follows then that, micromechanical modeling of ductile crack growth is the modeling of material processes, on the microstructural scale, that lead to ductile crack growth.

Ductile crack growth is the culmination of several micromechanical processes which occur as a result of an externally applied stress field. The first

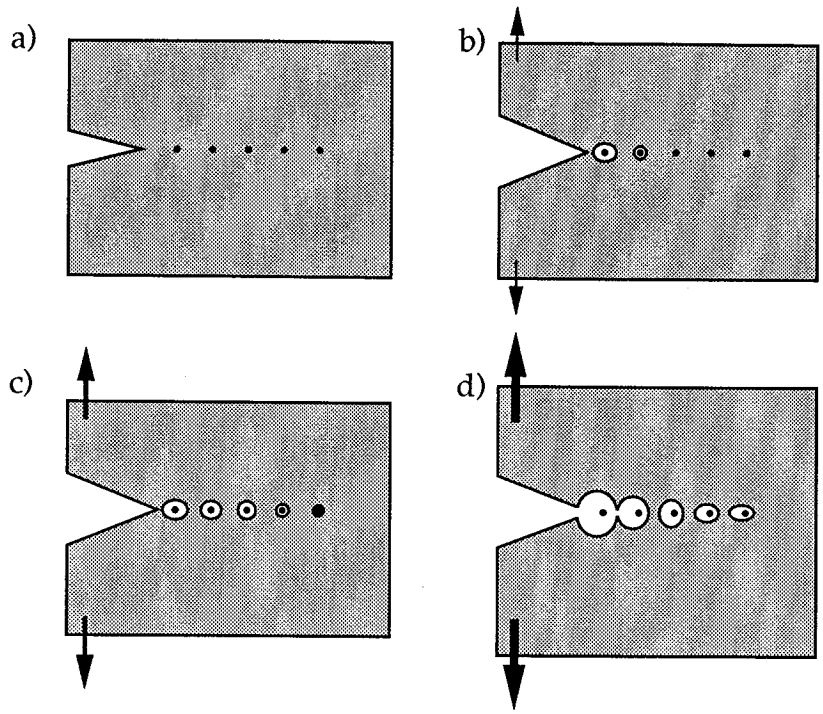

Figure 17: Nucleation and coalescence of voids from inclusions and second phase particles.

micromechanical process is void nucleation as shown in Figure 17b. Voids tend to nucleate at locations in the material matrix where the cohesive energy is the lowest, such as at inclusions or second phase particles. In steels, for example, second phase particles of manganese sulfide provide ideal nucleation sites. The exception to this rule is the preferential nucleation of voids at some large inclusions and second phase particles. Although the cohesive energy at these particles is high, attributable to their large surface area, these particles tend to be brittle and fracture under relatively small applied loads.[2]

As the applied load increases, void growth occurs. This is the second micromechanical process of ductile crack growth and is shown in Figures 17b and c. Initially, nucleated voids are roughly spherical in shape. As they grow, however, these voids tend to expand fastest in a plane perpendicular to the principal stress field.

The third and final micromechanical process of ductile fracture is the coalescence of voids as shown in Figure 17d. As voids grow larger and the density of voids increases, interactions between voids must occur. Coalescence is simply the joining of two or more voids, a process which eventually culminates in the formation of a crack.

Although the micromechanical process of ductile crack growth can be broken down into these distinct phases, it is important to note that each phase is not mutually exclusive. Therefore, although nucleation must precede growth, and growth must precede coalescence, all three processes continue to occur as long as a driving force for the process exists.

While there are a number of different micromechanical models of ductile crack growth that have been developed over the years, several have been referenced extensively and stand out above the rest in terms of accuracy and usage: The Rice and Tracey model, the stress modified critical strain model, and the Gurson-Tvergaard or Gurson model.

3.2.1 Rice-Tracey Model

The Rice-Tracey model[2] is a void growth model which assumes a spherical void within a micromechanical cell. As normal stresses and strains are applied, the void deforms in proportion to the local stresses, becoming ellipsoidal. The rate of deformation is characterized by:

$$\dot{R}_i = \left[(1+G)\dot{\varepsilon}_i + \sqrt{\frac{2}{3}\dot{\varepsilon}_j\dot{\varepsilon}_j}D\right]R_0 \qquad (i,j = 1,2,3) \tag{4}$$

where D and G are material constants determined by the strain rate and strain hardening, and R_0 is the initial void radius.

If the incompressibility condition:

$$\dot{\varepsilon}_1 + \dot{\varepsilon}_2 + \dot{\varepsilon}_3 = 0 \tag{5}$$

is rewritten in terms of $\dot{\varepsilon}_1$ and ϕ:

$$\dot{\varepsilon}_2 = \frac{-2\phi}{3+\phi}\dot{\varepsilon}_1 \tag{6}$$

$$\dot{\varepsilon}_3 = \frac{\phi-3}{3+\phi}\dot{\varepsilon}_1 \tag{7}$$

$$\phi = -\frac{3\dot{\varepsilon}_2}{\dot{\varepsilon}_1 - \dot{\varepsilon}_3} \tag{8}$$

Then, substituting Equations 6, 7, and 8 into Equation 4 and making some simplifying assumptions:

$$R_1 = \left(A + \frac{(3+\phi)B}{2\sqrt{\phi^2+3}}\right)R_0 \tag{9}$$

$$R_2 = \left(A - \frac{\phi B}{\sqrt{\phi^2+3}}\right)R_0 \tag{10}$$

$$R_3 = \left(A + \frac{(\phi-3)B}{2\sqrt{\phi^2+3}}\right)R_0 \tag{11}$$

where:

$$A = \exp\left(\frac{2\sqrt{\phi^2+3}}{3+\phi}D\varepsilon_1\right) \tag{12}$$

$$B = \frac{(1+F)(A-1)}{D} \tag{13}$$

and ε_1 is the total strain integrated from the initial undeformed condition to the current state. This has been empirically solved by Rice and Tracey as:

$$\ln\left(\frac{\bar{R}}{R_0}\right) = 0.283\int_0^{\varepsilon_{eq}} \exp\left(\frac{1.5\sigma_m}{\sigma_{YS}}\right)d\varepsilon_{eq} \tag{14}$$

where R is the average of R_1, R_2, and R_3, and ε_{eq} is the equivalent plastic strain.

3.2.2 Stress Modified Critical Strain Model

The stress modified critical strain or SMCS model is a void coalescence micromechanical model. SMCS predicts the equivalent plastic strain for a given triaxiality state required to cause coalescence of voids and consequently failure.

One method of determining the SMCS failure criterion was demonstrated by MacKenzie[34] and Panontin.[41] The failure criterion was generated by performing tensile tests on notched and smooth tensile round bar specimens. That is, circumferential notches of various width and constant depth are machined in the gage section of the specimens prior to testing. These specimens are then pulled to failure, while monitoring load, strain, and diametral contraction. The load at fracture initiation can be determined from the sudden drop in load carrying capacity that occurs at initiation. Based on finite element models of these specimens, the triaxiality and equivalent plastic strain at fracture initiation can be

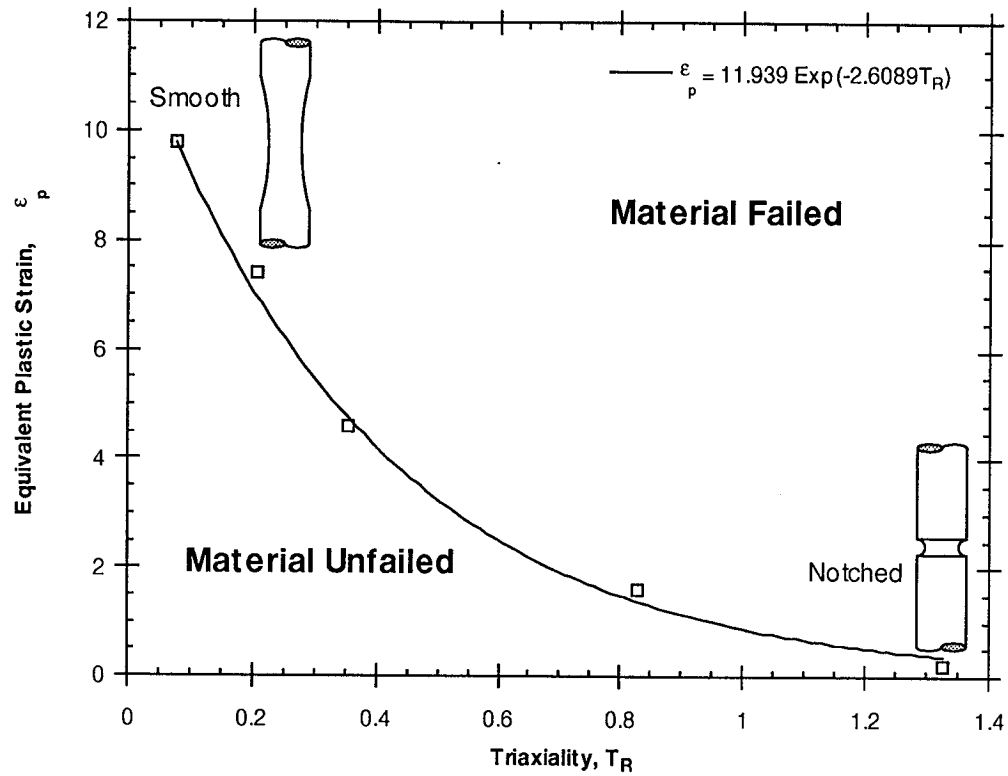

Figure 18: SMCS failure criterion.

determined. Triaxiality is then plotted against equivalent plastic strain, where the resulting curve makes up the SMCS failure criterion. This is shown in Figure 18.

According to the micromechanical model, void coalescence has occurred over a length of material, when the equivalent plastic strain over that length of material exceeds the failure criterion for the triaxiality over the entire length. An alternative approach, demonstrated by Panontin[41] is to subtract the equivalent plastic strain in each cell from the equivalent plastic strain at failure, as determined by the triaxiality of the cell. This is represented by the equation:

$$\Delta\varepsilon_P = \varepsilon_{P(actual)}(T_R) - \varepsilon_{P(failure)}(T_R) \tag{15}$$

Therefore, failure has occurred over the length of cells where $\Delta\varepsilon_P$ is greater than

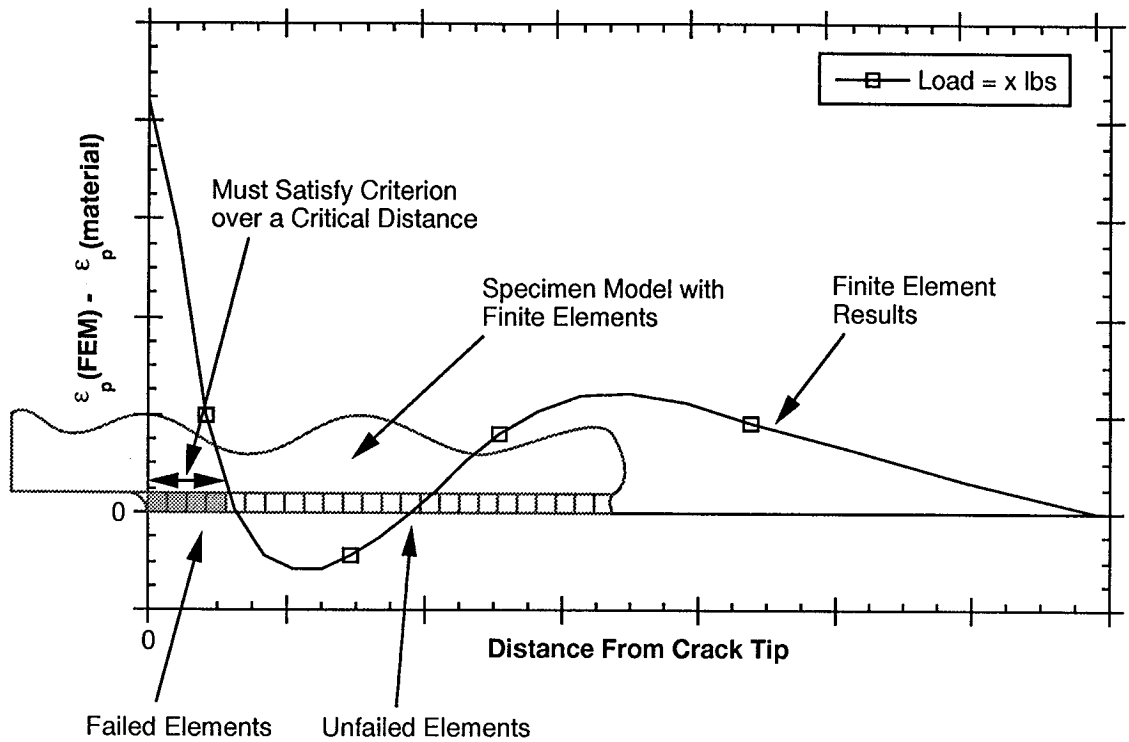

Figure 19: Failed length of cells as predicted by the stress modified critical strain void coalescence model.

zero. This is illustrated in Figure 19.

3.2.3 Gurson-Tvergaard Void Growth Model

Like many material models used to characterize void nucleation and growth phenomenon, the Gurson (1977a) model makes the simplifying assumption that voids are spherical or cylindrical in nature.[25] This has been shown to be a fairly good assumption[23], especially so, when the nucleating particles are spherical in shape.

The Gurson model (1977a)[25,32] suggests an element yield condition that is a function of σ_e, the Mises equivalent macroscopic stress, σ_m, the mean macroscopic stress, $\bar{\sigma}$, the Mises equivalent stress of the matrix, and f, the void volume fraction.

$$\Phi = \left(\frac{\sigma_e}{\bar{\sigma}}\right) + 2f\cosh\left(\frac{3\sigma_m}{2\sigma}\right) - (1 + f^2) = 0 \tag{16}$$

Unlike the von Mises and Tresca Yield criteria which do not account for material softening and are functions of the applied normal stress, the Gurson yield criterion changes as void volume fraction in the element changes. According to the Gurson model, the element yield criterion, Φ, goes towards zero, as the void volume fraction goes towards 1.0 (100%).

The void volume fraction increases due to void nucleation and growth, under increasing applied stresses. The crack propagates as elements reach a void volume fraction of 1.0, consequently exceeding the elemental yield criterion.

To improve the models prediction ability for periodic arrays of spherical and cylindrical voids, Tvergaard modified the Gurson element with factors q_1, q_2, and q_3, and developed the Gurson-Tvergaard (GT) model[32,54]:

$$\Phi = \left(\frac{\sigma_e}{\bar{\sigma}}\right) + 2q_1 f\cosh\left(\frac{3q_2\sigma_m}{2\sigma}\right) - (1 + q_3 f^2) = 0 \tag{17}$$

Note that Equations 16 and 17 reduce to the standard Mises yield condition when the current void volume fraction is zero. Tvergaard suggests values of 1.5 and 1.0 for the variables q_1 and q_2, respectively, in an elastic-perfectly plastic material. More recently, research by Gao[22] suggests that q_1 and q_2 vary with the material strain hardening and strength.

An additional modification to Equation 16 was proposed by Tvergaard, although it is not directly reflected in Equation 17. According to the Gurson model, the load carrying capacity of an element shrinks to zero when the void volume fraction approaches unity. However, experimental evidence shows that

this is not the case. Examination of fracture specimens by Brown and Embury have shown that the critical void volume fraction (i.e. where load carrying capacity goes to zero) is much closer to 0.15 and not 1.0 as predicted by Equation 16.[54] Therefore, Tvergaard and Needleman[54] introduced the function, $f^*(f)$ to model the complete loss of load carrying ability while still at a realistic void volume fraction:

$$f^*(f) = \begin{cases} f & \text{for } f \le f_c \\ f_c - \dfrac{f_v^* - f_c}{f_F - f_c}\langle f - f_c \rangle & \text{for } f \ge f_c \end{cases} \tag{18}$$

where f_v^* is the uncorrected void volume fraction at failure equal to $1/q_1$, f_c is the critical value of f when coalescence begins, and f_F is the void volume fraction at final fracture.

Even under conditions wherein the initial void volume fraction is zero, new voids will nucleate at inclusions, second phase particles, and grain boundaries. Many analyses in the past ignored the effects of these heterogeneities, however, the nucleation of new voids can play a significant role in ductile tearing.[23]

The Gurson-Tvergaard model presented in Section 3.2.3 accounts for void growth, but special consideration must be given to account for void nucleation. The increase in volume fraction of voids with load is due to growth of existing voids, as well as nucleation of new voids at inclusions, second phase particles, and grain boundaries. Therefore,

$$df = df_{growth} + df_{nucleation} \tag{19}$$

The change in void volume fraction due to void growth is a function of the current volume fraction of voids, or:

$$df_{growth} = (1 - f)d\varepsilon^p \tag{20}$$

The change in volume fraction due to void nucleation is a function of the current plastic strain in the matrix:

$$df_{nucleation} = A(\bar{\varepsilon}^p)de^p \tag{21}$$

Chu and Needleman suggest that A is of the form

$$A = \frac{f_N}{s_N\sqrt{2\pi}}\exp\left[-\frac{1}{2}\left(\frac{\bar{\varepsilon}^p - \varepsilon_N}{s_N}\right)^2\right] \tag{22}$$

where ε_N is the mean strain required for nucleation with a standard deviation of s_N and f_N is the volume fraction of void nucleating particles.[32] For steels and related materials, the values of ε_N, s_N, and f_N are 0.3, 0.1, and 0.04, respectively.[16]

3.3 Problems with Micromechanical Void Growth Models

There are many problems with the existing body of micromechanical models that are used to predict fracture mechanics, least of which is not determining stresses and strains in the micromechanical cells. Finite element analysis is an important tool used to determine the cell stresses and strains. However, at high levels of plasticity, solutions are not always forthcoming, sometime requiring many iterations and significant computational time to be solved. In some cases, there is no solution, and the utility of the model breaks down.

Another significant problem that affects void growth models stems from the method by which the voids themselves are modeled. In the continuum approach, materials are assumed to be homogeneous, with the effect of voids averaged throughout the material. This assumption, which is used in the Gurson Model and the Rice and Tracey model, precludes any possibility of void interaction, such as void linking. In addition, both models assume a regular array of spherical voids throughout the material matrix. This assumption breaks down when the nucleating particles are irregularly shaped, and as the crack approaches final fracture. Becker, et al. has shown experimentally for sintered iron powders that near final fracture, the linked voids lose their spherical appearance, causing discrepancies between the actual and predicted strength.[54] This is shown qualitatively in Figure 20. Since void linking is ignored in the Gurson and the Rice and Tracey models, erroneous results at high strains can occur and ultimate failure cannot be predicted.

Thomason[2] extended the Rice and Tracey model to include a failure

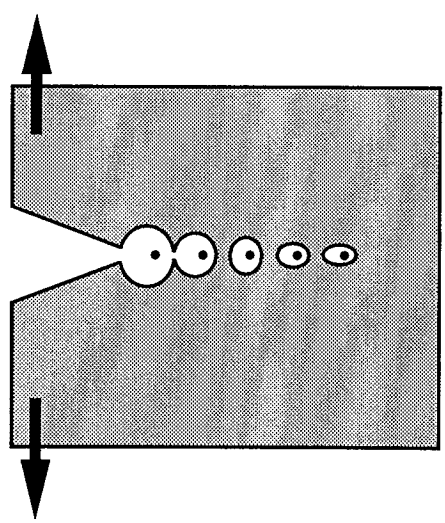

Figure 20: Coalescence of initially spherical voids, results in loss of spherical appearance per Becker, et al.

criterion based on the limit load for internal necking between microvoids. This allowed predictions of failure strains that were much closer to experimental values and an order of magnitude lower than those generated with the unmodified Gurson model (Equation 16).

The original Gurson model had very few parameters. Specifically, the yield condition was a function of σ_e, the Mises equivalent macroscopic stress, σ_m, the mean macroscopic stress, $\bar{\sigma}$, the Mises equivalent stress of the matrix, and f, the void volume fraction. However, modifications by Tvergaard, Chu, Needleman, and others, have left the Gurson Model with a great number of adjustable parameters, including three nucleation parameters and three correction factors. Many of these parameters are not representative of physical characteristics, which makes arriving at values for them even more difficult.

3.4 Finite Elements and Micromechanics

Finite element analysis is well suited for use with micromechanical modeling since it provides a simple method for computing the stresses and strains within the micromechanical cells. Several different programs have been modified or developed to utilize micromechanics to compute large scale plasticity and crack growth.

3.4.1 Warp3D

Warp3D is a finite element research code developed by Koppenhoefer et al. at the University of Illinois.[32] This code, which is currently under development, utilizes a preconditioned conjugate gradient solver to analyze the dynamic nonlinear response of solids to applied loads and displacements.

Warp3D predicts crack growth through several different micromechanical

models, including the Gurson-Tvergaard and stress modified critical strain models. The Gurson-Tvergaard method implemented in Warp3D was the method selected for this study, since it is the only method that employs the void growth model and predicts crack growth.

Unlike standard finite element analysis methods, element size in Warp3D is material dependent and is linked to the volume of material ahead of the crack tip over which softening occurs. The element size is generally similar, if not the same, as the material characteristic distance discussed in Section 3.7. Consideration must be given, however, to the appropriateness of the element size since it has a direct effect on the accuracy of crack tip stress and strain computations.

3.4.2 Warp3D and Fracture Specimens

Warp3D was used previously to predict ductile crack growth in A533B and A516-70 standard fracture test specimens.[43] Ruggieri, et al. applied the Warp3D implementation of the Gurson element to SE(B) and C(T) fracture specimens and found that it performed adequately in predicting J-R curves and crack front shape.

3.5 Consideration of Weld Inhomogeneity

Inhomogeneity is the key element that separates the study of welds from other materials. Due to the differences in microstructure and material properties between the weld metal, heat affected zone (HAZ), and the base structure, many long accepted theories of fracture mechanics must be modified or disbanded.

The crack tip stresses of a homogeneous component can be calculated using classical fracture mechanics through one of several different single parameter stress factors: the stress intensity factor (K), the J-integral (J), and the crack tip opening displacement (CTOD). Fracture toughness, the material constant at

which fracture occurs, can be related to a critical value of any one of the single parameter stress factors. However, these methods were developed for use in homogeneous structures and are not necessarily applicable to the inhomogeneous nature of a welded structure. Differences in flow and plasticity, and constraint resulting from material mismatch are the main reasons that fracture parameters are affected by inhomogeneity of weldments.

Sunwoo and Morris[53] showed for 2090 aluminum alloy weldments, that differences in material properties were attributable to inhomogeneities in the weldment microstructure. These inhomogeneities resulted from differences in the thermochemical processing between the base metal and the fusion zone. The fusion zone lacked strengthening precipitates present in the base material, resulting in increased weld metal constraint, effectively confining plastic deformation to the weld. This had the effect of reducing the weldment mechanical properties to that of the weld metal.

Kirk also used finite element analysis to predict J versus load or crack tip opening displacement for strength overmatched and undermatched welds. Two different classes of models were developed and the results compared. The first model, the bimetal model, consisted of different homogeneous properties for the plate and weld metal. The second model, the heterogeneous weld, contained a strength profile across the heat affected zone. Models of various weld geometries provided data showing the difference in calculating J using the bimetal and heterogeneous assumptions. From these results, it was determined when the bimetal assumptions were applicable. This took the form of a minimum distance between the crack tip and the weld/base metal interface, L_{min}, above which the bimetal assumption performed acceptably. For all of the different weld geometries and configurations tested, it was shown that for a 20% strength overmatched welded

plate, there was little or no difference between J calculated using the two different assumptions when L_{min} was greater than 0.2 inches (5 mm).[30] Therefore, variation of properties across a 20% strength overmatched weldment can be ignored if the crack tip remains 0.2 inches (5 mm) from the weld/base metal interface.

3.6 Modeling Cracks in Welds

Many attempts have been made to predict crack stability in welded structures. Different material models, representing brittle and ductile fracture have been utilized, as have simplifying assumptions of homogeneity. Additionally, different load conditions, such as tension, bending, and a combination of the two have been attempted.

Before modeling the stresses surrounding a crack, one must model the stresses in a weld. Raghavendren and Fourney[42] developed a two-dimensional finite element model of butt welds to determine the stress distributions across a crack free weld under tension and bending loads. The analysis included plane stress and plane strain conditions and computed the effects of embedded porosity in the weld. The results show a good correlation between the finite element model and photoelastic analysis for a butt welded plate in plane stress. This approach, however, lacked two important factors that can strongly affect the stress distribution in a weld. First, the residual stresses due to welding were neglected, and second, the analysis treated the material as homogeneous across the weld. Research by Kirk, et al. discussed in Section 1.3 shows that under certain conditions, the bimetallic weld assumption produces acceptable results. Residual stresses are often reduced by stress relieving, and are often neglected in analysis

since they can be difficult if not impossible to compute.

Berge, et al. validated a finite element model of butt-welded plates with semi-elliptical surface cracks along the fusion line under four-point bend, low-temperature loading conditions. These efforts were limited to low temperature brittle fracture, using the Level-3 CTOD method, or reference strain method, proposed by Anderson, et al.[13] It was shown, that the plane stress Level-3 CTOD method overpredicted applied CTOD for cleavage. In addition, it was found that underprediction of CTOD occurred for a plane strain Level-3 CTOD method, that takes into account linear-elastic effects of crack geometry. The best results came from a plane strain Level-3 CTOD method that took into account plastic deformation and load redistribution.

Schmitt and Blauel[45] used the Gurson model and accurately predicted static J-resistance curves for irradiated weld material.

Schwalbe applied the Engineering Treatment Model (ETM) to a tension loaded plate with a "structurally short" weld metal crack, to determine the crack tip opening displacement as a function of applied load or applied strain. This method was limited to piece-wise power law materials, but did allow for different material properties between the base and weld metals. It was shown that deviation of the weld metal stress-strain curve from that of the base metal, could have a marked effect on the applied CTOD. Additionally, it was found that critical loads or critical crack length could be predicted, based on a given toughness level. These results stemmed from the result that the applied CTOD could be simply expressed as a function of applied strains or loads.[47]

3.7 Characteristic Length for Ductile Fracture

One of the more popular techniques for predicting crack growth using micromechanical models involves the void growth or Gurson model. Used by Dodds,[15] Schmitt,[45] and others, this method of finite element analysis has the unique difference in that the size of elements along the crack front are determined by the material that the crack is contained within.

Normally, in finite element analysis, element size is determined by finding the element size of diminishing returns. If the elements are chosen too small, analysis time can increase dramatically. If the elements are chosen too large, accuracy suffers. In the G-T void growth model, accuracy of stresses and strains are still determined by the element size, although now element size is a material fracture parameter, equivalent to the length of material over which a critical void density must be reached, before a crack initiates. This characteristic length, *D*, shown in Figure 21, can be determined in several different ways, depending on the level of accuracy expected.

Using the stress modified critical strain method of determining the charac-

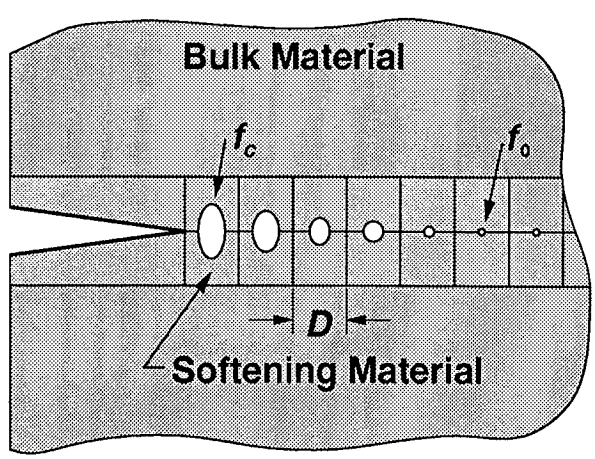

Figure 21: Definition of material characteristic distance and process zone size.[15]

teristic length, Panontin[41] demonstrated that for A516-70 steel the characteristic length was 0.003 inches (0.076 mm). This was determined by loading a single edged bend specimen to the point of crack initiation, and modeling the same specimen using finite element analysis. Using an ultra-refined mesh (elements along the crack plane 10 times smaller than the expected characteristic length), an analysis was performed to the point of crack initiation. Based on a SMCS failure criterion for A516, developed through testing of uniaxial notched tension specimens, the distance from the crack tip to the last element that satisfied the failure criterion was measured.[41]

Another method sometimes utilized, and demonstrated by Schwalbe[46] and Garrison[23] is based on metallography or fractography of specimens. In this method, the characteristic length is determined based on the distance between, and size of, inclusions in the material.

To use the microscopic method, the initial area fraction of inclusion particles must be determined. This is accomplished by photographing several sections of the ductile fracture surface at random and measuring the total area photographed. The mean inclusion area is then measured and multiplied by the number of inclusions in the photographed area. The initial inclusion area fraction is then determined as:

$$f_{0_a} = \frac{\text{Total Particle Cross Sectional Area}}{\text{Total Area}} \tag{23}$$

Moody[38] demonstrated that the inclusion area fraction could be used in place of the inclusion volume fraction, based on the assumption that fracture generally occurs along a plane, thereby involving planes of inclusions. Thus,

$$f_{0_a} = f_{0_v} \tag{24}$$

This initial inclusion volume fraction can then be converted into a mean inclusion spacing using a formula presented by Garrison[23] as:

$$\frac{X_0}{d_0} = \frac{0.36}{\sqrt{f_{0_v}}} \tag{25}$$

$$X_0 = \frac{0.36 d_0}{\sqrt{f_{0_v}}} \tag{26}$$

where d_0 is the mean inclusion diameter and X_0 is the mean inclusion spacing. An example of this calculation is included in Section 6.4.1 for the weld material of this study.

This method will provide the experimenter with an empirical value for the material's mean inclusion spacing. The characteristic length is generally on the order of the mean inclusion spacing. For example, Panontin found that for A516-70 steel, the characteristic length was 1-2 times the mean inclusion spacing.[41] Of course, it is up to the experimenter to refine the value through analysis of well known and verifiable test cases.

Chapter 4

Objectives and Approach

4.1 Objectives

As discussed in the previous section, a current methodology exists for applying laboratory testing to actual structures for the case of homogeneous, monolithic materials. However, no such methodology exists for the case for defective welds with nonhomogeneous material properties.

The objectives of this study are therefore:

1. To extend the existing methodology of modeling homogeneous materials to include modeling of welds with material properties different from the base metal.

2. To examine applicability of methodology to structural configurations which include buried weld defects.

3. To determine the weld metal mechanical properties, such as flow characteristics, initial void volume fraction, and characteristic length, which are required to perform accurate crack growth predictions using the Gurson-Tvergaard micromechanical model and finite element analysis.

4. To evaluate Gurson model calibration techniques, used to refine experimentally determined mechanical properties.

4.2 Approach

In order to make crack growth predictions in structural configurations, a number of material properties and parameters need to be measured and calibrated. The empirical approach of this study is diagramed in the flow chart of Figure 22.

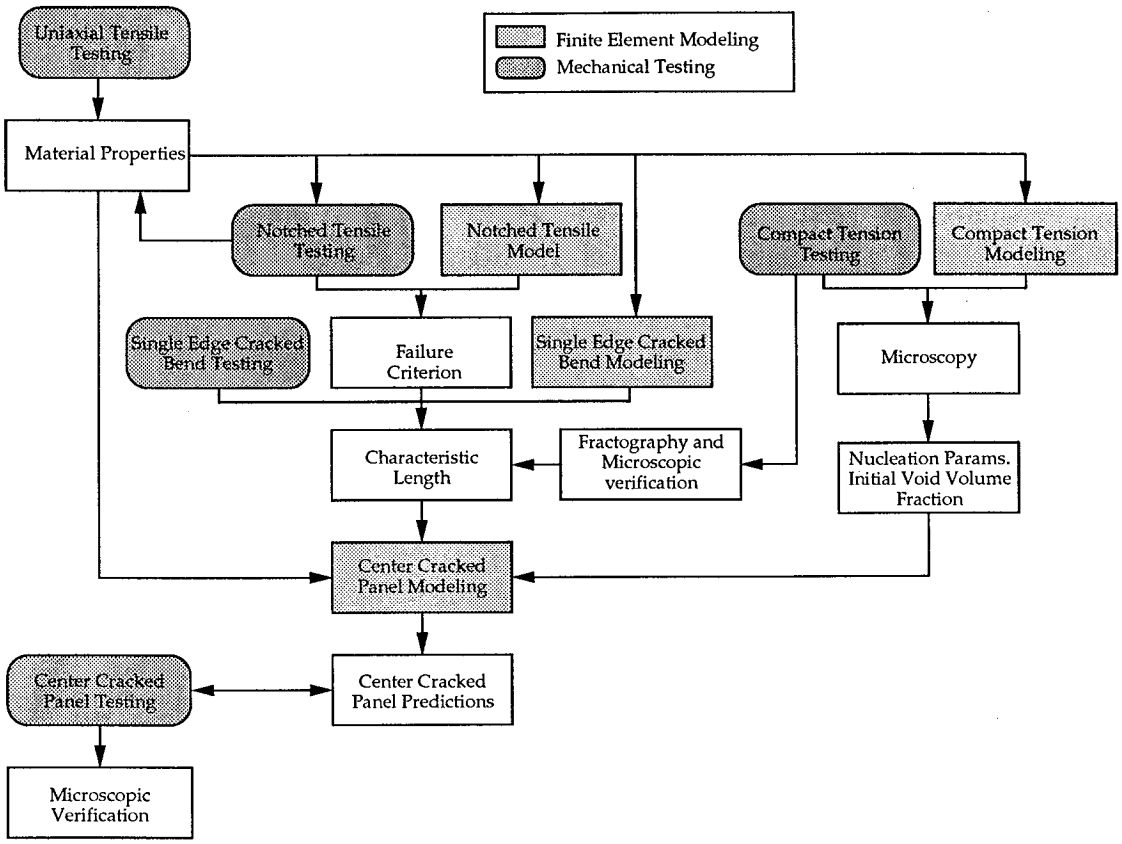

Figure 22: Experimental approach flow chart.

The study first characterizes the material properties associated with weldments, consisting of E7018 weld rod and A516-70 plate steel. This was accomplished through testing and analysis of smooth and notched round-bar tension specimens. This was followed by determination of the material characteristic length, through the testing of single edged bend specimens. Calibration of several finite element parameters, including element size and initial void volume fraction, was carried out through the modeling and testing of compact tension specimens.

The main objective, modeling crack growth in a welded structural configuration, was then accomplished through the testing and modeling of center cracked panels. Solutions and materials parameters, developed in the previous tests, were

applied to the model, and predictions were made as to the crack front size and shape, J-resistance curve, and crack mouth opening displacement.

Chapter 5

Experimentation

The fabrication, setup, and testing of specimens is the main focus of this chapter. Fabrication includes weld preparation, welding, post-weld heat treatment, and machining. The preparation of specimens after they were machined, including strain gaging and the attachment of knife edges is the subject of specimen setup. Finally, testing will cover the testing methodology, ASTM and related requirements, equipment utilized, and characterization of basic mechanical properties.

The experimental procedure can be broken down into the following steps:

1. Test Specimen Design
2. Materials Selection
3. Weld Fabrication
4. Specimen Fabrication
5. Specimen Setup and Testing
6. Microscopy
7. *FEA Element Sizing - Chapter 6*
8. *Calibration of FEA Crack Growth Parameters - Chapter 7*
9. *Verification of FEA M(T) Results - Chapter 8*

Those parts of the experimental procedure related to finite element analysis are marked in italics and will be discussed in the chapters to follow. This chapter will concentrate on those steps solely related to materials testing.

5.1 Test Specimen Design

The test specimens utilized in these experiments were prepared according to ASTM standards where applicable. A number 16 surface finish or better was

applied to all specimen faces, as required by the ASTM standards. Although standard milling techniques were utilized for basic cutting and shaping of specimen blanks, electron discharge machining (EDM) was used to cut all complex shapes, including crack starter-notches.

The EDM technique is an extremely accurate method of machining, and can be used to produce very tight radii and sharp edges. When standard milling techniques are utilized, crack starter-notches are rarely sharp enough to quickly initiate fatigue cracks. To help alleviate this problem, the ASTM specification recommends machining a chevroned crack starter-notch, to assist in the initiation of a fatigue precrack. However, when a straight crack starter-notch is cut with 0.003 inch (0.076 mm) diameter EDM wire, fatigue crack initiation occurs readily. In this way, using EDM to cut crack starter-notches simplifies machining and shortens the time required for specimen precracking.

Fabricating specimens from the weld metal of a butt welded plate can be difficult, especially when the weld is small with respect to the specimen size. To insure that specimen blanks were cut from the proper area and in the correct orientation, the welded plate was macroetched with 5% Nital to reveal the weld structure. Outlines of specimen blanks were then drawn onto the welded plate, to provide guidelines for cutting of specimen blanks.

5.2 Materials Selection

The metals used in this study were chosen because of their use in the pressure vessel industry and in wind tunnel construction at NASA-Ames Research Center. A common type of connection is a butt weld consisting of A516 Grade 70 steel base metal, joined with an E7018 welding electrode.

5.2.1 A516 Grade 70 Steel

A516 Grade 70 is a low carbon-manganese fine grained steel used in pressure vessels where improved notch toughness is important. In plate form, it is characterized by a tensile strength of 70-90 ksi with a minimum yield strength of 38 ksi and a minimum total elongation of 21% over 2 inches. Above room temperature, A516-70 exhibits upper shelf behavior. The composition is shown in Table 1.

5.2.2 E7018 Weld Rod

E7018 weld rod is a covered low-alloy steel arc-welding electrode which employs a 25-40% iron powder electrode covering. Weld strength is 84.4 ksi, with a yield strength of 72.8 ksi. When used with A516-70 steel, the weld is approximately 50% strength overmatched. The chemical composition of the welding electrode is given in Table 1. It should be noted, however, that the composition of the weld metal varies throughout the weld, and generally lies somewhere between the composition of the weld electrode and the parent material.

Table 1: Material chemical requirements

	Chemical Composition, %					
Material	C	Mn	P	S	Si	Mo
A516-70[a]	0.25	1.06	0.006	0.011	0.21	0.004
E7018-A1[33]	0.12	0.90	0.035, max	0.04, max	0.80	0.40-0.65
Typical Weld	0.22	0.92	0.020	0.02	0.60	0.50

a.From plate certification, Geneva Steel Company.

5.3 Weld Fabrication

A 10 foot x 8 foot (3 m by 2.4 m), 1.5 inch (38.1 mm) thick A516 Grade 70 plate was procured for the purpose of this test program. The plate was cut into smaller pieces, one measuring 2 feet by 4 feet (0.6 m by 1.2 m). This plate was cut

along the long axis and welded together according to the following specifications:

- Preheat and interpass temp of 50°F to 250°F (10°C to 121°C)
- Weld bead size = $\frac{3}{16}$ to $\frac{5}{16}$ inch (4.8 to 7.9 millimeters)
- Stringer beads only
- Electrode storage per AWS D1.1
- Land separation $\frac{1}{8}$ inch (3.2 millimeters)
- Stress relieve (PWHT) per AWS D1.1 - Structural Welding Code - Steel
- 100% radiographic inspection as per AWS D1.1

The weld utilized a double "V" weld preparation with required 60° weld angle as shown in Figure 23. The specification calls for shielded metal arc welding (SMAW) using 0.25 inch (6.5 mm) weld beads. In this welding process, the plates are placed together, with the lands of the preparation separated by 0.125 inches (3.2 mm), and two or three weld passes are placed in the root of the weld preparation. The plate is then flipped over and the weld root is gouged out. Then, two or three weld passes are performed in the now gouged out weld root. With the weld root processed on both sides, the plate is then flipped to each side, alternately, with a weld pass being performed each time the plate is turned over. The purpose of welding in this manor is to improve the quality of weld and reduce bending due to residual stresses in the weld metal.

Once the weld was completed, a 100% radiographic inspection of the weld was performed according to AWS D1.1, Section 8.15.3, to verify that the weld was good, containing no cracks and being free of any rounded defects larger than 3/32 in. (2 mm). The plate was then stress relieved for 4.5 hours at 1200°F (650°C) to minimize residual stresses in the weld. Finally, the plate was blanchard ground, a process which removes material from both sides of a plate, to obtain parallel flat

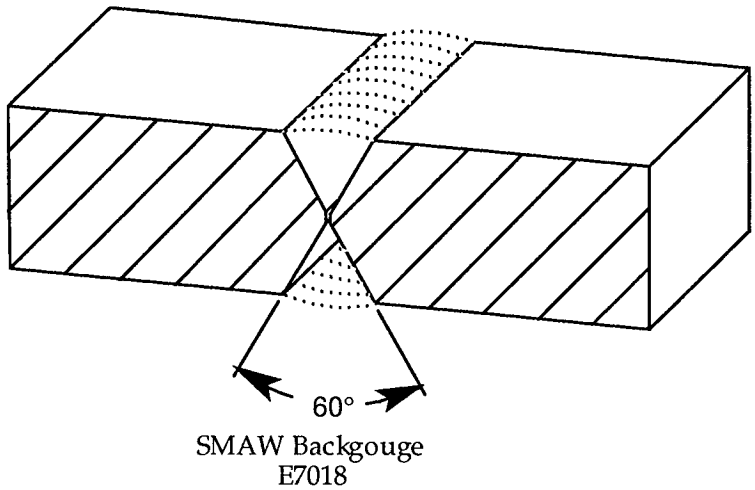

Figure 23: Weld preparation guidelines for weld specimens.

surfaces. This had the effect of removing the weld crowns and reduced the overall thickness of the plate to 1.25 inches (31.8 mm).

5.4 Specimen Fabrication

Once the welded plate was prepared, specimens were cut from both the base and weld metal regions as indicated schematically in Figure 24. These specimens included smooth and notched tensile specimens, single edge cracked bend specimens, compact tension specimens, and center cracked panels.

Characterization of basic mechanical properties was required, both for initial modeling, model calibration, and final verification. The required properties to be measured are listed in Table 2. For a piecewise linear material model, the overall shape of the true stress-true strain curve is required, along with values for Young's modulus, Poisson's ratio, and the 0.2% offset yield stress. The piecewise linear material model was selected for these analyses, due to its accurate representation of the material flow properties. However, the trade-off for this improved level of accuracy revealed itself as a significant increase in computer analysis time,

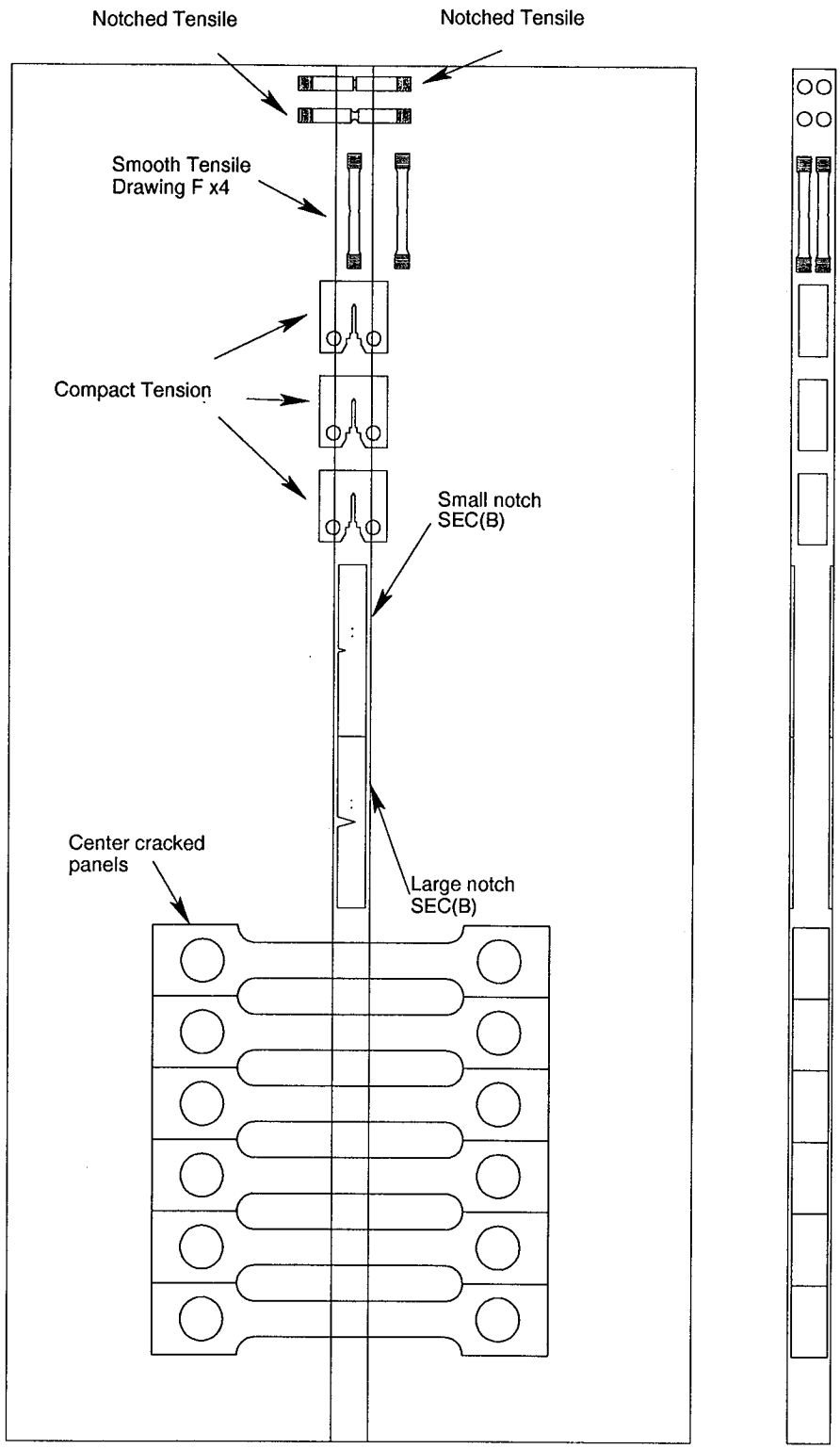

Figure 24: Welded plate specimen layout.

necessary for the interpolation of solutions along the piecewise linear curve.

Table 2: Required properties for analysis using Gurson-Tvergaard Model

Property	Symbol	Section[a]	Reference[b]
Young's Modulus	E	5.5.2	
Poisson's Ratio	ν	5.5.2	
Yield Stress	σ_0	5.5.2	
Hardening Modulus	E_T	5.5.2	
Initial Void Volume Fraction	f_0	7.0	Equation 19
Stress Strain Curve		6.3	Used with piecewise linear curves.
Reference Strain Rate	ε_{ref}	7.0	

a. Property covered in listed section of this report.
b. Property used in listed form or equation.

5.5 Tensile Testing

5.5.1 Specimens

Tensile specimens were prepared according to ASTM E8: Standard Test Methods of Tension Testing Metallic Materials.(5) Three different types of tensile specimens were fabricated: the smooth round-bar specimen shown in Figure 25 and both a small notched (0.125 inch - 3.175 mm notch diameter) and a large notched (0.25 inch - 6.35 mm notch diameter) specimen shown in Figure 26. These specimens were cut from the welded A516-70 plate as detailed in Section 5.3, such that the intended deformation region consisted only of weld metal. In order to make the entire fracture region consist of only weld metal, the specimen had to be reduced in diameter from the ASTM specification. The actual tested weld specimen configuration had a diameter of 0.257 inches (6.5 mm), reduced to 0.22 inches (5.6 mm) in the deformation region, and therefore deviates from the ASTM

E8 geometry as illustrated in Figure 25. All of the tensile specimens were machined to a number 16 surface finish with 1/2″-20-UNF-2A threads machined on each end to accommodate the specimen mating connector.

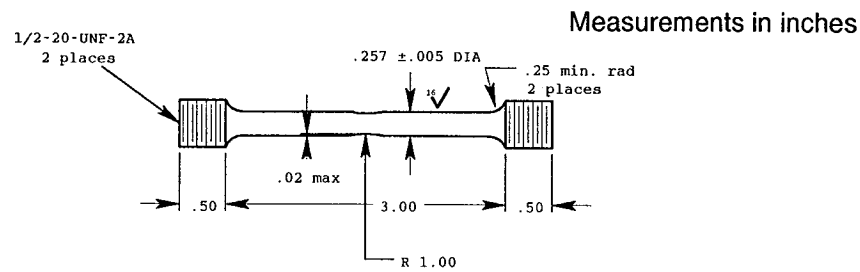

Figure 25: Smooth weld metal tensile specimen. (Figures appear larger in Appendix A for clarity.)

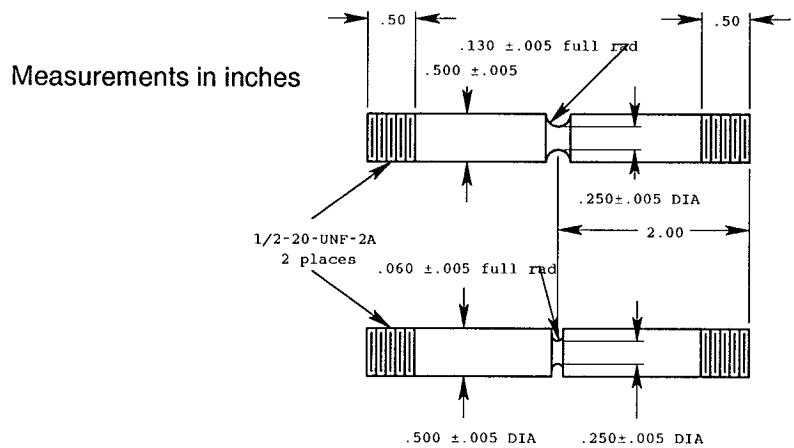

Figure 26: Notched tensile specimens. (Figures appear larger in Appendix A for clarity.)

All of the tensile specimens were machined on a numerically controlled metal lathe, a tool especially suited to the manufacture of axisymmetric parts.

5.5.2 Testing Procedures

Tensile testing was performed according to ASTM E8: Standard Test Methods of Tension Testing Metallic Materials.[5] The purpose of these tests was to determine the basic material properties of stress and strain for both the A516-70 plate and the E7018 welds. In addition, the A516 plate data were compared to data

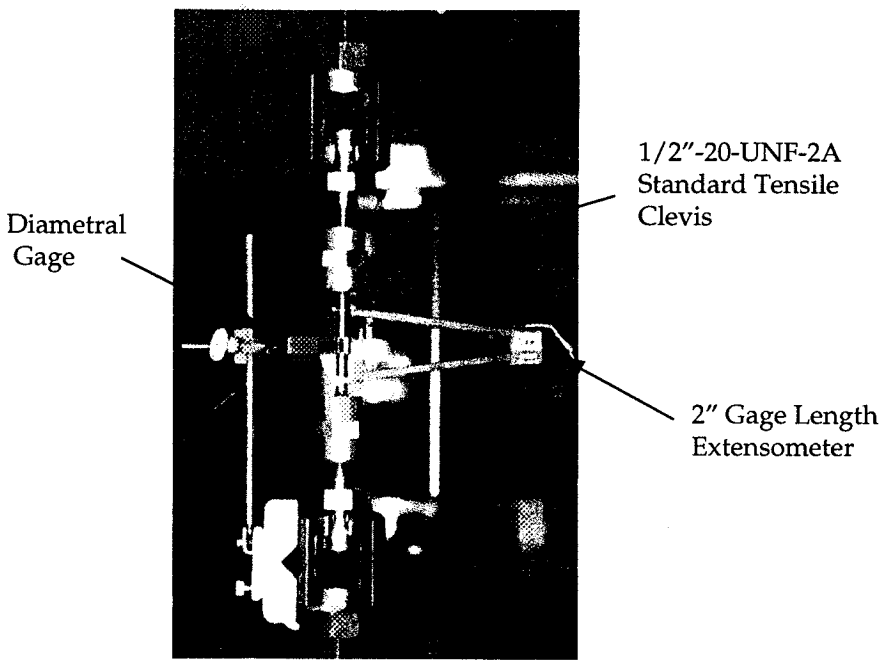

Figure 27: Tensile Round-Bar Test Setup.

previously measured by Panontin.[41] The notched specimens provided data which allowed refinement of the true stress-true strain curve obtained from testing of smooth specimens, through comparison of diametral contraction with finite element analysis. In addition, data from the results of the notched tensile tests were utilized in the generation of a constraint failure criterion which was necessary in determining the weld metals characteristic length. This is discussed further in Chapter 7.

In addition to the standard material properties, inclusion size, area fraction, and spacing were determined by microscopic examination of the post-test fracture surface.

The tensile specimens were tested in a standard tensile test fixture as shown in Figure 27. A 20,000 pound capacity load frame equipped with an MTS electro-hydraulic servo-controlled actuator was utilized. The actuator was controlled by

an MTS 458.20 Microconsole that allowed both digital and analog data acquisition. Load, extension, and diametral contraction were monitored and recorded as the test progressed. The test was conducted in displacement control so that the yield point could be accurately measured. In addition, the displacement rate was maintained at 5×10^{-5} inches per second to avoid any introduction of strain rate effects.

5.5.3 Test Results

Results of the tensile testing for the plate and weld material are shown in Figures 28 and 29. In addition, final fracture data points, based on the unloaded fracture area, are also included.

Adjustments were made to the test data to account for the geometry induced constraint effects (necking) of the test specimen. Large deformation that

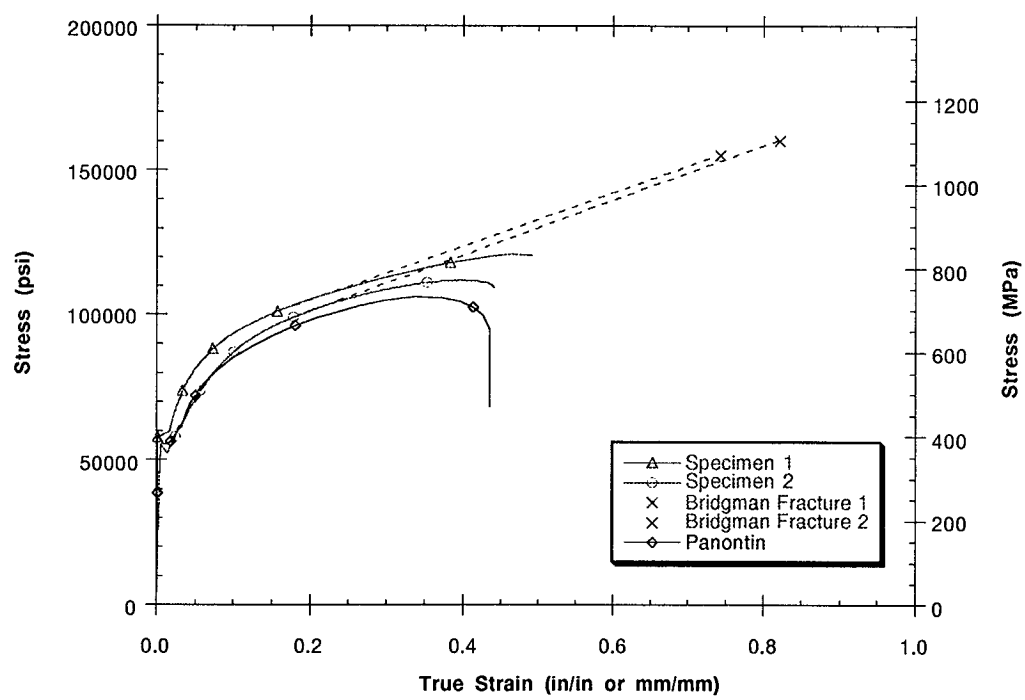

Figure 28: Base metal true stress-strain curves with Bridgman correction factor applied. (duplicate tests)

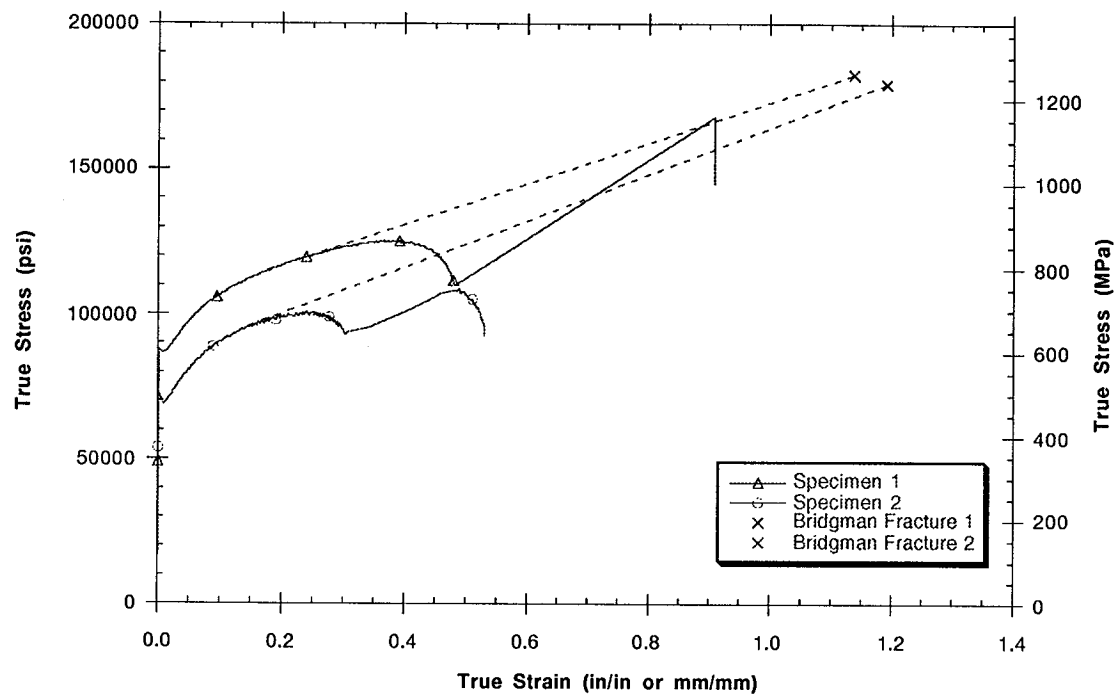

Figure 29: Weld true stress-strain curves with Bridgman correction factor applied. (duplicate tests)

occurs as the specimen necks results in an increase in constraint which can be corrected for by applying the Bridgman correction factor.[37] This factor expresses the corrected stress as:

$$\sigma = \frac{\sigma_{av}}{\left(1 + \frac{2R}{r_n}\right)\ln\left(1 + \frac{r_n}{2R}\right)} \tag{27}$$

where σ is the corrected stress, σ_{av} is the average measured true stress, r_n is the radius of the neck at the thinnest portion, and R is the radius of curvature of the neck. The Bridgman correction for strain beyond necking in steel was previously

developed by McGregor-Tegert, and can be represented as:

$$\frac{\sigma}{\sigma_{av}} = 1 - 0.230\left[\ln\left(\frac{A_0}{A}\right) - \varepsilon_u\right] + 0.0696\left[\ln\left(\frac{A_0}{A}\right) - \varepsilon_u\right]^2 \qquad (28)$$

where A_0 is the initial neck area, A is the instantaneous neck area and ε_u is the strain at necking.[37]

Small decreases in the stress levels of the curves shown in Figures 28 and 29 near failure are the result of the diametral gage not maintaining a position to measure the smallest portion of the neck. The diametral gage was rigidly fixed to the load fixture and as a result, as the specimen necked, the distance from the fixture to the center of the neck changed. Therefore, there was a high potential for the diametral gage to move away from the exact location of the neck.

5.6 Single Edge Cracked Bend Specimen Testing

5.6.1 Specimens

Single edge cracked bend specimens were cut from the welded plate, along the weld, as shown in Figure 24. The specimens were cut such that they consisted entirely of weld metal. The 6 inch (152.4 mm) long bend specimens were designed following guidelines similar to those found in ASTM Standard E399[7] for single edged bend specimens. A number 16 surface finish was required for all surfaces of the specimens. Notches of two different depths were added, as shown in Figures 30 and 31. The shallow notch measured 0.125 inch (3.175 mm) deep, for an initial crack ratio (a/W) of 0.17. The deep notch measured 0.5 inch (12.7 mm) for an initial a/W of 0.66. A 0.003 inch (0.076 mm) diameter EDM wire was used to cut all crack starter-notches, in order to ensure ease of growing a fatigue crack.

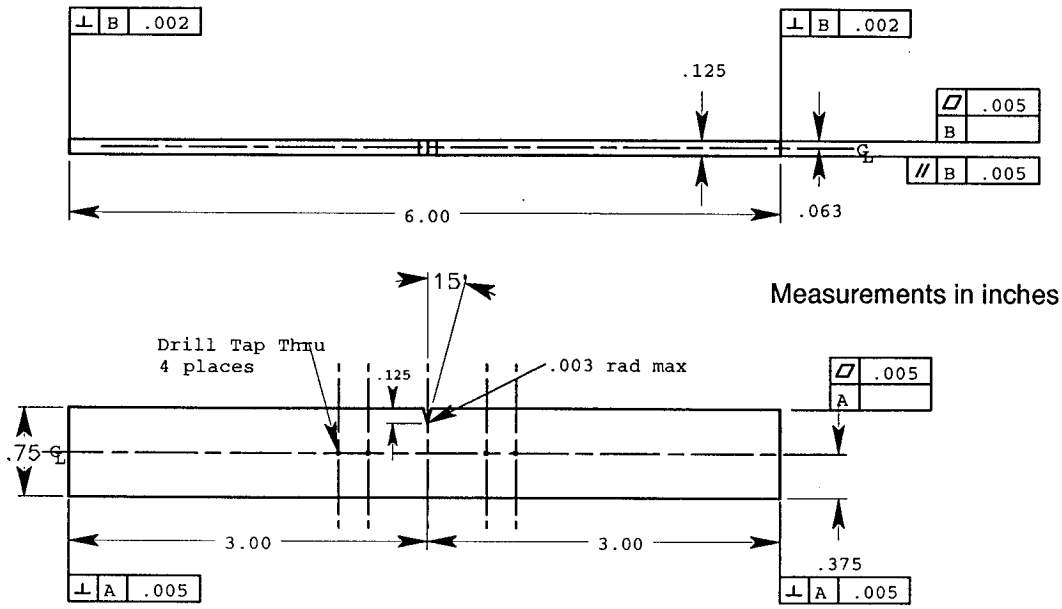

Figure 30: Shallow notched single edged bend specimen. (Figures appear larger in Appendix A for clarity.)

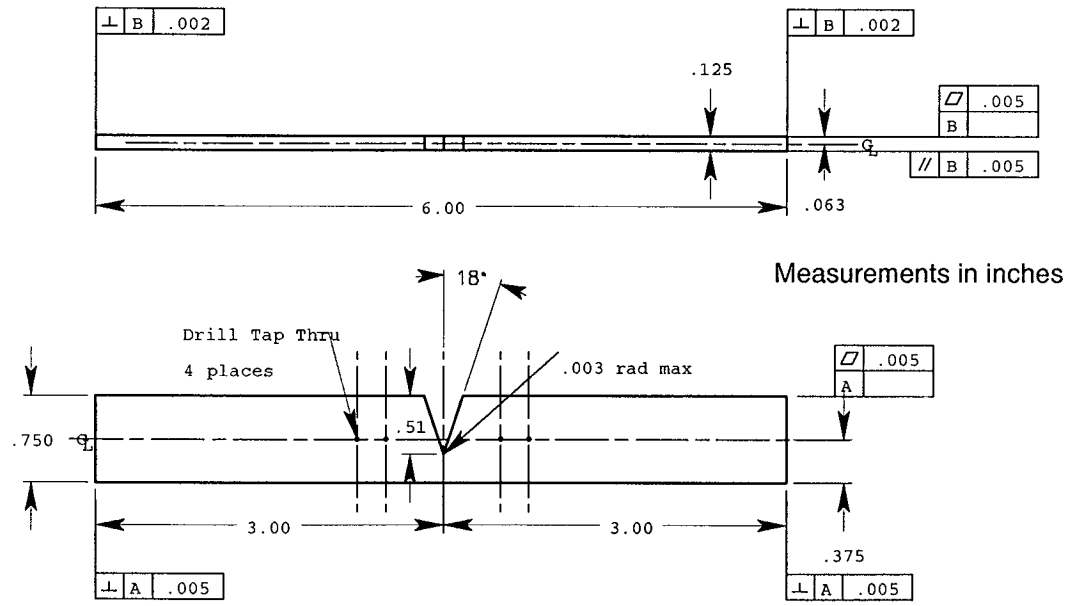

Figure 31: Deep notched single edged bend specimen. (Figures appear larger in Appendix A for clarity.)

Reusable knife edges were fastened to the SE(B) specimens with two-part epoxy, so that CMOD readings could be made. This is shown schematically in

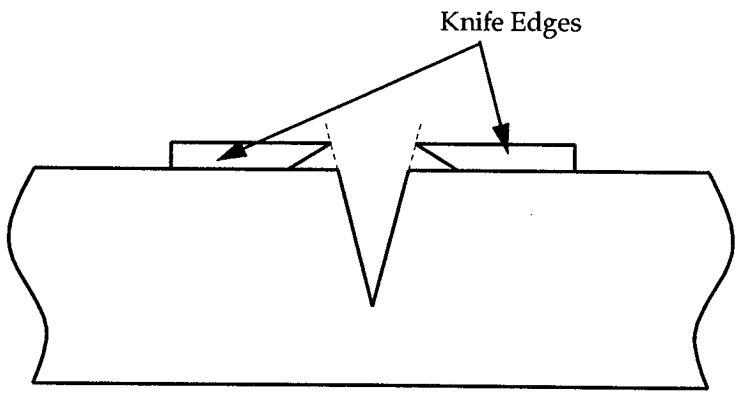

Figure 32: Location of knife edges on single edged bend specimens.

Figure 32.

5.6.2 Testing Procedures

Testing and analysis of SE(B) specimens was performed to determine the characteristic length of the weld metal, using the stress modified critical strain fracture initiation criterion demonstrated by Panontin.[41] By modeling the specimen with an extremely refined finite element model (0.0005 inch elements), crack initiation can be predicted and used to determine the minimum distance over which void coalescence must occur before crack advance can occur. This "characteristic distance" was discussed at length in Section 3.7 and again in Section 6.4. Because the characteristic length is determined phenomenologically, specimens with two different notch lengths were manufactured to allow for verification of the estimate.

Prior to testing the SE(B) specimens, fatigue precracking was used to generate a crack at the crack starter-notch. The specimen was positioned on 0.75 inch (19.1 mm) rollers, separated by a span of 5 inches (127 mm), as shown in Figure 33. This configuration was utilized both for precracking and for testing.

In the short notched beam specimen, the initial a/W was 0.16. The

specimen was then fatigue precracked to an a/W of 0.3. The deep notched specimen was cut to an a/W of 0.66 and fatigue precracked to an a/W of 0.7. Precracking was performed as detailed in Table 3, at a frequency of 5 Hz.

Table 3: Fatigue precracking requirements for SE(B) specimens.

Specimen Type	a/W	R-Ratio	Span	ΔK	P_{max}
			in (mm)	ksi√in (MPa√m)	lbs (kg)
Shallow Notched SE(B)	0.3	0.1	5 (127.0)	18 (19.8)	216 (9.08)
Deep Notched SE(B)	0.7	0.1	5 (127.0)	20 (22.0)	62 (28.1)
Conducted ΔLoad at 5 Hz					

A 20,000 pound capacity load frame equipped with an MTS electro-hydraulic servo-controlled actuator was utilized for fatigue precracking and testing. Since the specimens lacked integral knife edges and since precision CMOD values were not available, precracking was run semi-automatically in load

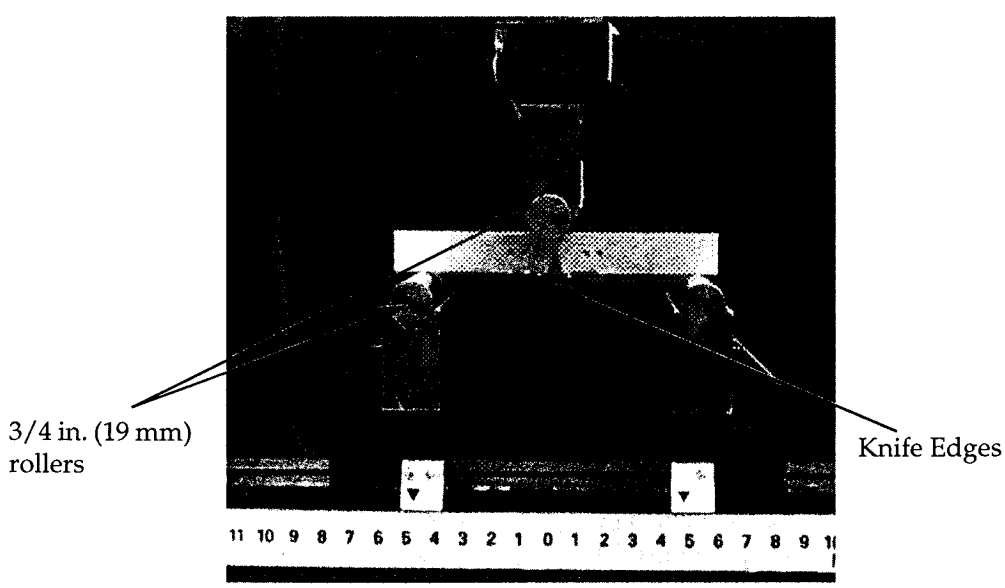

Figure 33: single edged bend testing setup. Deep notched specimen shown.

control with a constant cyclic load. The load was adjusted as the crack grew so that the stress intensity never exceeded 20 psi·√in. Optical crack length measurements were taken periodically to verify instantaneous crack length. Prior to precracking, the final crack length was marked on the specimen with a scribe. A thin oil layer, applied to the surface of the specimen, provided a clear, optical indication of the instantaneous crack length.

Once the desired crack length had been achieved, the specimens were tested. Testing was conducted in displacement control after finite element analysis of the specimen geometry suggested that the required load for crack initiation occurred after the load had leveled off. The load to fracture initiation was estimated from *J* values for the weld material and a known characteristic length for similar plate materials. With load limit switches set at the predicted fracture initiation load value, the specimen was loaded. Testing was concluded at the predicted fracture initiation load. Data were recorded digitally, on a computer based data acquisition system, and using an analog pen plotter. The specimen was then sectioned and mounted in Bakelite, where it was ground to the midplane of the specimen. The surface was then polished to reveal the crack front so that fracture initiation could be verified.

The results of these tests are presented and discussed in Section 6.4.

5.7 Compact Tension C(T) Testing

5.7.1 Specimens

Compact tension specimens like the ones shown in Figure 34 were utilized to determine a weld material J-R curve. This curve, along with CMOD data, provided the basis for determining several finite element parameters that could

not be measured by more conventional means. These parameters, discussed in Section 7.2, include the initial void volume fraction and the crack tip element size. Additionally, the C(T) specimen was utilized to verify that the values for nucleation parameters and correction factors taken from the literature were accurate. Adjustment of these finite element parameters was accomplished by matching crack mouth opening displacement and J-resistance curves, as well as crack front shape and length. These specimens were designed and manufactured according to ASTM Standard E813: Test Method for J_{Ic}, A Measure of Fracture Toughness. As with the previous specimens, the C(T) specimens were manufactured such that the crack plane lay within the weld of the plate.

5.7.2 Testing Procedures

One difficulty that arose during testing was dealing with the problem of using a standardized test on non-standard specimens. Specifically, the J-R test was designed for the testing of homogeneous materials. The weld specimen, however, is by its very nature nonhomogeneous. Consequently, the crack tip opening displacement (CTOD) could not be related to *J* and CMOD, as described in E813. To minimize the effects of inhomogeneity across the heat affected zone on ductile crack extension, the C(T) specimens were designed such that the weld interface-to-defect distance met the Kirk, et al. requirement.[31] As such, standard C(T) specimen design guidelines were utilized.

Compact tension testing was performed according to ASTM Standard E813: Test Method for J_{Ic}, using MTS 790.50 Fracture Toughness Testing Software. The software, running on a IBM 486 computer, controlled an MTS 458 Microprofiler connected to an MTS electro-hydraulic servo-controlled actuator. This software performed precracking and single specimen testing according to Section 8.4 of the

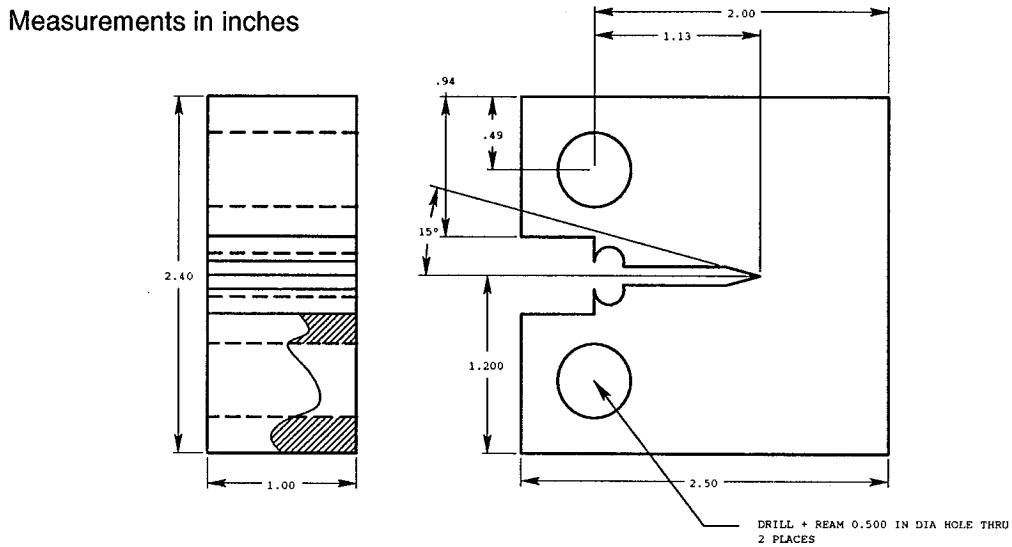

Figure 34: Compact tension C(T) specimen. (Figures appear larger in Appendix A for clarity.)

ASTM Standard E 813.

The specimens were supported by means of a pinned clevis with flattened holes to prevent pin "roll-up" in the hole. Measurements of CMOD were taken using a displacement clip gage attached to integral load-line machined knife edges. Load, stroke, and CMOD were recorded digitally by a computer as well as an analog pen plotter. Figure 35 illustrates the test setup including the positioning of the displacement clip gage.

Fatigue precracking was conducted in stress intensity control using the parameters shown in Table 4. Once fatigue precracking was completed, testing was initiated. As dictated by ASTM Standard E813, testing was conducted in CMOD or clip gage control. The single specimen, crack increment technique of ASTM Standard E813 Section 8.4 was utilized. As required by the specification, a crack mouth opening displacement increment of 0.010 inches (0.254 mm) per step, with a maximum rate of 0.0002 inches (0.005 mm) per second was utilized. Five unloads to 50% of the load at full CMOD were performed at each step, and a 20

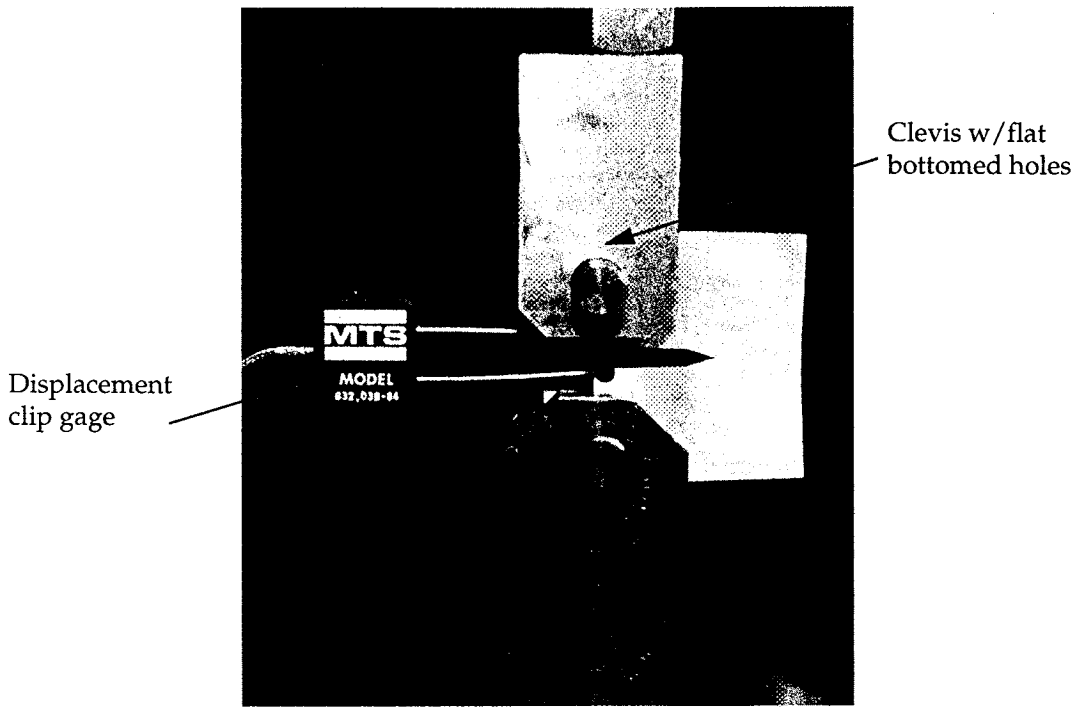

Figure 35: Compact tension test setup.

second hold was performed at the full CMOD, prior to each unload, to allow crack extension. Compliance based crack length measurements were taken after each CMOD hold.

Table 4: Fatigue precracking requirements for C(T) specimens.

Specimen Type	a/W	R-Ratio	Width	ΔK	K_{max}
			in (mm)	ksi√in (MPa√m)	ksi√in (MPa√m)
Compact Tension	0.6	0.1	2.0 (50.8)	18 (19.8)	20 (22.0)
Conducted ΔStress Intensity at 5 Hz					

The J-resistance curve was automatically computed by the MTS 790.50 Fracture Toughness Testing Software, using the CMOD integration technique detailed in Section A2.5 of ASTM Standard E813.

Once testing was complete, the specimen was fatigue cracked further,

marking the final position of the experimental crack front. The specimen was then overloaded to break the specimen. Each fracture half could then be easily studied to examine the experimental crack front shape and size.

The results of these tests are presented and discussed in Section 7.2.

5.8 Center Cracked Panel M(T) Specimens

Tension and tension plus bending center cracked panels make up the primary focus of this research program in that their geometry and loading conditions closely match the conditions present in actual wind tunnel configurations. The geometry of the center cracked panel tension and tension plus bending specimens is shown in Figures 36 and 37, respectively.

Measurements in inches

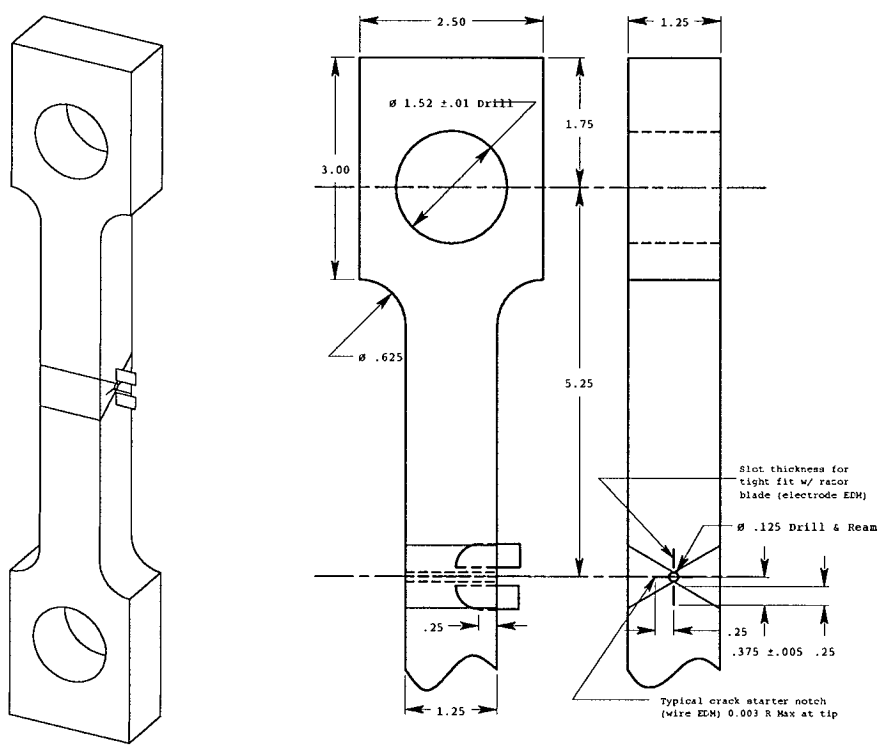

Figure 36: Center cracked panel specimen for tension loading. (Figures appear larger in Appendix A for clarity.)

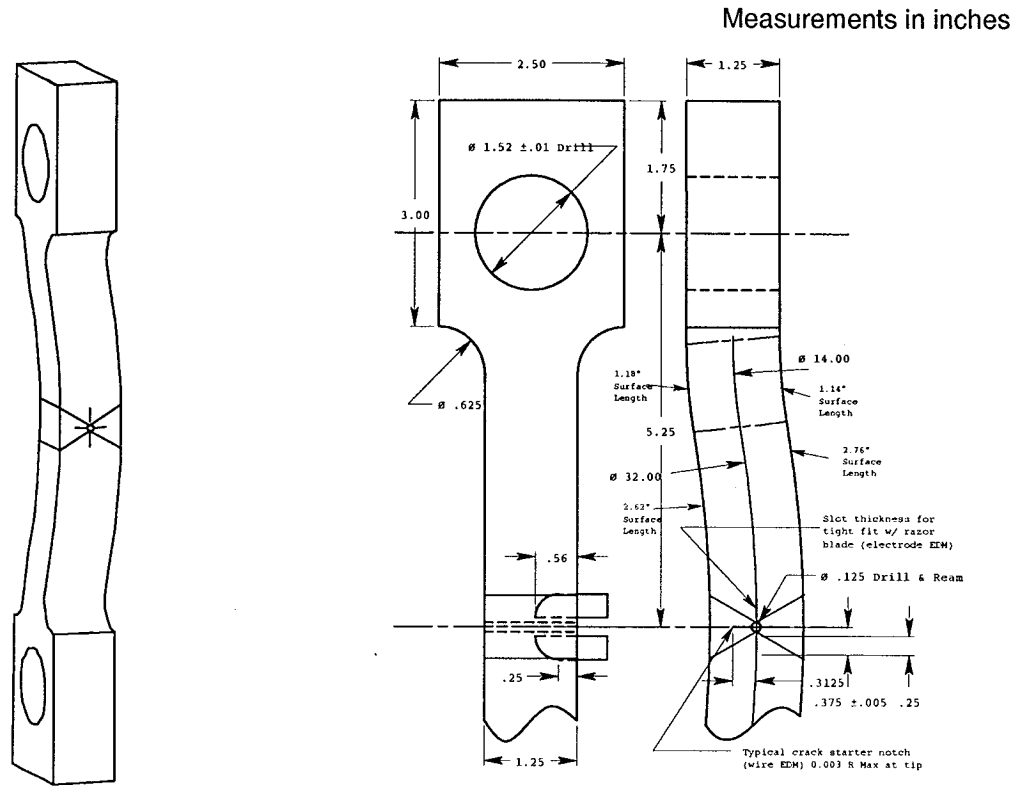

Figure 37: Center cracked panel specimen for tension plus bending loading. (Figures appear larger in Appendix A for clarity.)

A section of the Unitary Plan Wind Tunnel at NASA-Ames Research Center is shown in Figure 38. In this figure, there are two types of butt welds: longitudinal welds, running the length of the tunnel, and circumferential welds, which go around the circumference of the tunnel, joining the individual sections. In addition, there are ring supports which are circumferentially fillet welded to the tunnel. These ring supports are rigid in comparison to the tunnel shell, and attach the tunnel to the ground.

Under operational conditions, the tunnel is pressurized, which produces hoop stresses in the longitudinal welds, and longitudinal stresses in the circumferential welds. These stresses are pure tension and can be approximated using the thin walled pressure vessel equations:

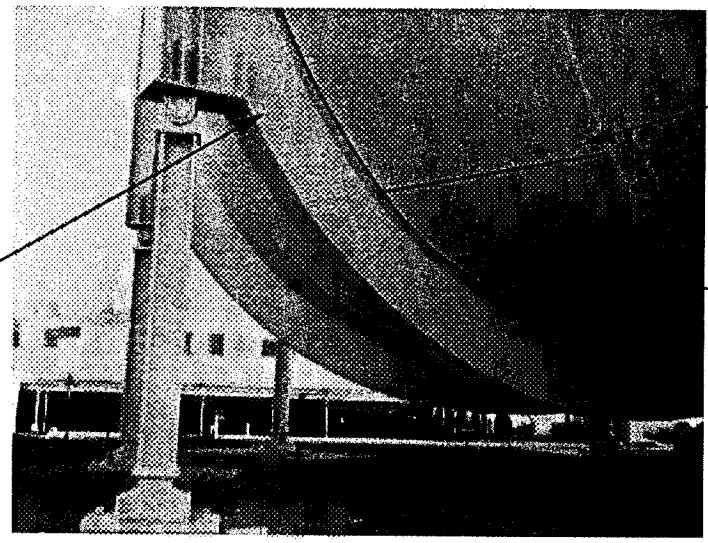

Figure 38: Longitudinal and circumferential butt welds in the Unitary Pressurized Wind Tunnel at NASA-Ames Research Center.

$$\sigma_{hoop} = \frac{pr}{t} \tag{29}$$

$$\sigma_{longitudinal} = \frac{pr}{2t} \tag{30}$$

where p is the gage pressure in the tunnel, t is the wall thickness, and r is the section radius. The situation becomes significantly more complex for welds that occur near the ring supports, however. Due to the rigidity of the ring supports, bending in the tunnel shell occurs. This bending is most pronounced in nearby circumferential welds. The magnitude of the stresses in bending is on the same order as the tension stresses due to pressurization. This results in a state of stress wherein the tension stress at the inner surface is twice the pressurization stress alone, and the stress on the outer surface is zero. This is shown in Figure 39.

Although the center cracked panels utilized in this experiment are by no means conventional, standard ASTM specimen preparation and dimensional

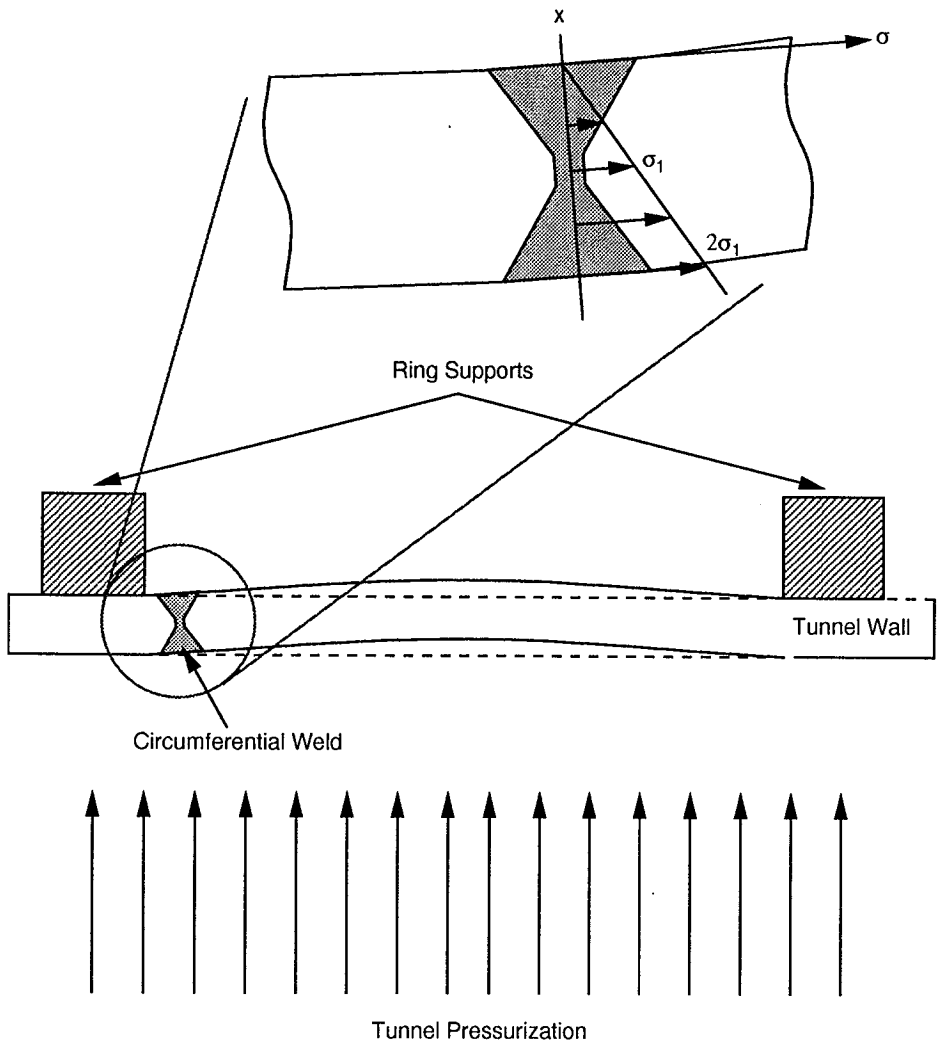

Figure 39: Stress due to bending in circumferential butt welds near ring supports.

guidelines were employed where possible. In order to facilitate cutting the crack starter-notch, a 1/8 inch (3.2 mm) hole was drilled down the center of the weld (Refer to Figures 36 and 37.). The 0.003 inch (0.0.076 mm) diameter EDM wire was then fed down the hole, and crack starter-notches were cut on both sides of the weld. In the first three specimens, the starter notch was cut to an a/W of 0.4. The last three specimens were cut to an a/W of 0.5. This change was implemented once testing began, after problems with growing straight fatigue cracks of equal length

were encountered. The tension panel, shown in Figure 36 is the original center cracked panel design and has an a/W of 0.4.

To facilitate measurement of the crack mouth opening displacement at the center of the specimen, slots were machined into the specimen, perpendicular to the crack plane. These slots were cut using a die-sink EDM, which allows narrow, deep cuts to be machined. Razor blades cut to fit the slots were then inserted and secured with two-part epoxy. This is shown in Figures 36, 37, and 40. A CMOD clip gage can be seen, attached to the blades, in Figure 41.

The original design of the tension plus bending specimen was identical to the tension specimen, excepting the load, which would have been applied from an off-center position. This however proved to be technically non-feasible since the offset required to generate the required amount of bending was determined to be 0.3125 inches (7.9 mm), while the specimen was 1.25 inches (31.75 mm) thick. It was determined that the same stress configuration could be attained by designing a curved specimen and using direct uniaxial tension. Such a specimen is illustrated in Figure 37. However, due to problems with testing these configurations, the tension plus bending specimens have been left for future study.

Measurement Group Precision Strain Gages of type EP-08-062AQ-350 were mounted on the outside of some of the center cracked panel specimens and provided additional displacement information which was used in the verification process. Shown in Figure 40, these gages are smaller than standard gages, specifically designed for localized large scale strain measurements. Under standard temperature conditions, these gages are accurate to elongations up to 10% (100,000μ strain ± 500 μ strain), and perform with high precision (20,000 μ Strain ± 50 μStrain) in the region of interest.

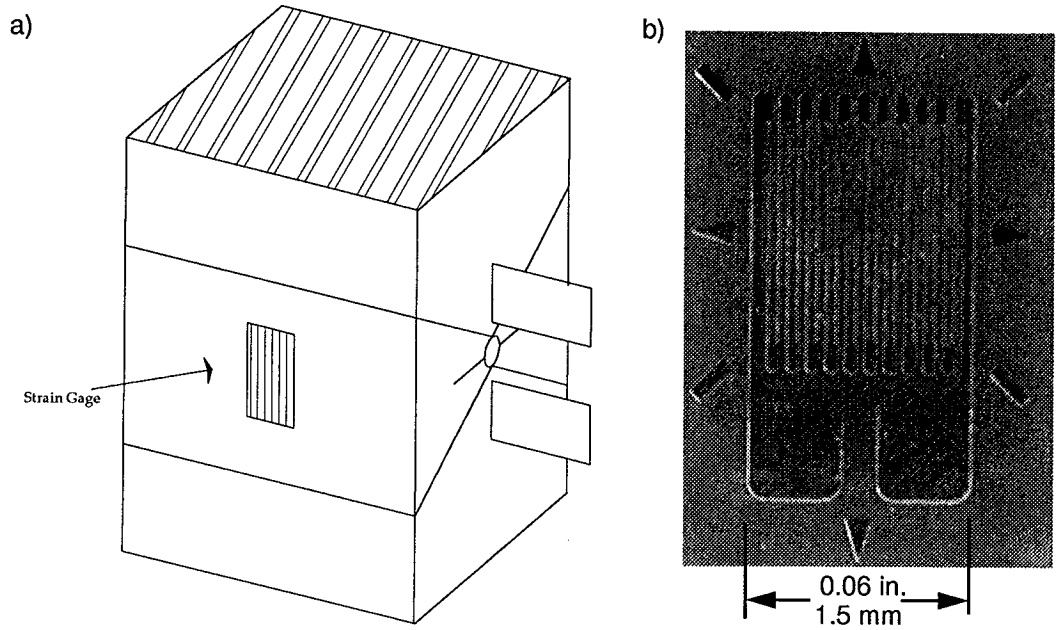

Figure 40: Position of strain gages on center cracked panel specimens. (Refer to Figure 36). b) Measurement Group Precision Strain Gages of type EP-08-062AQ-350.

5.9 Center Cracked Panel M(T) Specimen Testing

Although similar to the center cracked panel presented in ASTM E647, the center cracked panels used in this study were sufficiently different to require special consideration in setting up and performing the test. Testing was performed on a 110,000 pound capacity load frame equipped with an MTS electro-hydraulic dual servo-controlled actuator. Digital data acquisition was provided through a computer link to an IBM 486. Analog data were acquired as well through a mechanical pen plotter. Finally, strain readout and redundant load and CMOD measurements were acquired through a Hewlett-Packard digital data acquisition unit.

The specimen was attached to the load frame through a pair of clevises, pin supported at each end. This is shown in Figure 41. CMOD measurements were

taken from a displacement clip gage attached to the specimen at knife edges attached to the surface.

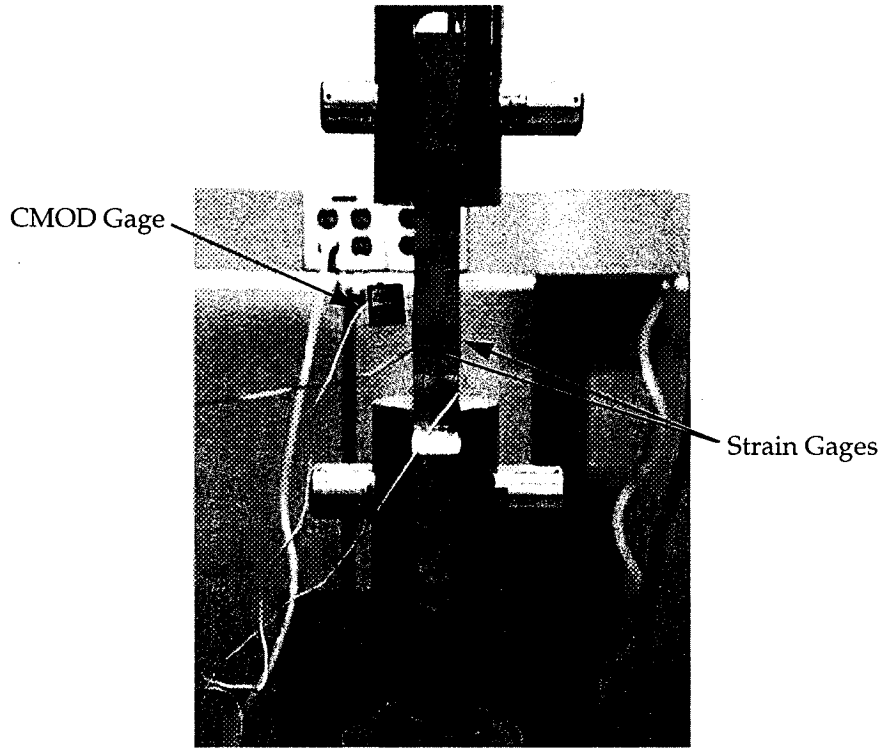

Figure 41: Center cracked panel test setup.

Testing was conducted in displacement control since it was predicted that the final desired load would occur during the load shed phase (beyond maximum load). A displacement rate of 5×10^{-4} inches per second was utilized so as to limit rate effects. Displacement continued until the measured CMOD at the clip gage reached a desired level. The first four tests concluded at a CMOD of 0.04 inches (1 mm). The fifth test was run to a CMOD of 0.06 inches (1.5 mm). These crack mouth opening displacements were chosen based on analysis to obtain a specific amount of ductile crack growth.

Once the desired crack mouth opening displacement occurred, the specimen was unloaded and removed from the test fixture. The current position

of the crack front and hence the amount of crack growth was then marked by heat tinting by placing the specimen in a furnace at 570°F (300°C) for 30 minutes as detailed in Section 8.3.4.2 of the E813 ASTM standard. The exposed surfaces of the specimen developed a slightly orange colored oxide layer as it air cooled to room temperature. The specimen was then notched from the outside to reduce the remaining ligament and therefore, load required for fracture. Finally, the specimen was placed in a dewar of liquid nitrogen, replaced in the test fixture, and quickly loaded until fracture occurred. Breaking the specimen at low temperature reduced distortion of the crack plane. In addition, a slight change in morphology occurred as a result of fracture at low temperature, and in combination with heat tinting, provided extremely good definition of the experimental crack front. This simplified the process of measuring its shape and the crack length at several locations through the thickness.

5.10 Microscopy

Metallography was performed on the pre-test weld material to verify the grain size and porosity size and spacing. The inclusion volume fraction was determined by lightly etching the polished surface. A 5% Nital etchant was applied for 5-10 seconds. This allowed for some of the grain structure to show through, but more importantly, provided a deep contrast to inclusions. A sample weld metal photomicrograph is shown in Figure 42.

Examination of the fracture surfaces was conducted using several different techniques. First, photographs ranging from 4x to 20x were taken using a 4x4" macro camera system. Examinations were also conducted using a light microscope and a Cambridge StereoScan 360 scanning electron microscope. These

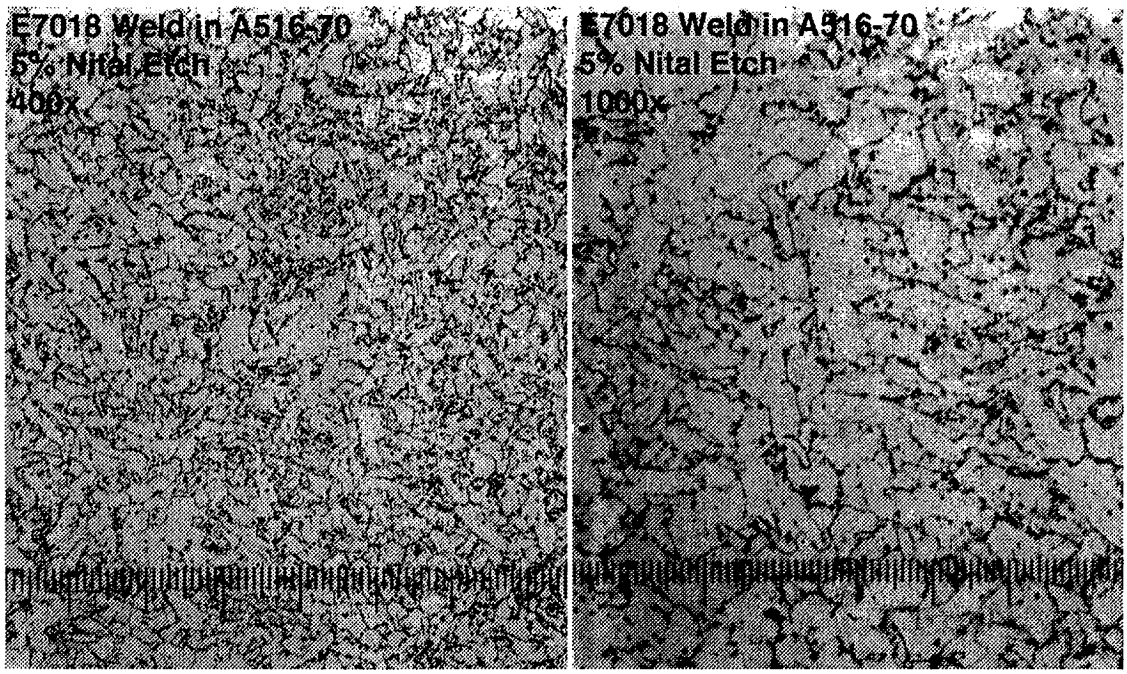

Figure 42: Weld micrograph showing hard particle (carbide) inclusions.

different systems allowed for measuring the crack front length, examination of precrack shape and length, and measurement of dimple size and distribution.

Metallographic examination was also conducted on many of the plate and weld samples, according to ASTM Standard E3: Standard Methods of Preparation of Metallographic Specimens.[4] Specimens were mounted in Bakelite, and alumina polished to a 0.1 micron finish. These specimens were then etched with a 5% Nital solution, revealing grain boundaries. Grain size was then measured per ASTM E112, Standard Test Methods for Determining Grain Size.[6]

Grain size was determined by continuing the etch performed in determining the void volume fraction. The same etchant, 5% Nital, was applied, for an additional 25 seconds. This revealed the weld grain structure shown in Figure 43. Columnar grains in the weld region possessed an aspect ratio of approximately 1 to 8, measuring on average 0.019 inches (0.5 mm) in length.

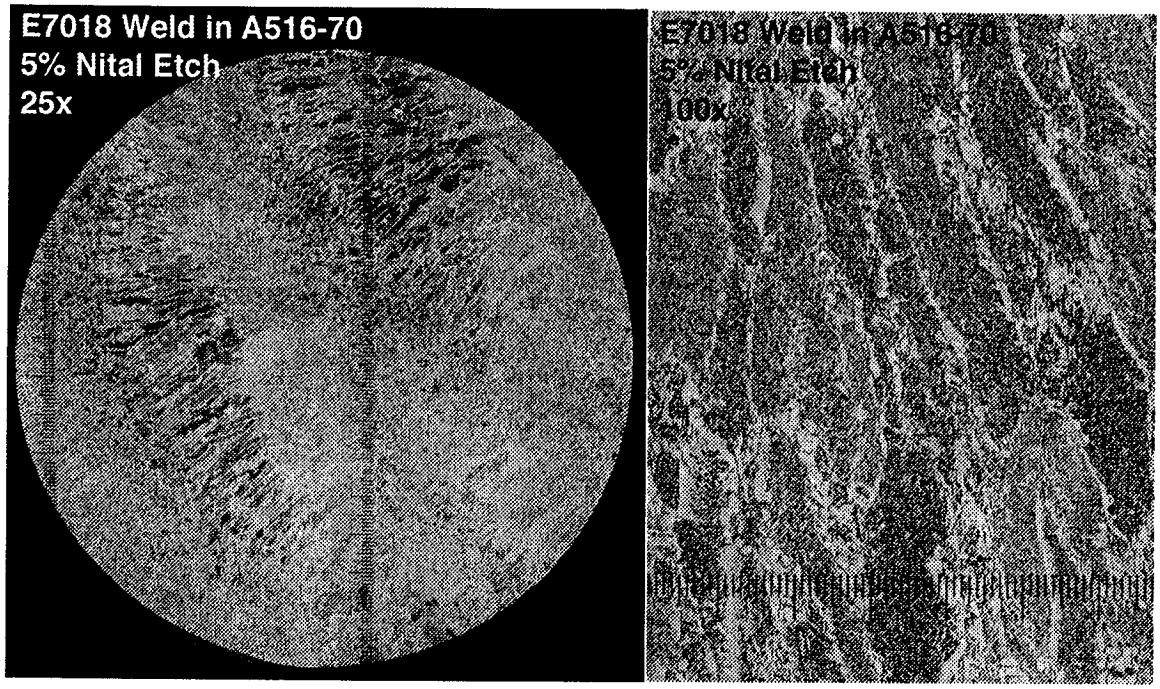

Figure 43: Weld grain structure after etching with 5% Nital.

Examination of both pre- and post-test weld micrographs and fractographs showed an inclusion area fraction of approximately 0.0016. This inclusion area fraction only included manganese sulfide inclusions measuring more than 5×10^{-5} inches (1.3 μm) in diameter.

Chapter 6

Finite Element Modeling

For this study, the finite element method forms the basis of prediction and verification of crack growth in experimental specimens. Application of the finite element method requires that the stress-strain response of all modeled materials be known. Additionally, in crack growth studies, the element length is a material parameter and must be determined.

Standard finite element methods assume homogeneous materials and do not account for large scale plasticity as the material deforms. To facilitate the prediction of crack growth, a new finite element code was utilized which accounts for large scale plasticity and advances the crack tip through a method of element stiffness reduction based on a void growth model. This program, Warp3D[16], developed at the University of Illinois, was used as the primary finite element code in this study. Analysis was performed on both a DEC AlphaStation 250 and the NASA-Ames Research Center Aeronautics Consolidated Supercomputing Facility (ACSF) Cray YMP-C90.

6.1 Finite Element Software

Warp3D only supports the use of an 8-node isoparametric element, or "l3disop", to describe a given structure. As this element is three-dimensional, two-dimensional structures are modeled as very thin three-dimensional structures with boundary conditions imposed on the two out-of-plane surfaces.

Since the experiments were all performed under quasi-static loading condi-

tions, all model loading was performed under displacement control, wherein a forced displacement was applied at nodes corresponding to the load point. This method also lends itself to improved efficiency of the numerical solution methods employed by the program.

The Gurson-Tvergaard model of void growth incorporated in Warp3D was utilized to perform ductile crack growth analysis. In this model, the yield surface grows as strain hardening occurs, but then decreases as void volume fraction increases. Once the subcritical void volume fraction of 0.1 is reached in an element, the element stiffness is reduced until the void volume fraction reaches a critical level of 0.15. At this time, the element is "killed" such that the stiffness, and therefore the load carrying capacity of the element, is reduced to zero. Even though an element is killed, Warp3D does not eliminate the element from the finite element model.

6.2 Modeling Software

All of the models for this study were created in P3/PATRAN, a geometric pre- and post-processor from MacNeal-Schwendler (MSC) Company Ltd. The models were first output as platform independent (neutral) element description files and then converted to Warp3D scripts via the Warp3D conversion routine Patwarp. Results from Warp3D were post-processed using PATRAN. The PATRAN software was executed on a DEC AlphaStation 250 workstation.

6.3 Material Stress-Strain Properties

Basic material parameters had to be determined before finite element modeling could begin. Obviously, one must know how a material reacts to the

application of load before one can determine the stresses and strains in a body. Tensile testing was conducted on smooth round bar specimens, the results of which were presented in Chapter 5. Piecewise linear representations of these curves were then applied to the finite element model. However, before this could be done, adjustments had to be made to the test data, to account for finite element stiffening.

In some cases, finite elements tend to be stiffer than their physical counterparts. To estimate the magnitude of the stiffening effect, the initial piecewise linear flow curve, based on the uniaxial stress-strain results, was entered into a finite element model of the small notched tensile specimen. The flow curve was then adjusted so that the diametral contraction results of the analysis matched the experimental results from notched tensile testing. (Experimental testing is discussed in Section 5.5.)

The notched round-bar tensile specimens were modeled as three-dimensional quarter models as shown in Figures 44 and 45. Face normal boundary conditions were applied as shown to provide the reflected portions of the model. This was necessary to make up for the lack of an axisymmetric element in Warp3D. A displacement loading condition was applied to the end of the model to simulate displacement controlled loading.

Based on results of the small notch finite element analysis, the original piecewise linear flow curve was decreased slightly, so that the finite element analysis matched the diametral contraction results. The finite element results after adjusting the stress-strain curve are shown in Figure 46. To verify the effect of these changes, a similar analysis was performed using the adjusted piecewise linear flow curve on the large notch tensile specimen. The results of these tests are shown in Figure 47. The adjusted piecewise linear flow curves for both plate and

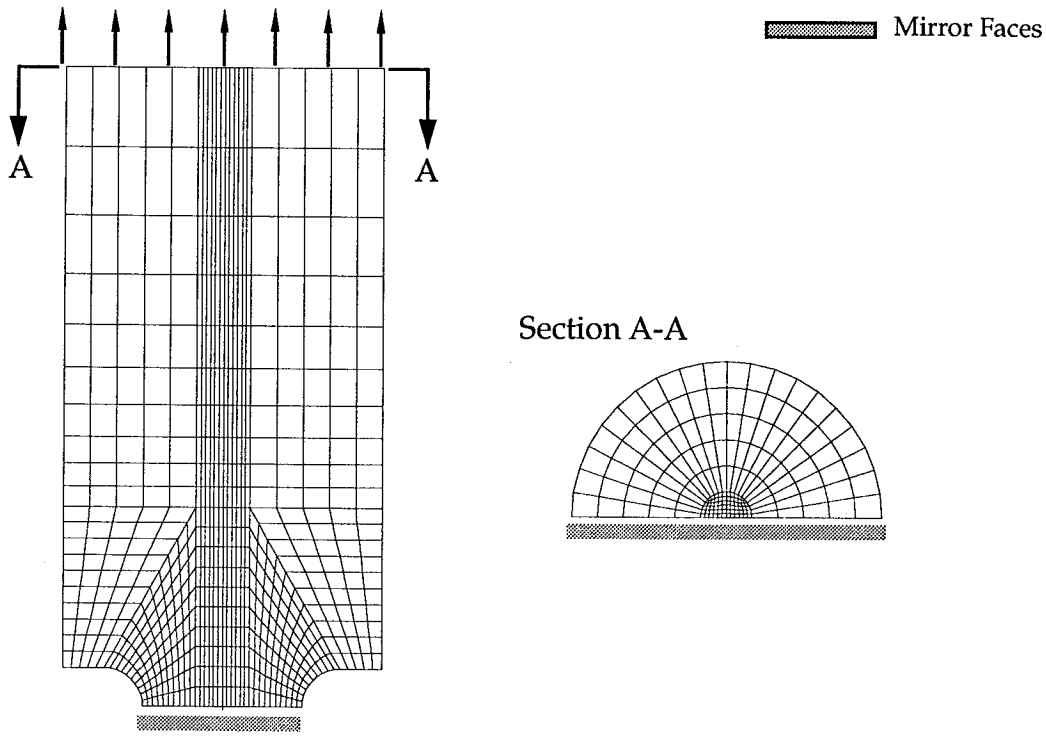

Figure 44: Small notched round-bar tensile specimen.

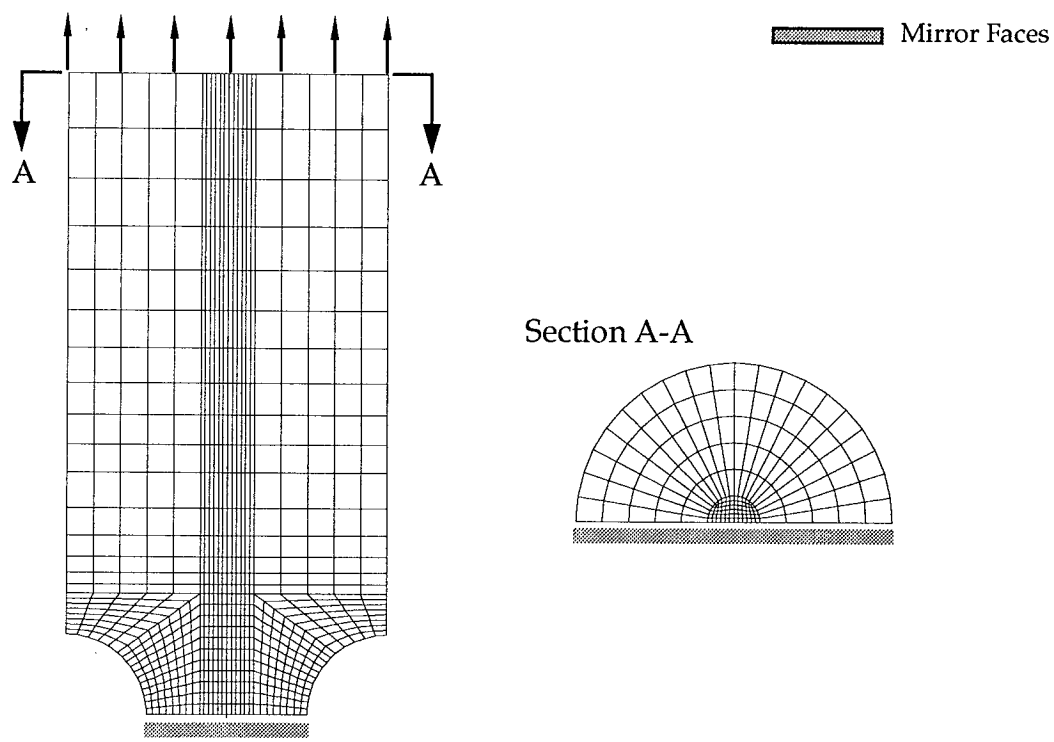

Figure 45: Large notched round-bar tensile specimen.

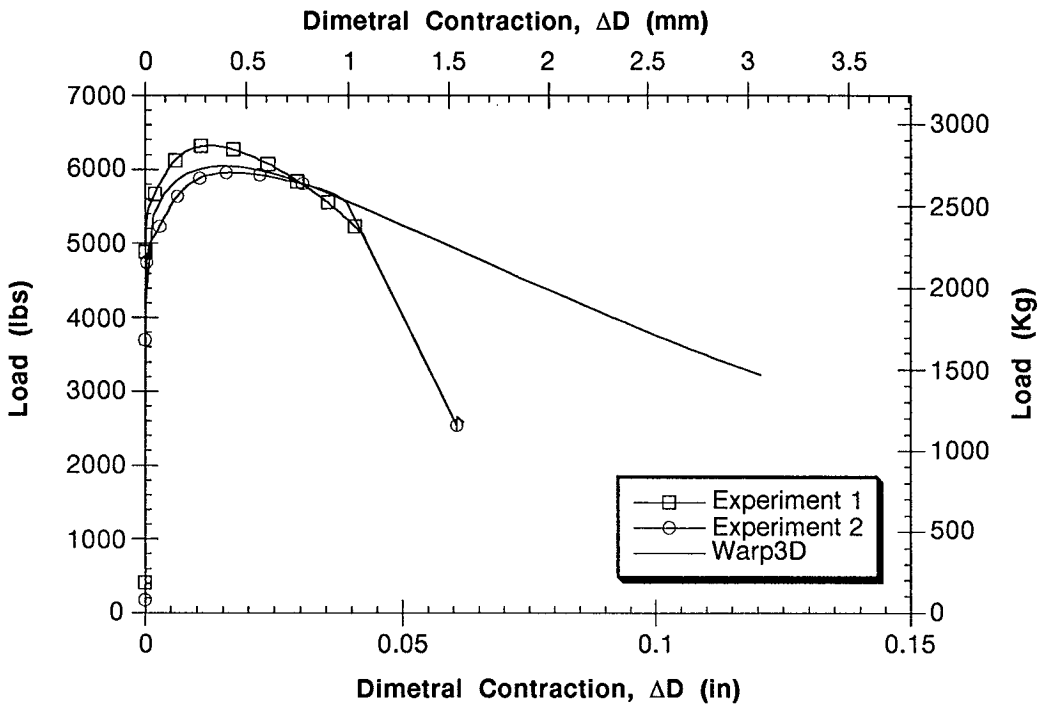

Figure 46: Comparison of stress-strain experimental and analytical results for small notched specimens. (duplicate tests)

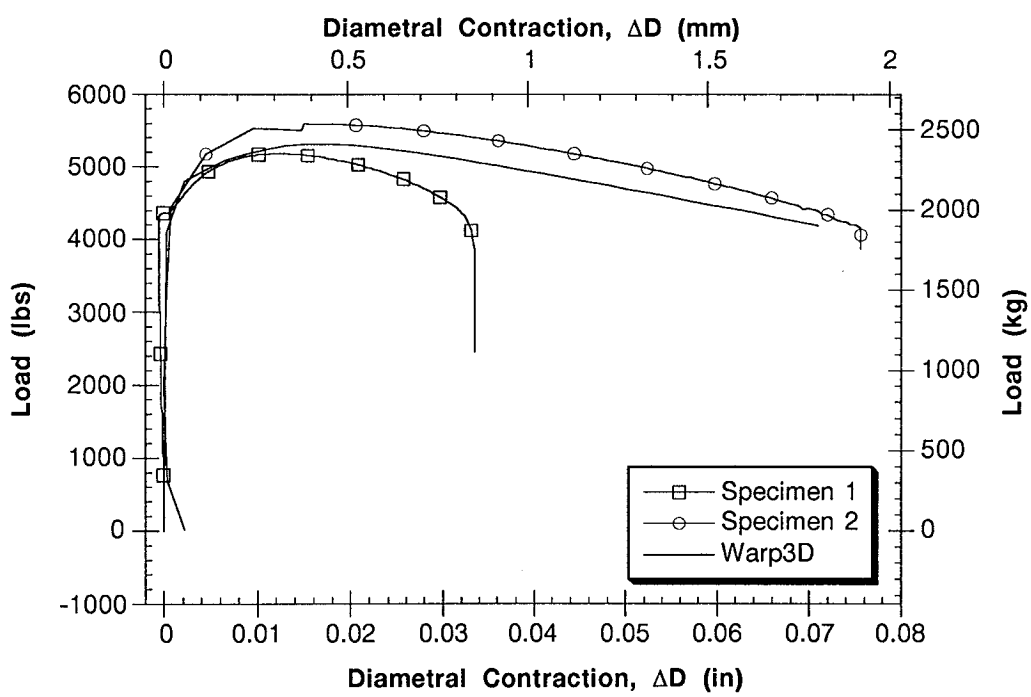

Figure 47: Comparison of stress-strain experimental and analytical results for large notched specimens. (duplicate tests)

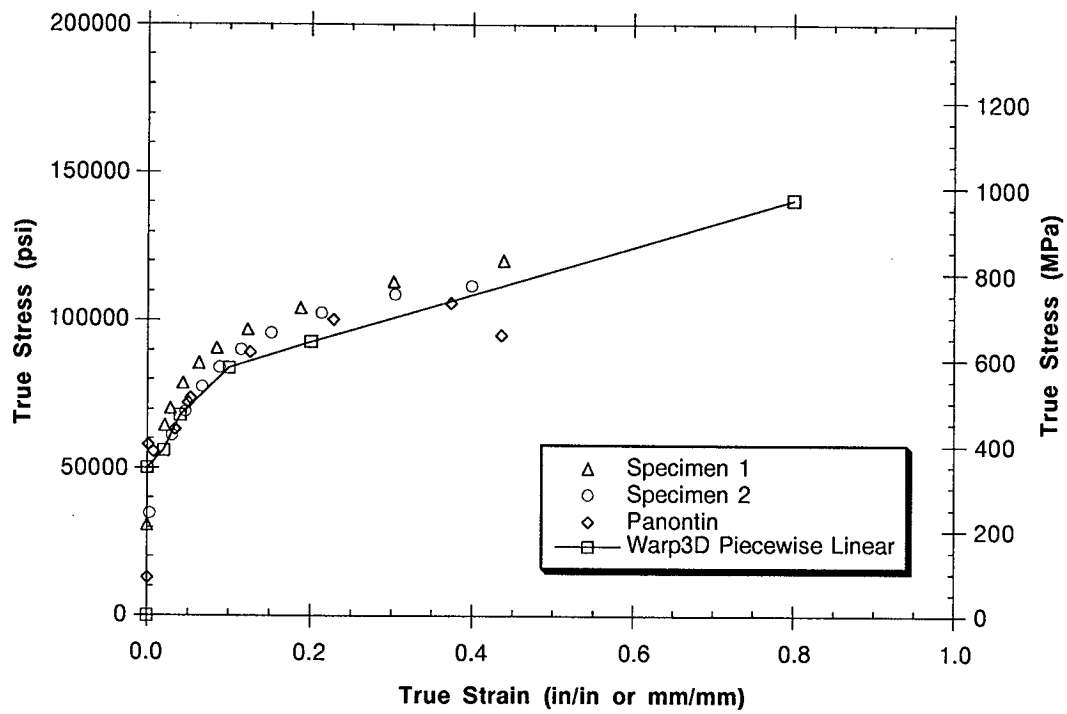

Figure 48: Base metal piecewise linear flow curve used in finite element analysis, adjusted for element stiffening. Original experimental data shown for reference.

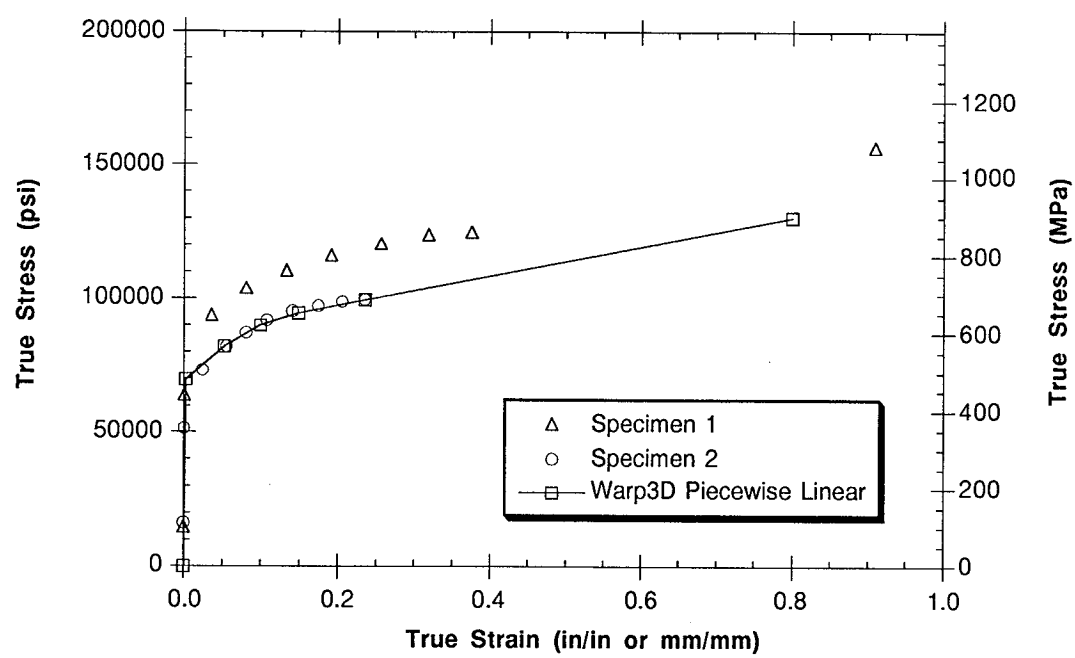

Figure 49: Weld metal piecewise linear flow curve used in finite element analysis, adjusted for element stiffening. Original experimental data shown for reference

weld metal are shown in Figures 48 and 49, respectively. Numerical values for these curves are included in Appendix C. The adjustments and stiffness calibrations for the plate metal were conducted by Panontin.[41]

6.4 Element Sizing (The Material Characteristic Length)

Finite element analysis using the Gurson micromechanical model requires that the elements along the crack front have dimensions equal to the material characteristic length. This is the length over which void coalescence must occur prior to crack propagation. Therefore, before finite element modeling can begin, the material characteristic length must be known.

The material characteristic length can be determined using a number of different methods, some theoretical and others, phenomenological. Two methods are presented here. The first method involves microscopic examination of fracture surfaces and metallography. A second method combines experiment and analysis, and uses the stress modified critical strain criterion for fracture initiation. In this research, the stress modified critical strain criterion was applied to single edged bend specimens to estimate the characteristic distance.

6.4.1 Metallographic and Fractographic Method

The metallographic methods used in this study are those of Schwalbe[46] and Garrison[23] as detailed in Section 3.7.

The dimpled surface shown in Figure 50 is characteristic of the fracture surfaces observed during testing of weld material. The entire surface possesses a fairly uniform and fine dimple rupture pattern typical of ductile failure. Within the dimples, small manganese sulfide particles can be seen. Interfacial decohesion of these inclusions creates the dimple rupture appearance of a ductile fracture

surface. However, dispersed randomly throughout the uniform surface is a small number density of larger inclusions, each measuring 5-10 times the diameter of the small particles. Interfacial decohesion is less likely at larger particles since they have a higher interfacial cohesive strength than small particles. However, large particles tend to fracture before decohesion of small particles occurs.[2] Therefore, it is suspected that these larger inclusions drive the failure mechanism and therefore should be used in the characteristic length determination.

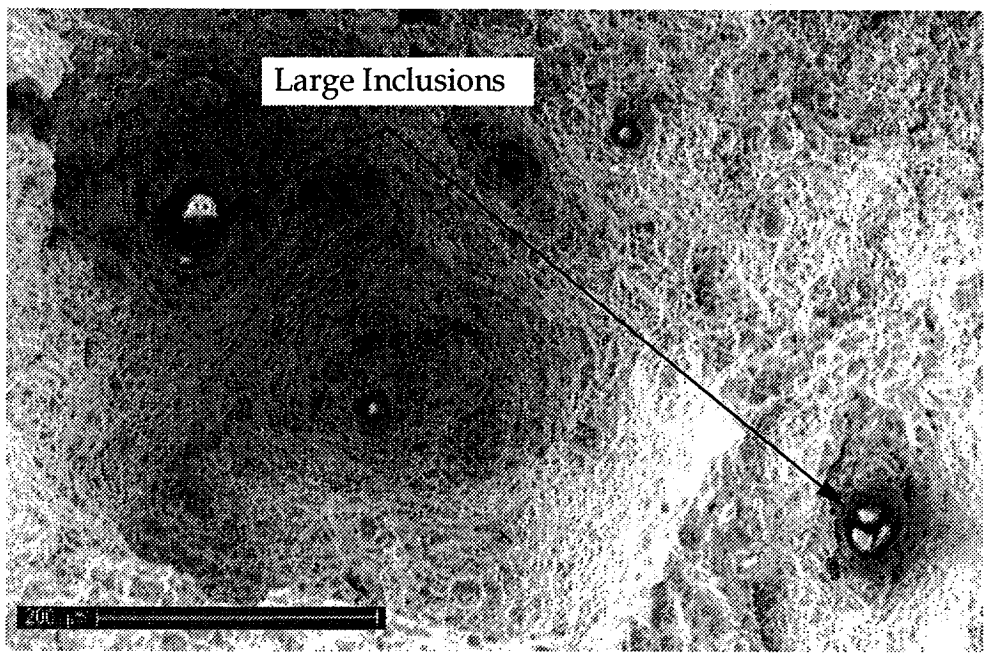

Figure 50: Fracture surface showing large (20 μm) inclusions surrounded by uniform smaller (2 μm) inclusions.

As shown, the section depicted in Figure 50 covers an area of 0.0006 square inches (0.387 mm^2). Within this area, 2 inclusions with a mean diameter of 7.9×10^{-4} inches (2.0×10^{-2} mm) were counted. Substituting into Equations 23 and 24 yields:

$$f_{0_a} = \frac{2 \times \pi \left(\frac{7.9 \times 10^{-4}}{2} \right)^2}{0.030 \times 0.020} = 0.0016 \tag{31}$$

$$f_{0_a} = f_{0_v} = 0.0016 \tag{32}$$

and the initial inclusion volume fraction, f_0, is 0.0016. A mean particle spacing of 0.007 inches (0.18 mm) can then be computed through Equation 26 as:

$$X_0 = \frac{0.36(7.9 \times 10^{-4})}{\sqrt{0.0016}} = 0.007 \text{ in.} \tag{33}$$

The material characteristic length is generally 1-2 times the mean particle spacing,[46] and Panontin found that it was 1.67 times the mean particle spacing for A516-70 steel.[41]

6.4.2 Stress Modified Critical Strain Method

The material characteristic length can also be determined based on the stress modified critical strain failure initiation criterion. In this method, a failure criterion is developed based on mechanical testing of notched tensile specimens[34] with different notch sizes and therefore different levels of constraint in the fracture region. Finite element analysis is then used to determine the triaxiality in the center of the specimen at the load required to initiate fracture, as indicated by a sudden drop in load. This failure criterion is then applied to single edged bend specimens, loaded to the point of crack initiation.[41]

In addition to adjusting the material flow curves to compensate for finite element stiffening, the notched tensile finite element models were utilized in

developing a triaxiality failure criterion for the weld metal. Load at failure for the round bar tensile specimens was determined from laboratory testing and is shown as the failure points on Figures 28 and 29. At the failure load, triaxiality and equivalent plastic or von Mises strain, ε_p, can be determined from the results of the finite element analysis. For the smooth tensile round bar specimen, which was not modeled, triaxiality is assumed to range from 0.3 to 0.5, based on research by MacKenzie.[34] Equivalent plastic strain is taken as the true strain, computed from $\ln(a_0/a)$. This is shown in Figure 51. MacKenzie[34] suggests an exponential curve

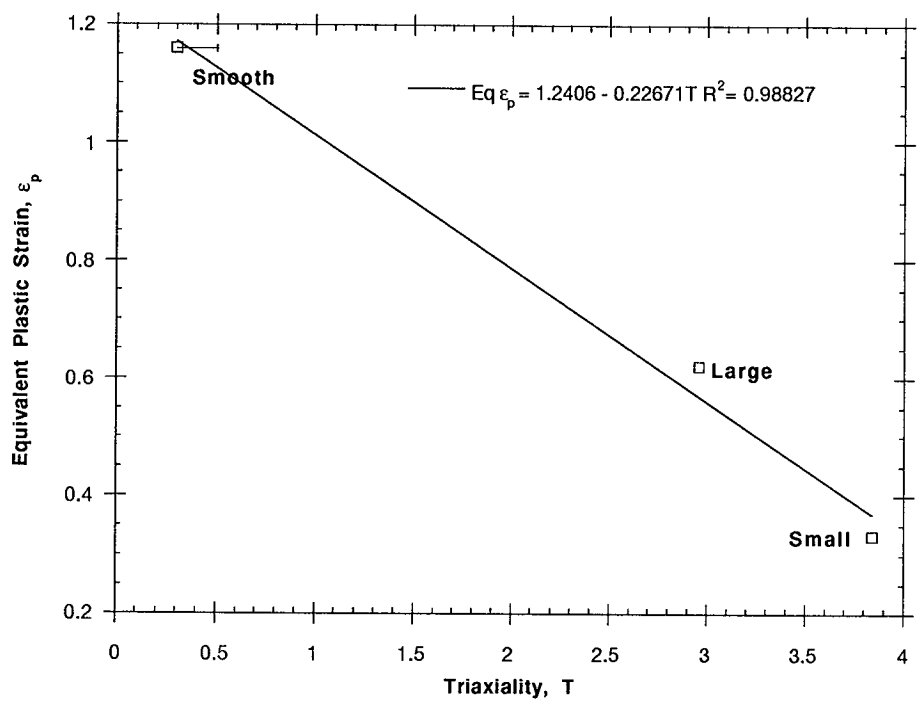

Figure 51: Weld metal failure criterion - equivalent plastic strain vs. triaxiality.

fit for the data of Figure 51. However, it was found that a linear fit was more appropriate to this situation. A least squares linear curve fit provided the equation

of a line:

$$\varepsilon_p = 1.2406 - 0.2267T \tag{34}$$

where T is the triaxiality and ε_p is the equivalent or von Mises plastic strain. The R^2 confidence of the fit was 0.988. The curve represents a failure criterion relating the equivalent plastic strain for failure at a given triaxiality state. For a given geometry, if the level of triaxiality is known, then the failure criterion determines the limiting value of equivalent plastic strain which must be reached or exceeded over the critical length for failure to occur.

The SE(B) specimen model was used to determine the characteristic length of the weld metal. The objective is to load a laboratory specimen to the point of crack initiation. Finite element analysis is then performed on a model of the specimen, up to the crack initiation load. The characteristic length can be determined by comparing the triaxiality and equivalent plastic strain to the failure criterion, at each element in front of the crack tip. Since the applied load is equal to the measured crack initiation load, the length of elements over which Equation 35 is satisfied equals the characteristic distance.

$$\varepsilon_{p(FEM)} \geq \varepsilon_{p(crit)} \tag{35}$$

The SE(B) specimen, shown in Figure 52 consists of elements measuring 0.0005 inches (0.013 mm) along the crack plane. Obviously, if the characteristic length is going to be determined based on the distance from the crack tip to the last element that meets the failure criterion, then the individual element size must be smaller than the characteristic length. For reasons of accuracy, the element size is chosen ten times smaller than the anticipated characteristic length.[41] Therefore,

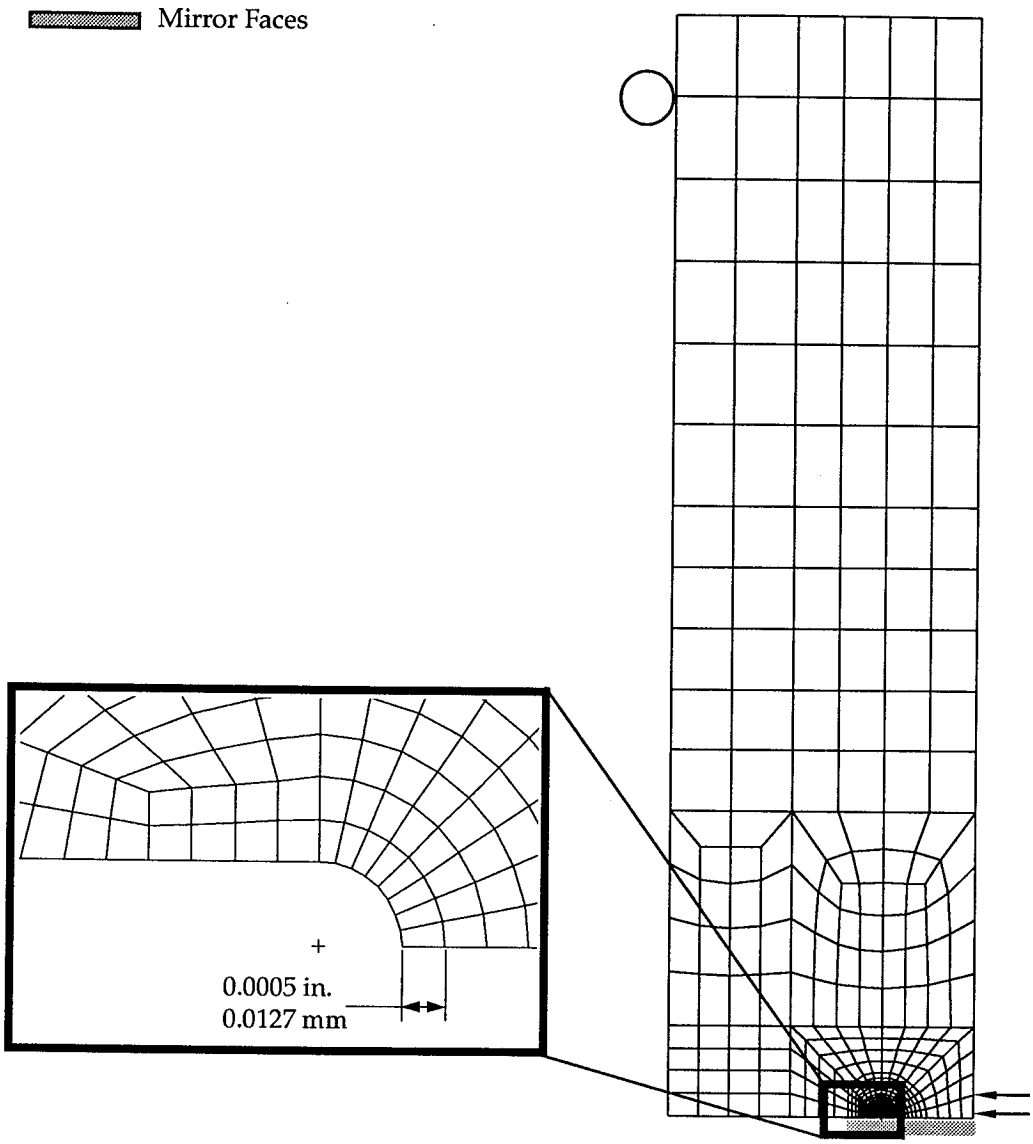

Figure 52: Deep notched (a/W = 0.7) SE(B) specimen model.

the model with 0.0005 inch (0.013 mm) elements would be suitable for calculating characteristic lengths of approximately 0.005 inches (0.13 mm). Measurements by Panontin place the characteristic length for A516 Grade 70 steel at 0.003 inches (0.076 mm).[41] It was hypothesized that the characteristic length for the weld metal would be on the same order of magnitude as the parent A516 steel, and thus the 0.0005 inch (0.013 mm) SE(B) crack front was determined to have a suitable

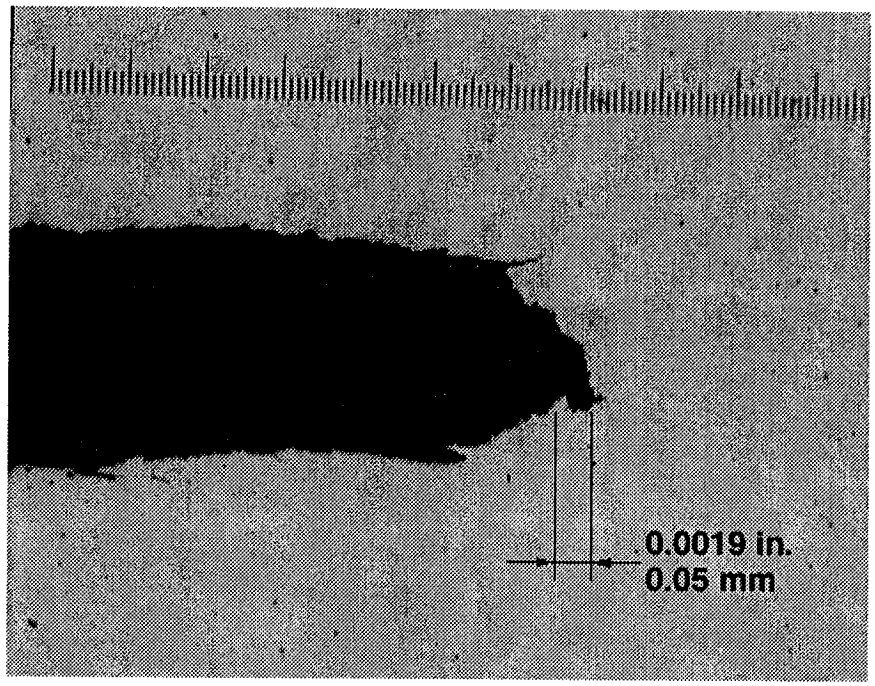

Figure 53: Micrograph of deep notched (a/W=0.7) SE(B) specimen showing fracture initiation. Specimen loaded to CMOD of 0.09 inches (2.3 mm), resulting in a load of123 pounds (55.8 kg).

mesh size resolution.

Analysis of the deep notched (a/W = 0.7) SE(B) specimen was conducted to the crack mouth opening displacement of 0.09 inches (2.29 mm) associated with fracture initiation. This CMOD was determined by matching J_{Ic} from C(T) tests to J obtained from the finite element analysis of the SE(B) specimen. Figure 53 is a micrograph of the crack tip at the midplane of the specimen, used to verify that the crack had initiated.

In order to verify that the SE(B) specimen model was performing correctly, predicted crack mouth opening displacement was compared to the experimental results, as shown in Figure 54. The comparison shows a very good match between the analysis and experimental results, with some error attributed largely to discrepancies in length between the modeled and fatigued crack fronts. The

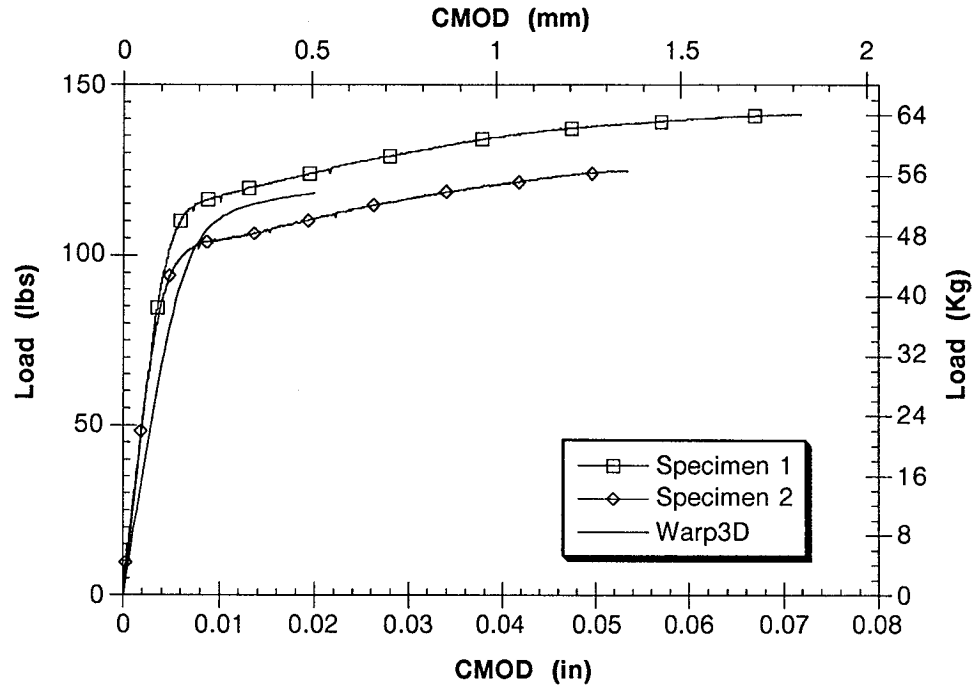

Figure 54: Crack mouth opening displacement for deep notched (a/W=0.7) SE(B) specimens.

analysis results of Figure 54 have been adjusted to compensate for the fact that the knife edges used in testing were not front-face mounted (i.e. not mounted flush with the crack mouth). This was accomplished by assuming a rigid body rotation of the knife edges with the two nodes adjacent to the knife edge mounting location, as shown in Figure 55.

Once it was verified that the model was working properly, triaxiality and equivalent plastic strain were extracted from the finite element results. This was done at several different load steps. Equivalent plastic strain at failure was then computed for all of the elements along the crack front, based on the finite element computed equivalent plastic strain, triaxiality, and the failure criterion of Equation 34. The difference between the FEM predicted equivalent plastic strain and the failure equivalent plastic strain was then determined[41]:

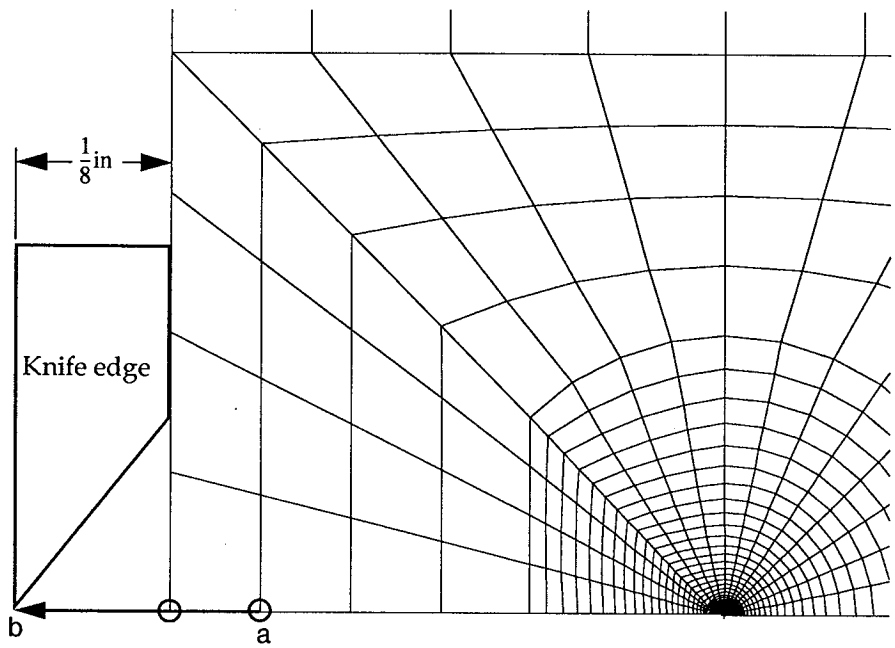

Figure 55: Compensation technique for knife edges not located on front-face. Rotation/location of circled nodes determines position of knife edge via vector a-b.

$$\Delta\varepsilon_P = \varepsilon_{p(FEM)} - \varepsilon_{p(test)} \tag{36}$$

Substituting $\varepsilon_{p(test)}$ from Equation 34 yields:

$$\varepsilon_{p(FEM)} - 1.2406 - 0.22671T \geq 0 \tag{37}$$

In this way, all elements for which the relation of Equation 37 is greater than zero have met the failure criterion. The "equivalent plastic strain difference" was plotted against the undeformed distance from the crack tip, as shown in Figure 56. The characteristic length was determined by measuring the distance from the crack tip to the point where the relation of Equation 37 went to zero. When

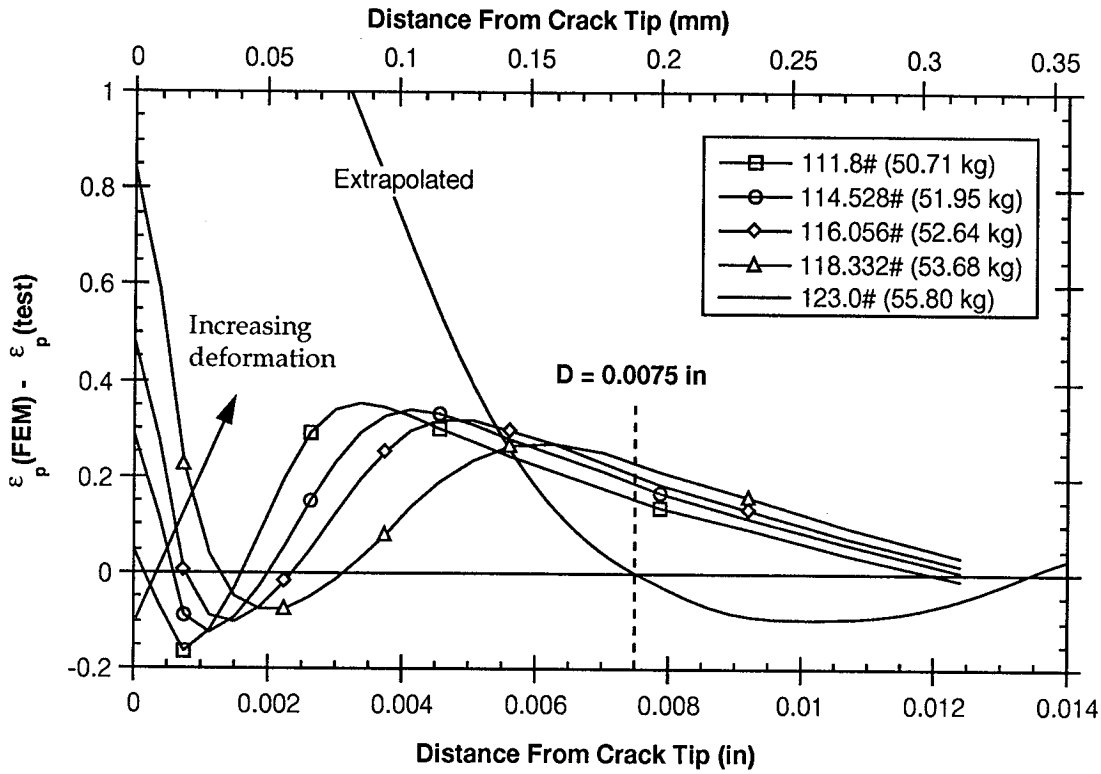

Figure 56: Determination of weld metal characteristic material length through deep notched (a/W=0.7) SE(B) analysis. Curves represent increasing load.

plotting the equivalent plastic strain difference against the distance from the crack tip, as it was in Figure 56, it is important to note that the equivalent plastic strain difference will start out positive, cross the axis, and then oscillate across the axis. This oscillation is an artifact of the method, and does not indicate that failure has occurred in elements with positive oscillations.

Due to an extreme amount of deformation preceding crack initiation in the deep notched SE(B) model, Warp3D was unable to reach the displacement step with a CMOD equal to that associated with fracture initiation. Therefore, the length of failed elements, measured from the crack tip, was plotted in Figure 57, against the crack mouth opening displacement at which they were measured. This was then curve fit with a linear function so that the characteristic length corre-

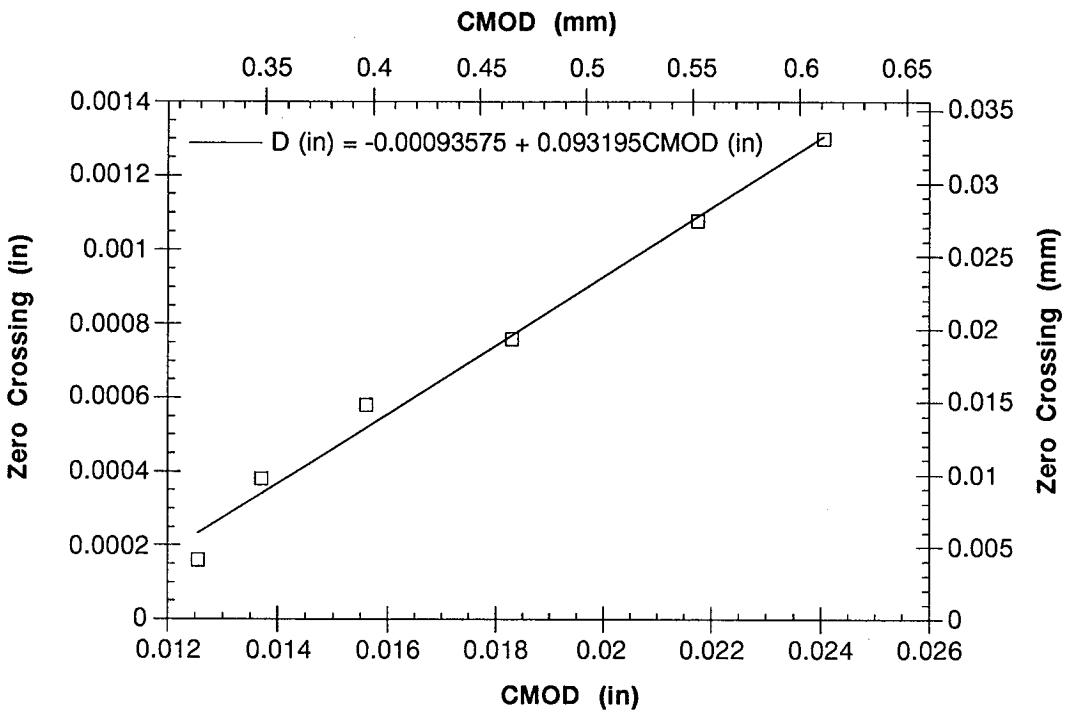

Figure 57: Deep notched (a/W=0.7) SE(B) "Zero Crossing" as a function of CMOD. Used for verification of weld metal characteristic length.

sponding to the crack initiation CMOD could be determined. The result of this extrapolation is reported in Equation 38:

$$D(\text{in}) = -0.000936 + 0.09320CMOD(\text{in}) \tag{38}$$

In the deep notched specimen, the CMOD at initiation was 0.09 inches (2.29 mm). Using Equation 38, D was computed as 0.0075 inches (0.191 mm). This is the preliminary, undeformed, SMCS determined characteristic length. Examination of the crack length shown in Figure 53 does not, however, show 0.0075 inches (0.191 mm) of crack growth. This is a result of the fact that the characteristic length is based on the original, undeformed geometry. As the crack tip blunts, the material along the crack front compresses, thereby changing the relationship of points along the crack front. This can be seen in the model of the deep notched

SE(B). Figure 63a shows the undeformed finite element model of the deep notched SE(B), while Figure 63b shows the deformed shape after loading to a CMOD of 0.024 inches (0.61 mm). As shown, the spacing of the nodes along the crack front changed once the load was applied.

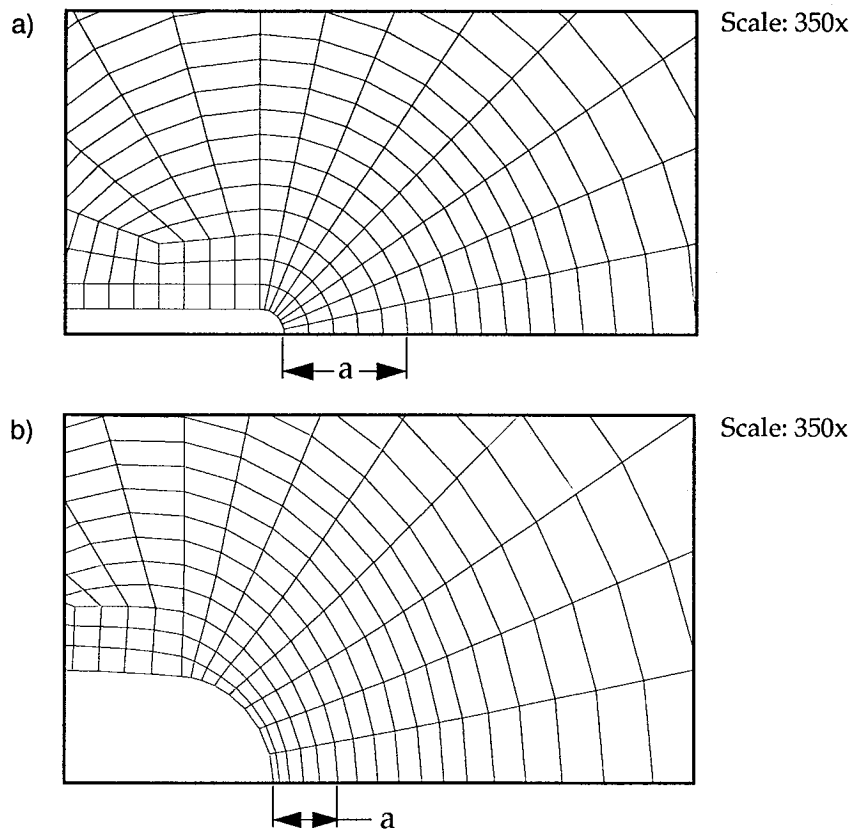

Figure 58: Deep notched (a/W=0.7) SE(B) model: a) undeformed geometry. b) geometry after application of 118.33 pounds (53.68 kg).

To verify the characteristic length calculation from the deep notched SE(B), a second model, that of the shallow notched (a/W = 0.3) SE(B), was also created. This is shown in Figure 59. This time, instead of experimentally determining the fracture initiation load, the CMOD for fracture initiation was predicted using the SMCS criterion and the previously determined characteristic length. At several different displacement steps, the equivalent plastic strain difference was plotted

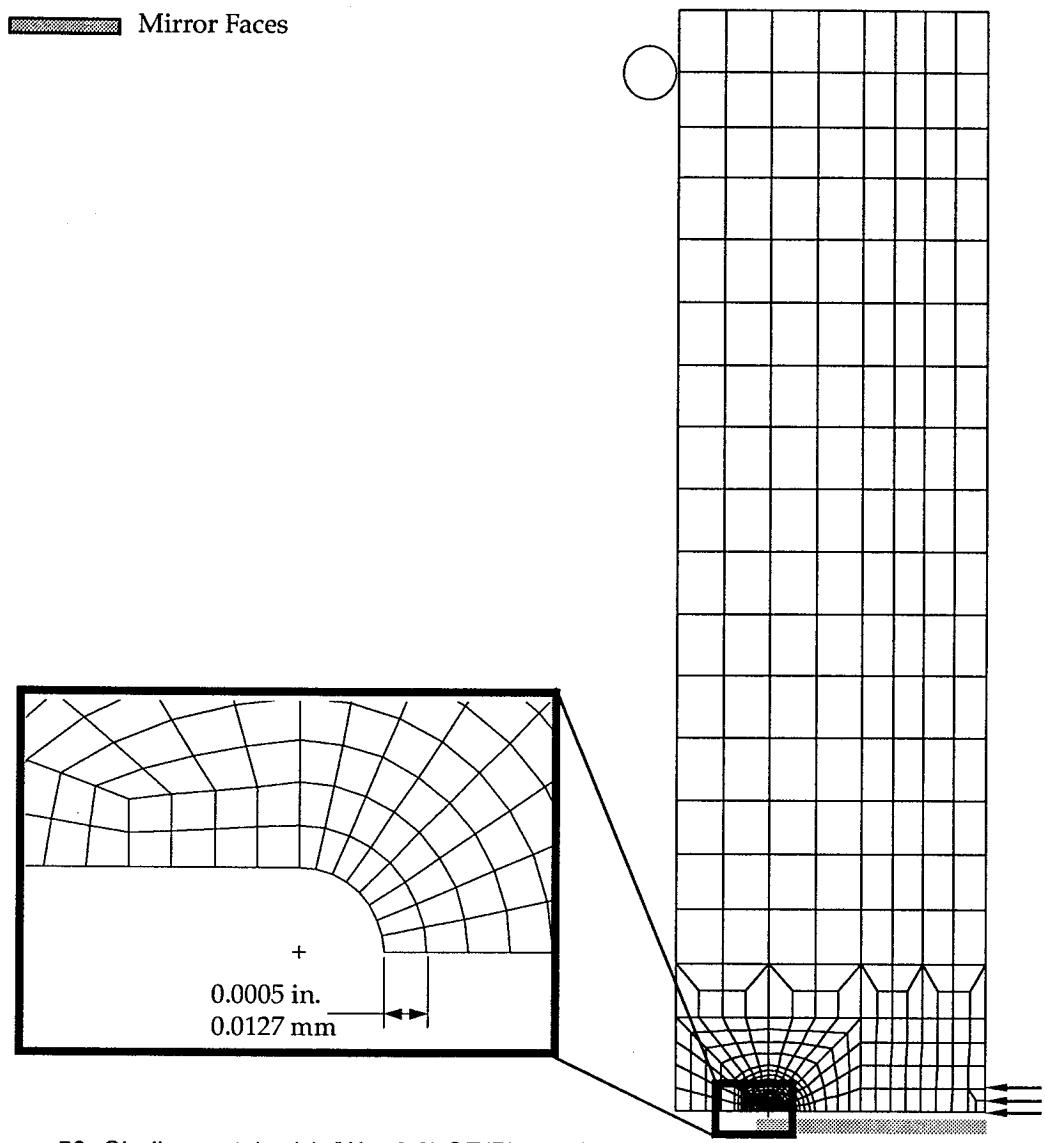

Figure 59: Shallow notched (a/W = 0.3) SE(B) specimen model.

versus distance from the crack tip, as shown in Figure 60. As before, failure has occurred in all elements where the relation of Equation 37 is greater than zero. Ideally, the load and CMOD at fracture initiation could be determined by running the analysis until all of the elements up to the previously determined characteristic length had met the failure criterion. However, as before, due to an extreme amount of deformation preceding crack initiation in the shallow notched SE(B)

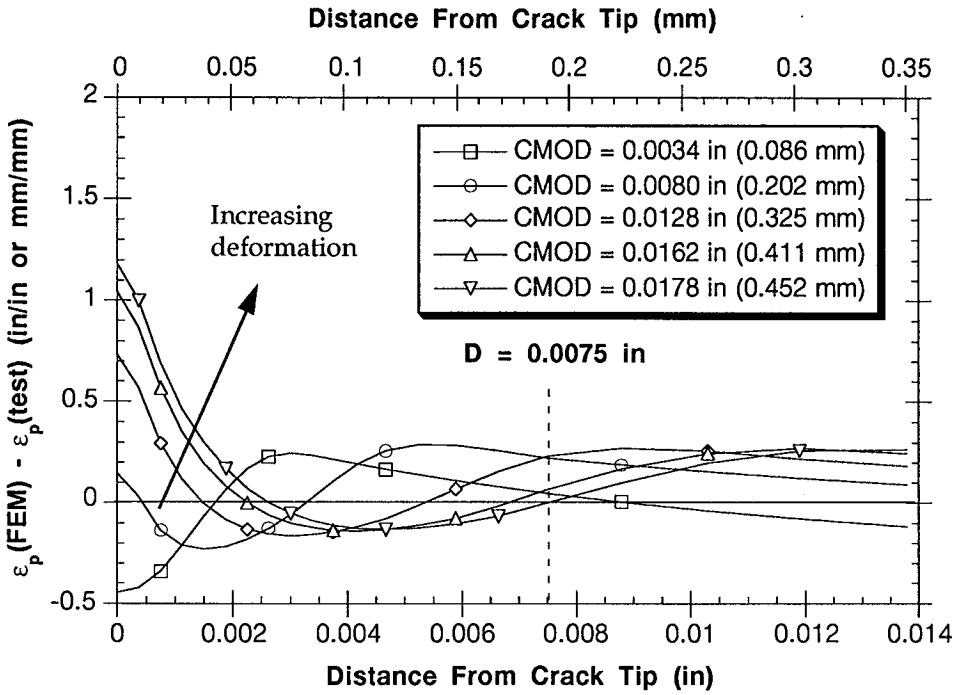

Figure 60: Determination of weld metal characteristic material length through shallow notched (a/W=0.3) SE(B) analysis. Curves represent increasing CMOD or load.

model, Warp3D was unable to reach this displacement step. Therefore, the length of failed elements, measured from the crack tip, was plotted in Figure 61, against the crack mouth opening displacement at which they were measured. This was then curve fit with a linear function so that the CMOD corresponding to the previously determined characteristic length could be determined. The result of this analysis is reported in Equation 39:

$$\text{CMOD (in)} = 0.00646 + 4.2523D(\text{in}) \tag{39}$$

In the deep notched specimen, the characteristic length was computed as 0.0075 inches (0.19 mm). Substituting this value into Equation 39 for D, suggests that a CMOD of 0.038 inches (0.017 mm) is required for crack initiation in the shallow

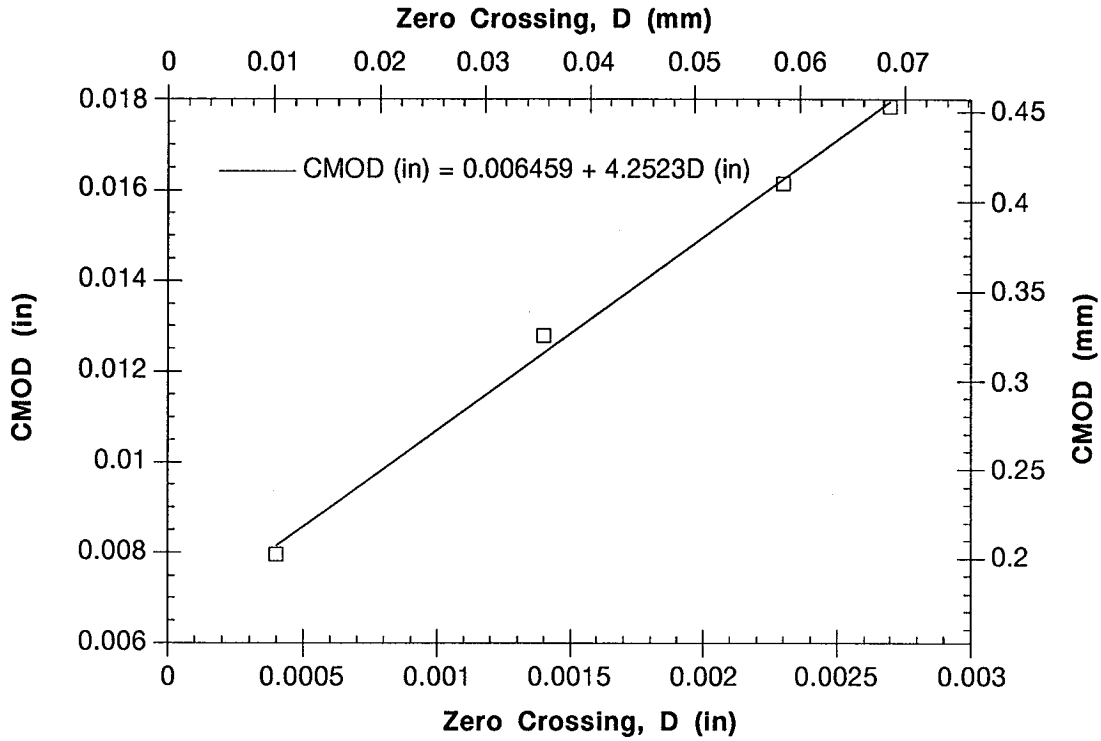

Figure 61: Shallow notched (a/W=0.3) SE(B) "Zero Crossing" as a function of CMOD. Used for preliminary SMCS determined weld metal characteristic length.

notched SE(B). An SE(B) specimen was tested to a crack mouth opening displacements of 0.034 inches (0.017 mm). A micrograph of the crack tip at the midplane is shown in Figures 62. As is indicated in the figure, crack growth has initiated and a fair amount of growth has occurred. In fact, more crack growth than the characteristic length has occurred, suggesting that the actual characteristic length may be shorter than 0.0075 inches (0.19 mm). Generally, the measured length of crack growth is less than the predicted characteristic length. This is due to the fact that the characteristic length is based on the undeformed position, and does not account for material deformation as the crack tip blunts. Figure 63a shows the undeformed finite element model of the deep notched SE(B), while Figure 63b shows the deformed shape after loading to a CMOD of 0.018 inches (0.46 mm). As

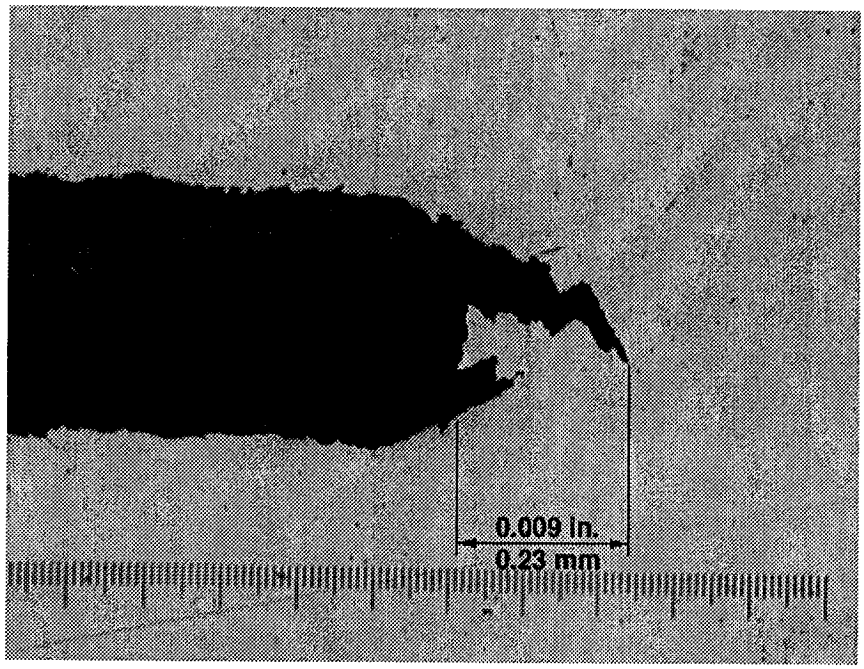

Figure 62: Micrograph of shallow notched (a/W=0.3) SE(B) specimen showing fracture initiation. Specimen loaded to a CMOD of 0.034 inches (0.86 mm), resulting in a load of 644 pounds (292.1 kg).

shown, the spacing of the nodes along the crack front changes as the load is applied.

To insure that the shallow notched SE(B) model had performed accurately, a comparison was made between the predicted and experimental crack mouth opening displacement. This is shown in Figure 64. The large disparity between the predicted and actual crack mouth opening displacement may be the result of the initial crack length being too long. Instead of the required a/W of 0.3, the specimen had an a/W of 0.35. This would also explain why there is more apparent crack growth than previously determined from the characteristic length.

The weld metal characteristic length measured by the SMCS method, is approximately twice the characteristic length of 0.003 inches (0.1 mm) reported for A516-70 steel measured by Panontin.[41]

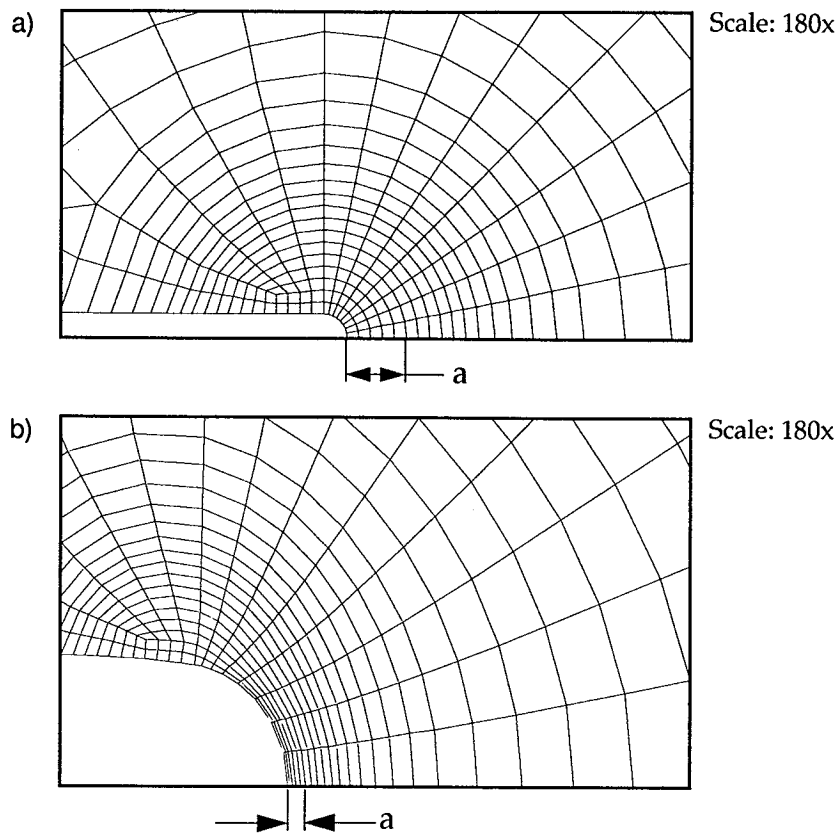

Figure 63: Shallow notched (a/W=0.3) SE(B) model: a) undeformed geometry. b) geometry after loading to a CMOD of 0.018 inches (0.46 mm).

The stress modified critical strain method of determining the weld metal characteristic length, predicted a characteristic length 1.36 times the mean inclusion spacing determined through metallographic techniques. Generally, the characteristic length is between 1-2 times the mean inclusion distance, thus the SMCS measured characteristic length is of the correct order of magnitude. Some discrepancy in the metallographically measured mean inclusion distance is expected however, and is most likely the result of a large variation in size of inclusions in the weld metal, as well as a variation in weld location within which crack growth occurred. In many examinations of weld fracture surfaces, it was observed that there was a fine dispersion of small inclusions with a 1.57×10^{-4} inch (4 μm)

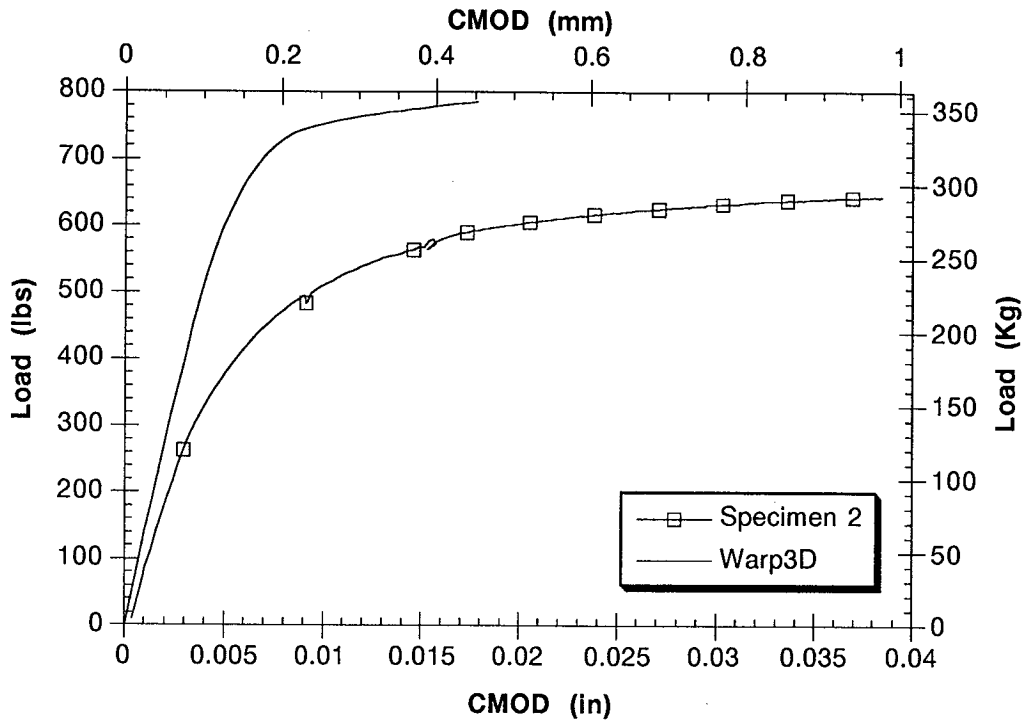

Figure 64: Crack mouth opening displacement for shallow notched (a/W=0.3) SE(B) specimens.

nominal diameter, overlaid with a random dispersion of larger inclusions with a nominal diameter of 7.87×10^{-4} (20 μm). It is hypothesized that it is the larger inclusions that drive the failure process in specimens where large inclusions are present. It is possible that the density of large inclusions in the examined fractographs, was not representative of their actual density, and that their distribution is unpredictable.

Chapter 7

Finite Element Analysis Calibration and Experimental Results

Calibration of the finite element model was accomplished though the testing and modeling of compact tension specimens. Mechanical testing of smooth and notched tensile round-bars provided the flow curve for both the parent[41] and weld materials. In Chapter 6, the material's characteristic length was determined. This information was then incorporated into the compact tension finite element model as material parameters and crack tip element size. The initial volume fraction of inclusions is the final remaining material parameter for the Gurson-Tvergaard void growth model that this study will examine.

In the Gurson-Tvergaard void growth model, void growth occurs from an initially present spherical void. In real materials, void growth can occur at existing voids, inclusions, and second phase particles. Therefore, the volume fraction of inclusions, voids, and second phase particles must be considered when determining the initial void volume fraction.

The initial void volume fraction can be determined experimentally by microscopic examination of dimple spacing on the fracture surface of tensile specimens. Likewise, inclusion site density can be measured from micrographs of etched surfaces. Although there are statistical methods for computing inclusion and void density based on two dimensional cross sections, there is little evidence to suggest which inclusions or voids will link to propagate a crack. Additionally, inclusions come in different shapes and sizes, making their effective density hard to estimate.[23,45,46] Some adjustment of these parameters must be performed,

however, since it has been found that for a given material, the contribution to crack growth from inclusions and voids, is dependent on their size and distribution.

The initial void volume fraction for the weld material was determined from metallurgical measurements as part of the characteristic length determination in Section 6.4.1, and found to be 0.0016. This value was refined by comparing results from finite element analysis of C(T) specimens to experimentally measured J-R curves and crack front profiles, making adjustments as needed. After several iterations, it was determined that the optimal initial void volume fraction for weld metal was 0.001. The welds used in the fabrication of the test specimens for this study were specified as high quality welds, which generally have a lower inclusion density than found in the base metal. Consequently, the initial void volume fraction for the weld metal was found to be significantly lower than that of the A516 plate metal. Ruggieri showed that the A516 plate metal possessed an initial void volume fraction of 0.002.[43]

7.1 Two Dimensional Modeling

Prior to performing any three dimensional finite element analysis on specimens where crack growth was being modeled, two dimensional analyses were run. The two dimensional analyses were invaluable in that they ran much faster, thereby producing results which could be quickly checked against experimental solutions. For example, a full three dimensional model of the center cracked panel took longer than 20,000 seconds (5 hours, 23 minutes) to run on the Cray, whereas a two dimensional analysis on the DEC AlphaStation 250 ran to the same displacement step in approximately 9,000 seconds (2 hours, 30 minutes).

Two dimensional models in Warp3D are different from standard two

dimensional analyses in that the modeling elements are still 8 noded isoparametric bricks. In the two dimensional analysis, in addition to displacements and single point constraints, out of plane constraint is placed on the front and back face of every element. The entire model is as thick as the characteristic element length, so that the crack tip elements are essentially square. Since out-of-plane motion is constrained, the result is a plane strain analysis.

Since crack growth adds a level of complexity to the problem of solving deformation plasticity problems, the first two dimensional analyses were performed with no crack growth. These solutions were compared to experimental results from specimens where the notch was cut to the initial crack length, a_0, and loading did not cause significant crack extension. Once it was determined that the model and software was performing correctly without crack growth, crack growth was enabled.

The results from the two dimensional analysis with crack growth were again compared to experimental results to determine that everything was running correctly.

The three dimensional model was then prepared by extruding the two dimensional model in the thickness direction. This method of proceeding from no crack growth to crack growth, and two dimensions to three dimensions, saved a significant amount of analysis time.

7.2 Compact Tension (CT) Model

The compact tension specimen was modeled as a quarter model with the reflective boundary conditions shown in Figure 65. The model, illustrated in Figure 66, is made up of seven layers, with a 10 to 1 aspect ratio between the

thickness of the midplane and outer layers. Smaller layers were placed towards the outer surface so that low constraint, out-of-plane deformation could be more accurately modeled (See Figure 66). Displacement conditions were imparted on the nodes surrounding the load point to best simulate the test conditions of displacement controlled loading. Linear elastic material properties were assigned to those elements located adjacent to the load point to eliminate punch problems. Simply put, a punch problem is a finite element condition that occurs at singularities such as load points and single point constraints, wherein a large amount of computational cycles are expended determining the deformation and stresses at the singularity. Placing linear elastic elements directly beneath the singularity can eliminate this undesirable punch condition.

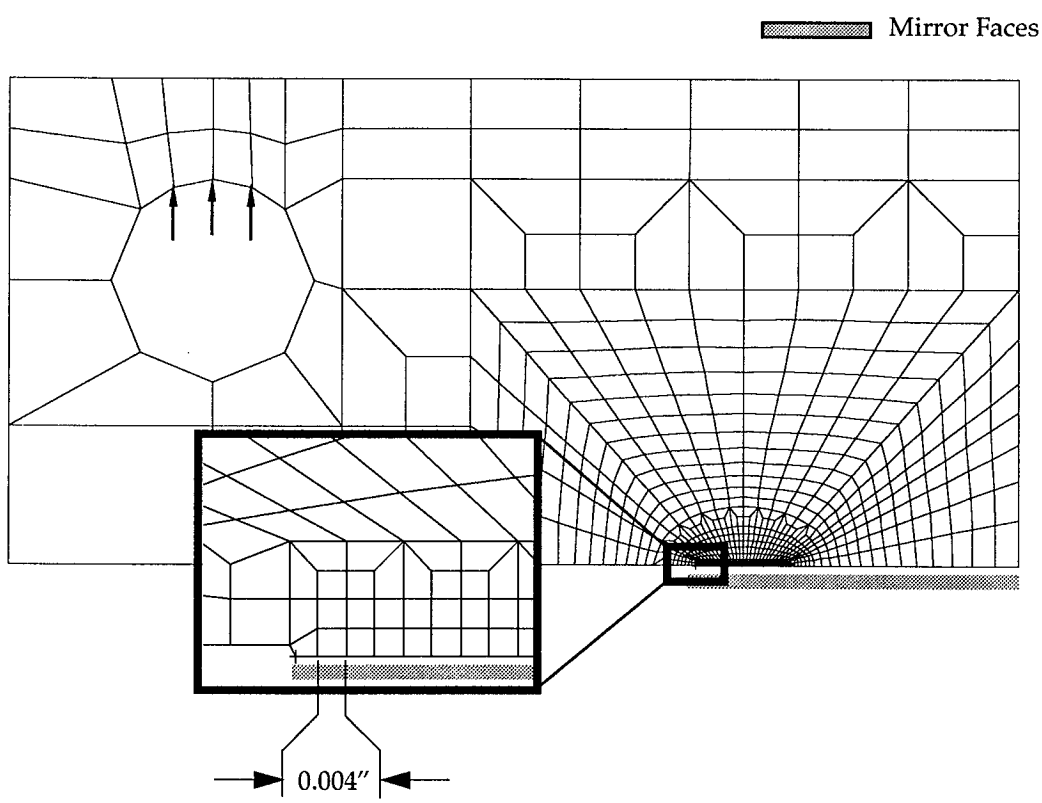

Figure 65: Compact tension specimen model.

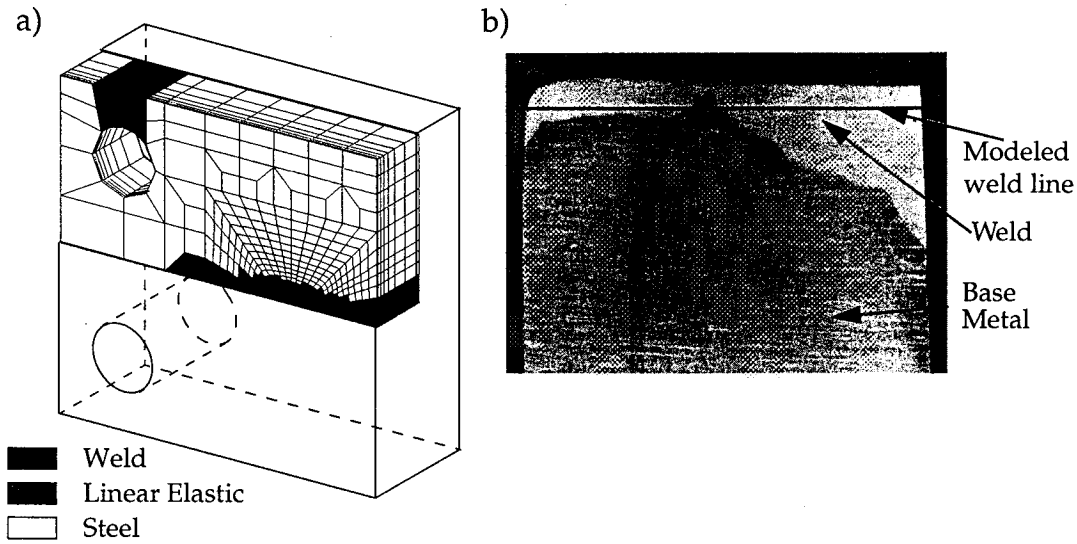

Figure 66: Compact tension model: a) The parent metal, weld, and load application regions were assigned different material properties, as indicated by the shaded regions. b) The actual specimen end-view, etched with 5% Nital to reveal location of crack plane in weld. Line indicates modeled fusion line.

Other material properties, such as those for the weld were applied as shown in Figure 66a. Figure 66b shows the actual fusion line of Specimen 3T, macro-etched with 5% Nital to provide contrast with the base steel. Although the weld geometry varies from the surface to the center as shown in Figure 66b, an average through-thickness weld was assumed, in order to simplify modeling.

The crack front mesh for the compact tension specimens was based on the weld metal characteristic length information obtained in Section 6.4. Metallographic and experimental (SMCS) data suggested that the weld metal characteristic length was approximately 0.0075 inches (0.19 mm). Therefore, according to the Gurson-Tvergaard model, the element size should have been 0.0075 inches (0.19 mm). However, using such large elements would have a detrimental effect on the accuracy of stress and strain computations in the crack growth elements. Therefore, an element size of 0.004 inches (0.1 mm), approximately half

the characteristic length, was selected as a compromise. Ruggieri[43] states that the element size, L, and the initial void volume fraction, f_0, are not a unique pair of parameters that will result in a good J-R solution. Therefore, an element size smaller than the characteristic length can be balanced against a larger initial void volume fraction. It is important to note, however, that there exists a fairly narrow band of L - f_0 combinations which result in a good J-R solution while remaining physically reasonable. Generally element size and the characteristic length are on the order of half the initiation crack tip opening displacement.[43] The SE(B) CTOD at initiation, based on the 90° included angle method, was 0.016 inches (0.41 mm) as shown in Figure 67. Therefore, the element size and characteristic length should be on the order of 0.008 inches (0.20 mm), suggesting that 0.004 inch (0.10 mm) elements are sized reasonably.

As with the SE(B) and tensile round-bar models, the C(T) model utilized both plate and weld material property curves. These curves are shown in Figures 48 and 49. The analysis was run and comparisons were made to experimentally

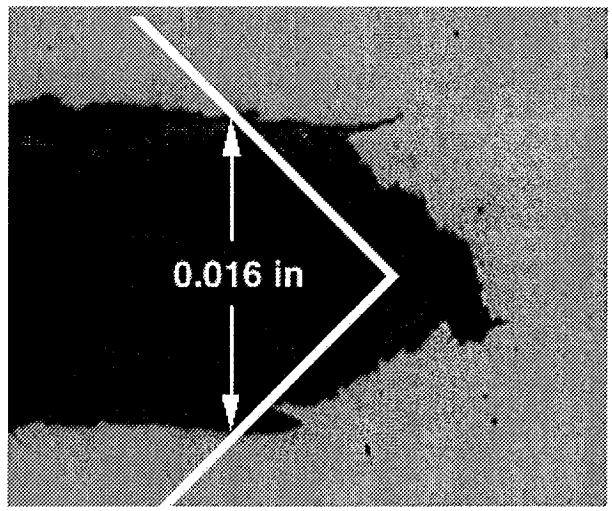

Figure 67: Crack tip opening displacement at initiation, based on 90° included angle method.

measured J-R curves, load-CMOD curves, and crack front sizes and shapes.

Determination of the J integral was performed automatically by Warp3D, based on a user specified *J* integration path. The integration path was carefully chosen such that it remained within the weld region of the model. However, despite this effort, a large amount of divergence occurred between the predicted and experimental J-R curves at high values of *J* (large amounts of growth). It was determined that this was most likely the result of strain interaction problems resulting from the *J* integration path being too close to the line separating the weld and plate materials. To correct for this problem, the J-integral was computed manually, by integrating the area under the Warp3D crack mouth opening displacement curve as detailed in ASTM Standard E813, Section A2.5.

In this method, the J-integral is divided into two components: an elastic component, J_{el}, and a plastic component, J_{pl}:

$$J_T = J_{el} + J_{pl} \tag{40}$$

At any load step (*i*) in the load curve, the elastic *J* component can be computed as:

$$J_{el_i} = \frac{K_i^2(1-\nu^2)}{E} \tag{41}$$

where:

$$K_i = \frac{P_i}{\sqrt{BB_N W}} f(a_0/W) \tag{42}$$

$$f(a_0/W) = \frac{(2 + a_0/W)\begin{pmatrix} 0.866 + 4.64(a_0/W) - 13.32(a_0/W)^2 \\ 14.72(a_0/W)^3 - 5.6(a_0/W)^4 \end{pmatrix}}{(a_0/W)^{3/2}} \tag{43}$$

and J_{pl}, the plastic component can be computed as:

$$J_{pl} = \frac{\eta A_{pl_i}}{B_N b_0} \tag{44}$$

where:

A_{pl}	=	Area under the load vs. crack mouth opening displacement curve (See Figure 68)
B_N	=	Net specimen thickness
b_0	=	Uncracked ligament
η	=	Plastic eta factor (Load-CMOD Integration Coefficient): 2+0.522 b_0/W for C(T) specimens[10]

The Warp3D predicted J-resistance curve shown in Figure 69 is a J-R curve derived from an area analysis of the load versus crack mouth opening displacement curve shown in Figure 70. Adjustments were made to the initial void volume fraction to produce a good fit between the Warp3D prediction and the experimental data.

The predicted crack mouth opening displacement curve diverges from the average of the experimental curves by approximately 11 percent. However, after breaking the test specimens, it was observed that the precrack front was not straight and the crack length at different points along the crack front varied by as

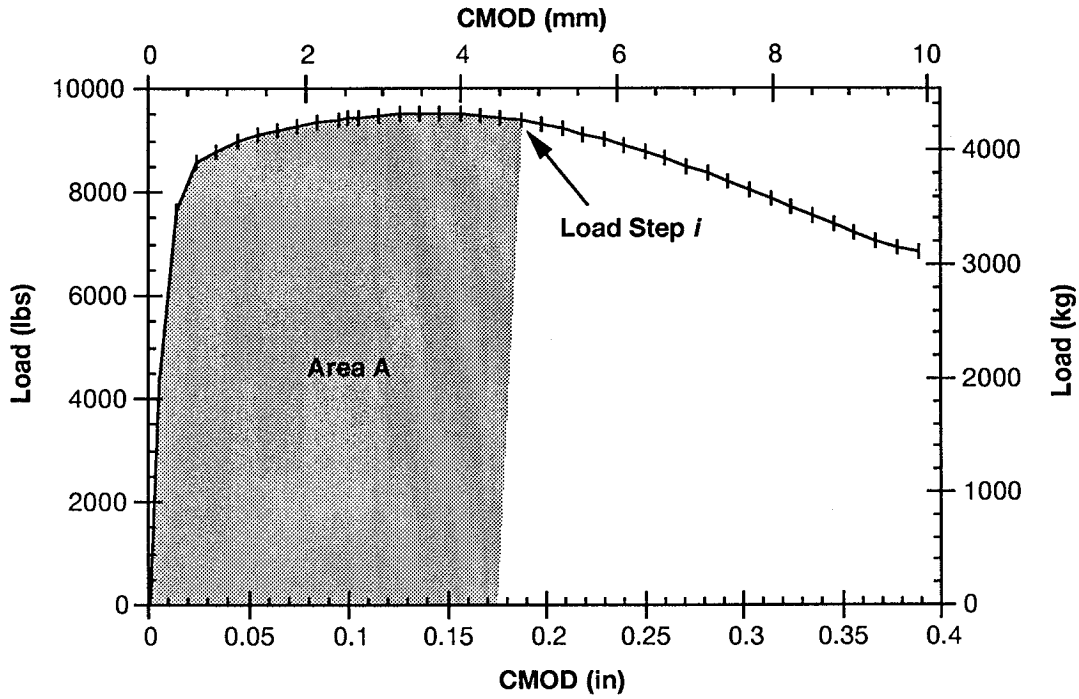

Figure 68: J-Integral area integration method.

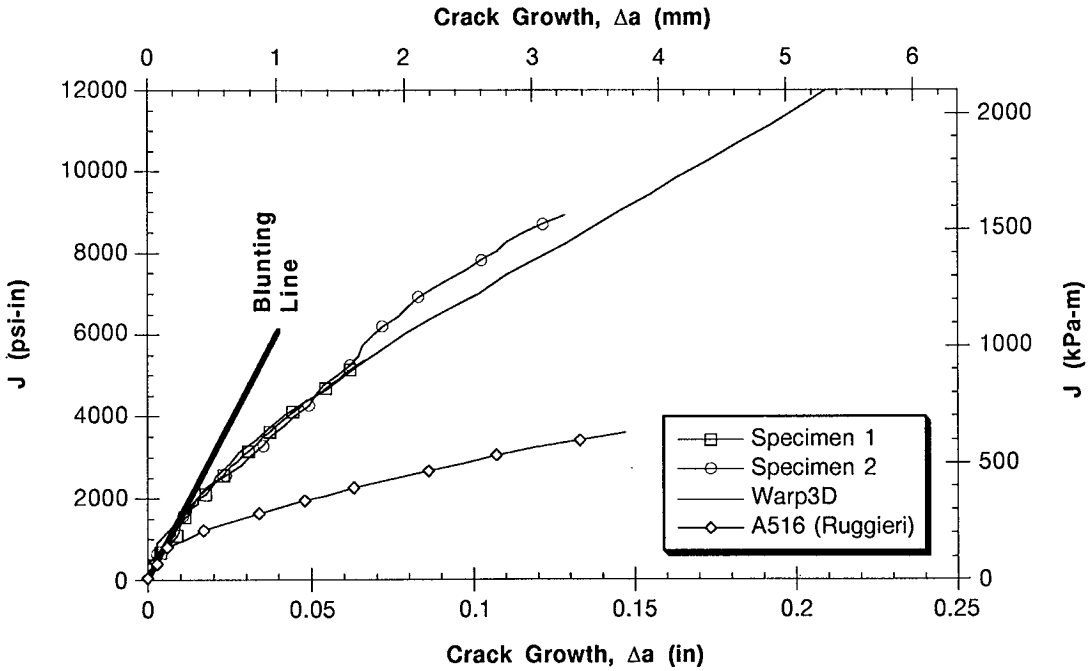

Figure 69: Weld metal J-R curve comparison of analysis and test results. (duplicate tests) J-R curve for A516 Steel (f0=0.002) shown for comparison.[43]

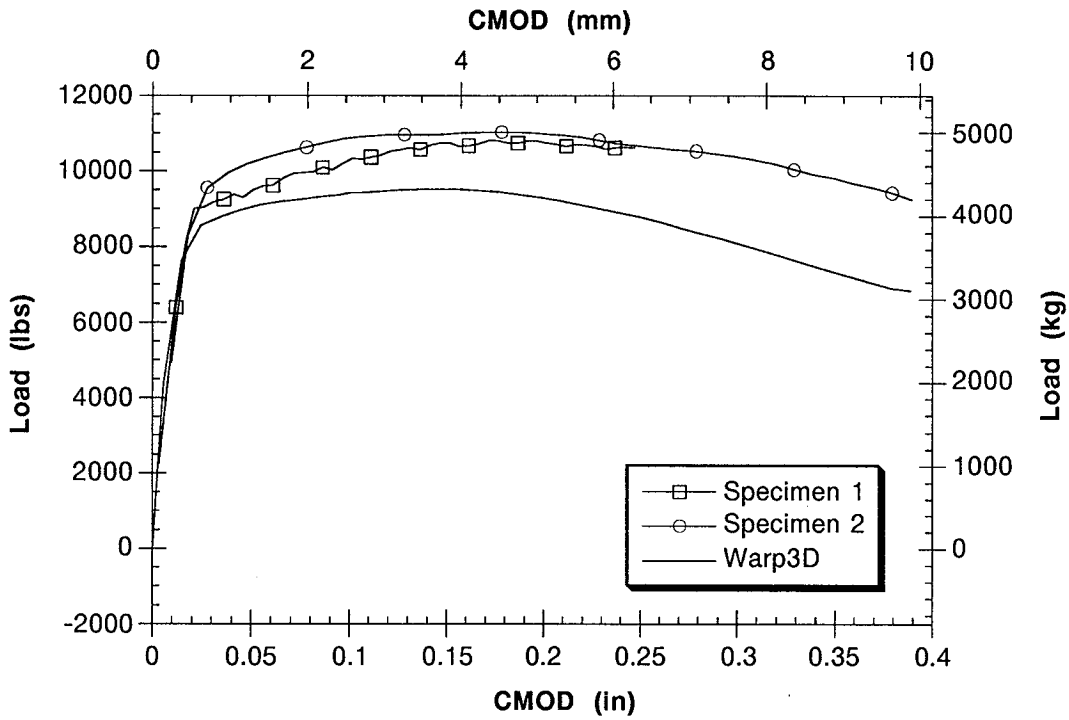

Figure 70: Compact tension crack mouth opening displacement vs. load. (duplicate tests)

much as 40%, despite the fact that the average crack length was only 0.016 inches (0.4 mm) shorter than the desired fatigue precrack extension of 0.07 inches (1.78 mm). Short precrack lengths in local areas could have the effect of elevating the crack mouth opening displacement curve.

A third comparison, crack front shape, was utilized to further examine parameter adjustment. A representation of the crack front shape can be developed from the Warp3D data, based on the elements that have reached the subcritical void volume fraction of 0.1. Although elements still have load carrying capacity at this void volume fraction, their stiffness is gradually reduced, reaching zero at a critical void volume fraction of 0.15. Figure 71 is a plot of the Warp3D computed crack front, overlaid on top of the actual crack front for three different tests. In either case, the crack front was computed at the final J value for the test specimen.

The figure on the top left produces a nearly perfect match, while the figure on the right shows that the finite element analysis predicted a much straighter crack front. This is most likely the result of Warp3D overpredicting the amount of void growth in low constraint areas near the surface of the highly deformed compact tension specimen.

Summarizing, the calibrated crack tip element size, chosen as a compromise between stress-strain accuracy and matching the characteristic length, was 0.004 inches (0.1 mm). Initial void volume fraction, from matching J-R curves, load-CMOD curves, and crack front sizes and shapes was 0.001. Although the element size was chosen smaller than the characteristic length of the weld metal, it is still well within the bounds of being physically reasonable, as is the initial void volume fraction.

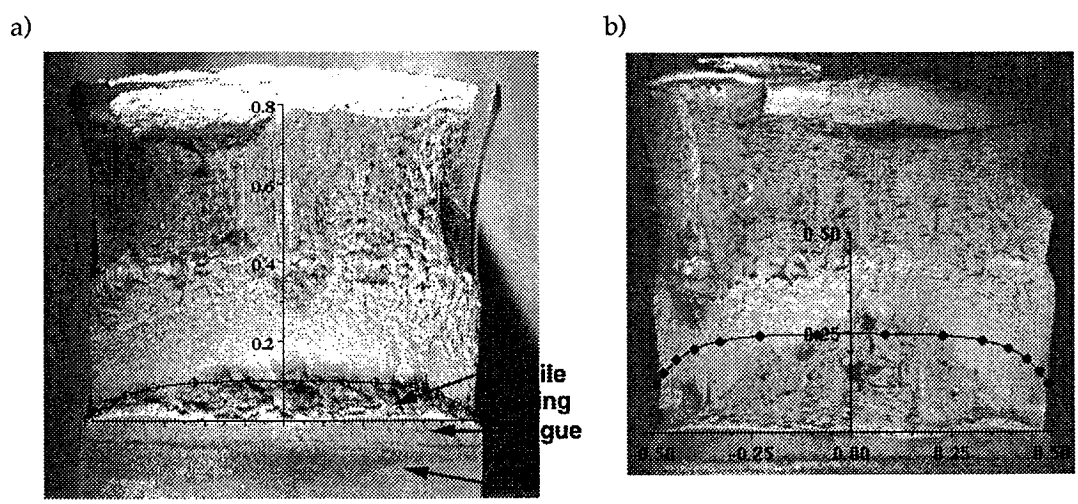

Figure 71: Compact tension predicted crack front superimposed on actual fracture surfaces of three C(T) specimens. Conditions: a) J = 4,645 psi-in. (813.5 KPa-m), b) J = 8,923 psi-in (1,562.7 KPa-m). Dimensions in inches.

Chapter 8

Experimental Results and Verification

Up to this point, finite element modeling parameters have been adjusted to produce good correlation between results from analysis and experimentation. The objective in this chapter is to apply these parameters, without adjustment, to another geometry to determine transferability. This was accomplished using the realistic structural configuration of a tension loaded center cracked panel.

8.1 Analysis

As with the compact tension specimens, the tension loaded center cracked panel specimen shown in Figures 72 and 73 was modeled as a one-eighth model with reflective boundary conditions. In the compact tension specimens, the width of the weld varied through the thickness of the plate. Modeling was accomplished by computing an average weld thickness and applying it uniformly through the thickness of the model. This was done to simplify modeling where a three-dimensional model is built-up from two-dimensional layers, thereby having no variation of geometry in the through-thickness direction. In contrast, the center cracked panel specimens were designed such that the width of the weld varied over the specimen face, and remained constant through the thickness. This is shown in Figure73b. Since the specimen face was modeled in detail, the weld could be accurately represented in the through-thickness direction, when built-up from the two-dimensional model. This is shown in Figure 73a. Ten layers of elements made up the thickness of the center cracked panel specimen, with a 10 to 1 aspect ratio

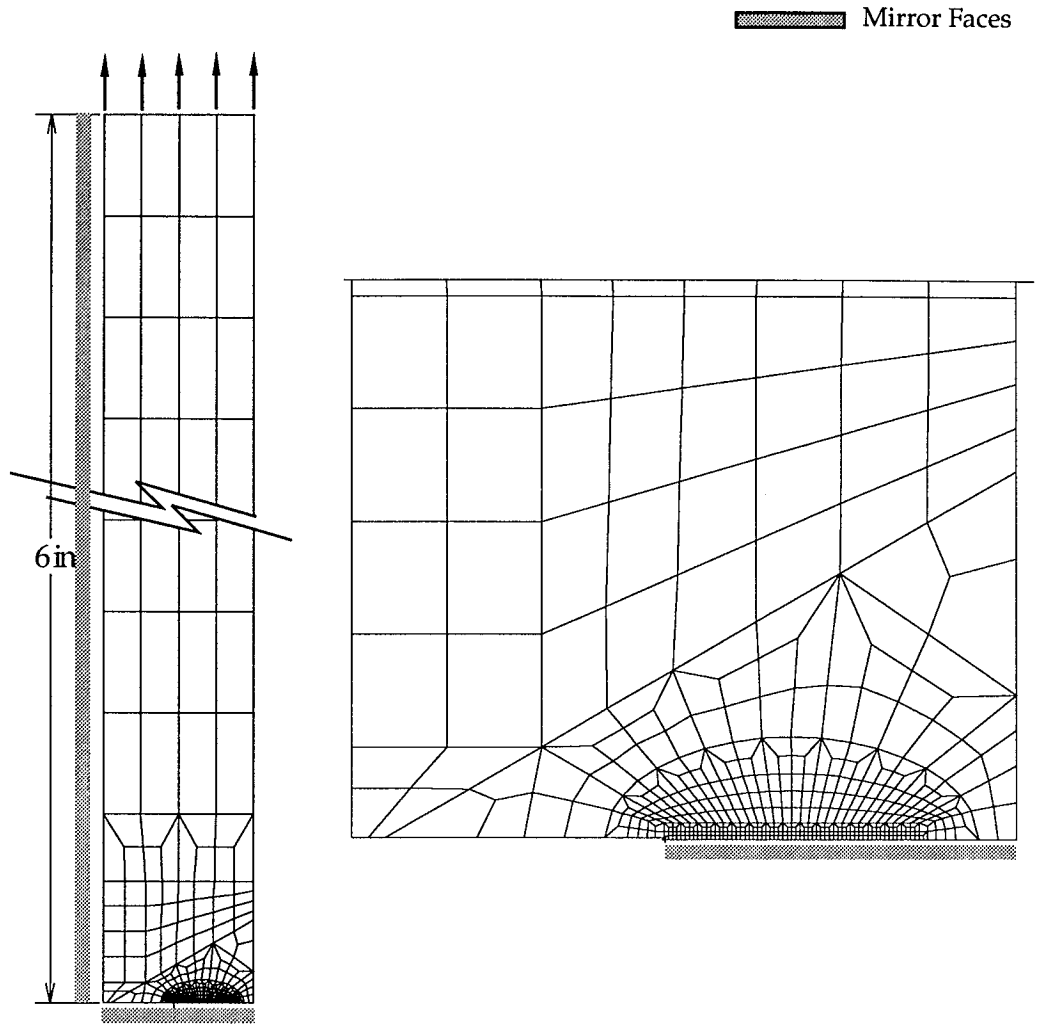

Figure 72: Center cracked panel tension specimen model.

between the thickness of the midplane and outer layers, as shown in Figure 73a.

The center cracked panel crack front was modeled identical to the C(T) model, with an element size of 0.004 inches (0.1 mm). A displacement boundary condition was applied to the end of the model to simulate displacement controlled loading.

The remaining material parameters are included in Table 5, and repeated in Appendix C along with the Warp3D solution parameters utilized.

Accuracy of the analytical solution was determined based on comparisons

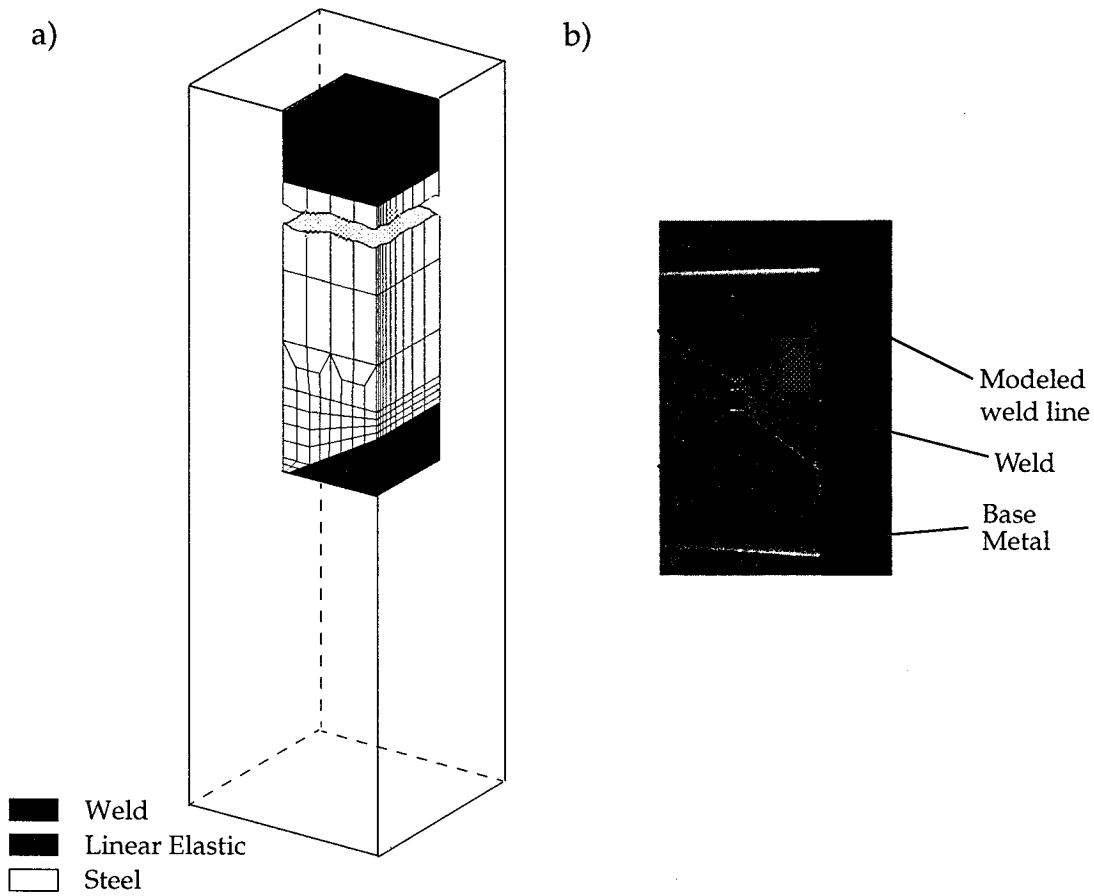

Figure 73: Center Cracked Panel: a) The parent metal, weld, and load application regions were assigned different material properties, as indicated by the shaded regions. b) The actual specimen face-view, etched with 5% Nital to reveal location of the in weld crack plane. Lines indicate modeled fusion line.

of load-CMOD response, surface strain adjacent to the crack tip, and crack front sizes and shapes.

Although there was no way to experimentally measure the J-resistance curve for the center cracked panel, it was manually computed based on the CMOD results of the Warp3D analysis. Automatic calculation of the J-integral thorough the method of domain integration was determined to be inaccurate in the weld specimen, due to the proximity of the fusion line to the integration domain. Instead, it was determined that the CMOD area integration method of ASTM E813

Section A2.5[10] would produce better results and thus this method was applied.

In order to apply the ASTM CMOD area integration method, a geometry and material dependent η factor must first be determined. This factor relates the amount of energy being released due to crack growth, with the amount of energy being applied to the specimen. Although the η factor is material dependent, comparison of η determinations by Kirk[31] suggest that the dependence is small. Therefore, an analysis was run on a center cracked panel consisting of a single material to determine the load - CMOD relationship shown in Figure 74. In this case, since there were two crack tips releasing energy, the load-CMOD relationship was taken as half of the total load. By comparing the automatic domain integrated J results to the manual integration of the CMOD results at each displacement step, the η factor for the center cracked geometry was determined. For center cracked

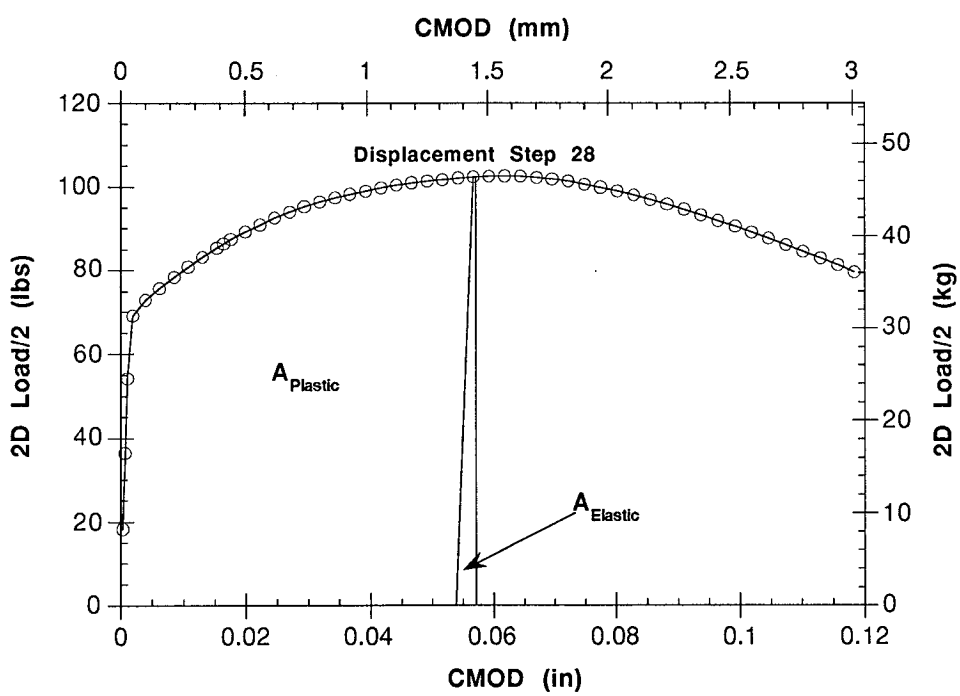

Figure 74: Load - CMOD relationship for single material, tension loaded center cracked panel.

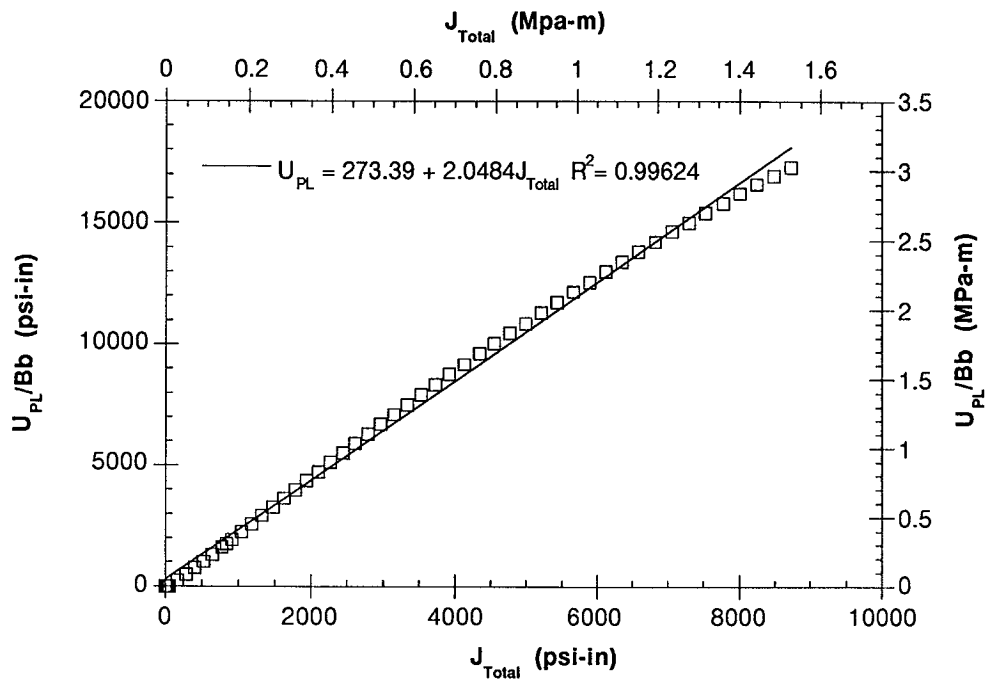

Figure 75: Determination of η factor for single material, tension loaded center cracked panel.

panels with an a/W of 0.5, the η factor was found to be 2.05. This is shown in Figure 75.

Integration of the Warp3D CMOD results shown in Figure 74 resulted in the J-resistance curve shown in Figure 76. The J-curve for the compact tension test is also shown, and shows lower crack resistance, as it should due to its higher level of constraint.[2]

The accuracy of the Warp3D analysis was not based on comparison of J-R curves, since there was no way to experimentally determine the J-R curve in the center cracked panel. Integration of the load-CMOD curve as detailed previously would have allowed the determination of the experimental J-R curve. However, since the same technique would have been applied to both the experimental and analytical results, no difference would have resulted over comparing the load-CMOD response.

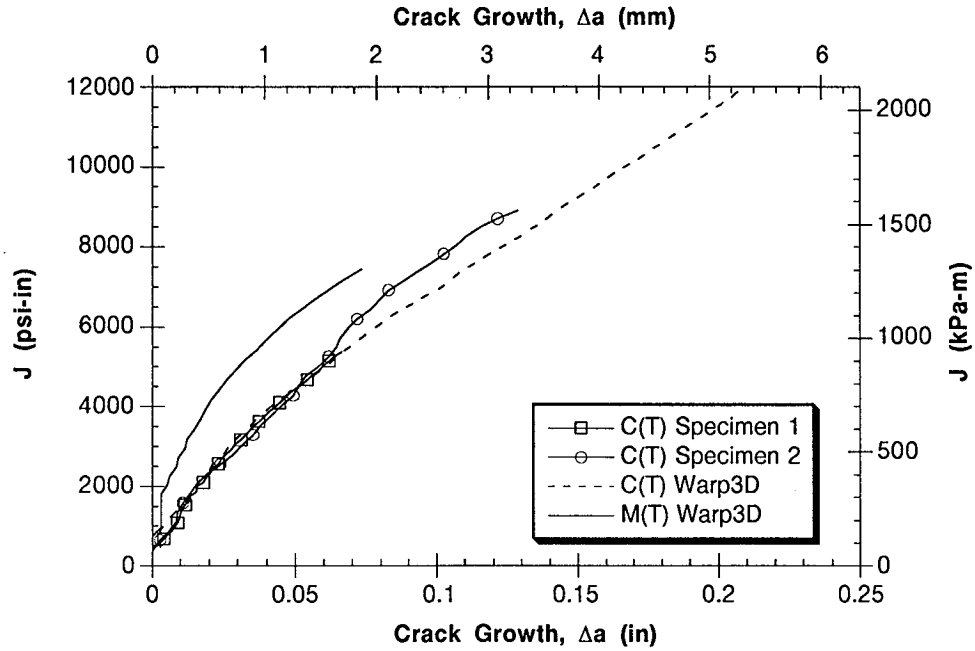

Figure 76: J-Resistance curve for tension loaded center cracked panel and compact tension specimen.

Table 5: Crack growth and weld material parameters for Warp3D model.

Property	Symbol	Value	Units
Young's Modulus	E	30,000,000	psi
Poisson's Ratio	ν	0.30	
Yield Stress	σ_0	69,533	psi
Hardening Modulus	E_T	54,847	psi
Initial Void Fraction	f_0	0.001	
Gurson-Tvergaard Parameter 1	q_1	1.25	
Gurson-Tvergaard Parameter 2	q_2	1.0	
Gurson-Tvergaard Parameter 3	q_3	1.5625	
Nucleation Parameter 1	f_n	0.04	
Nucleation Parameter 2	s_n	0.1	
Nucleation Parameter 3	e_n	0.3	
Stress Strain Curve		Piecewise Linear	
Reference Strain Rate	ε_{ref}	0.000064	in/sec
Cell Size	D	0.004	in

8.2 Results

The crack mouth opening displacement results of the model are shown in Figure 77. Results are within 15% of the results of laboratory testing. Specimen 4, which had an EDM crack tip and did not rely on fatigue precracking, gave results within 7% of the CMOD prediction.

Values of strain in the outer fiber adjacent to the crack tip, closely match strain measurements in strain gaged specimens. This is shown in Figure 78. Warp3D strains were determined by averaging the computed strain over elements associated with the strain gage locations. Each specimen was outfitted with a pair

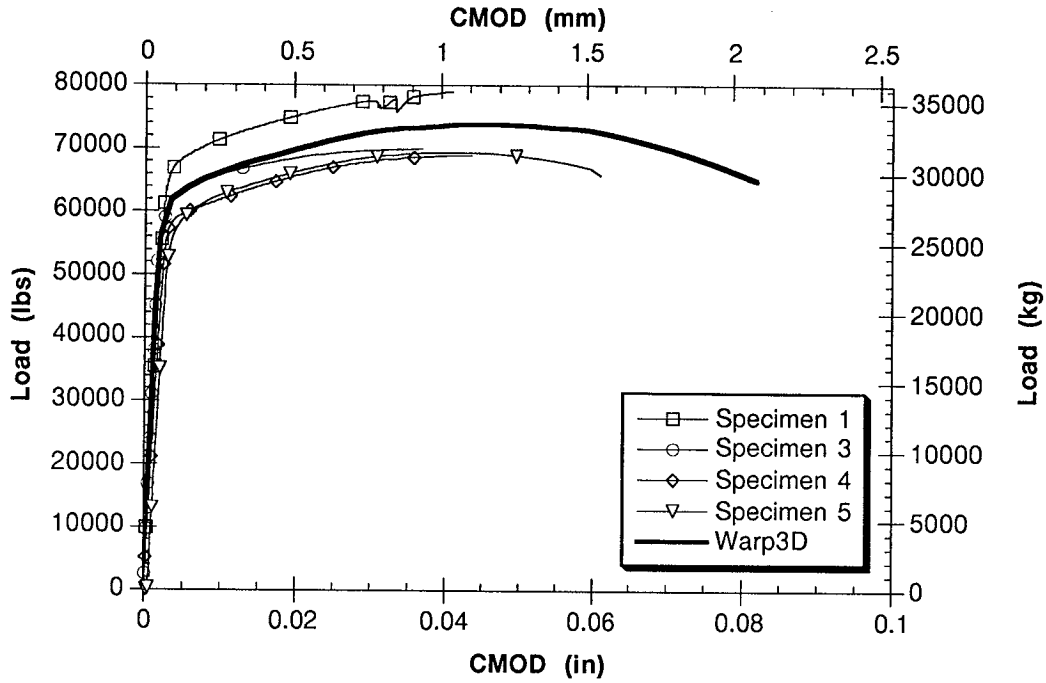

Figure 77: Center cracked panel tension CMOD results comparison. (duplicate tests)

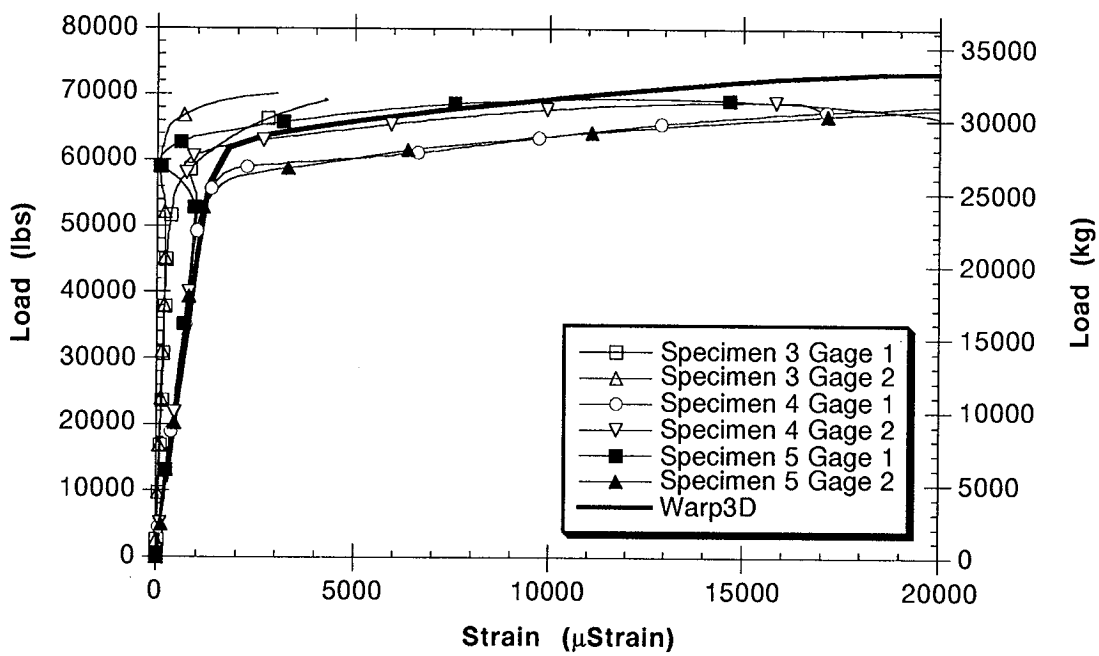

Figure 78: Center cracked panel tension strain results comparison. Warp3D strain extracted from average strain over elements associated with strain gage location. (duplicate tests)

of strain gages, one on each side (See Figure 40). Negative strain readings, such as those measured in Specimen 2, are most likely due to specimen bending, resulting from unevenly grown fatigue precrack fronts. Examination of the failure surface verified that Specimen 2 had four times as much crack growth on one side than the other, which could have resulted in uneven bending of the specimen. This further points out why fatigue precracking was abandoned and EDM crack tip preparation was employed (See Specimen 4 data, Figure 77 through 79).

As with the compact tension specimen, a crack growth profile was again constructed, based on the elements that had reached the subcritical void volume fraction of 0.1, at a given level of crack mouth opening displacement. Figure 79 shows the predicted amount of crack growth, overlaid on three different test specimen fracture surfaces. As shown, crack growth predictions were nearly identical to the amount of crack growth in both cases. The left side of Figure 79 is the fracture surface from Specimen 1 wherein fatigue precracking was used to form the crack tip. Adjustments were made to the predicted crack front to account for the irregularities in the fatigue precrack. This adjustment consisted of simply adding the amount of precracking beyond linearity to the predicted precrack lengths.

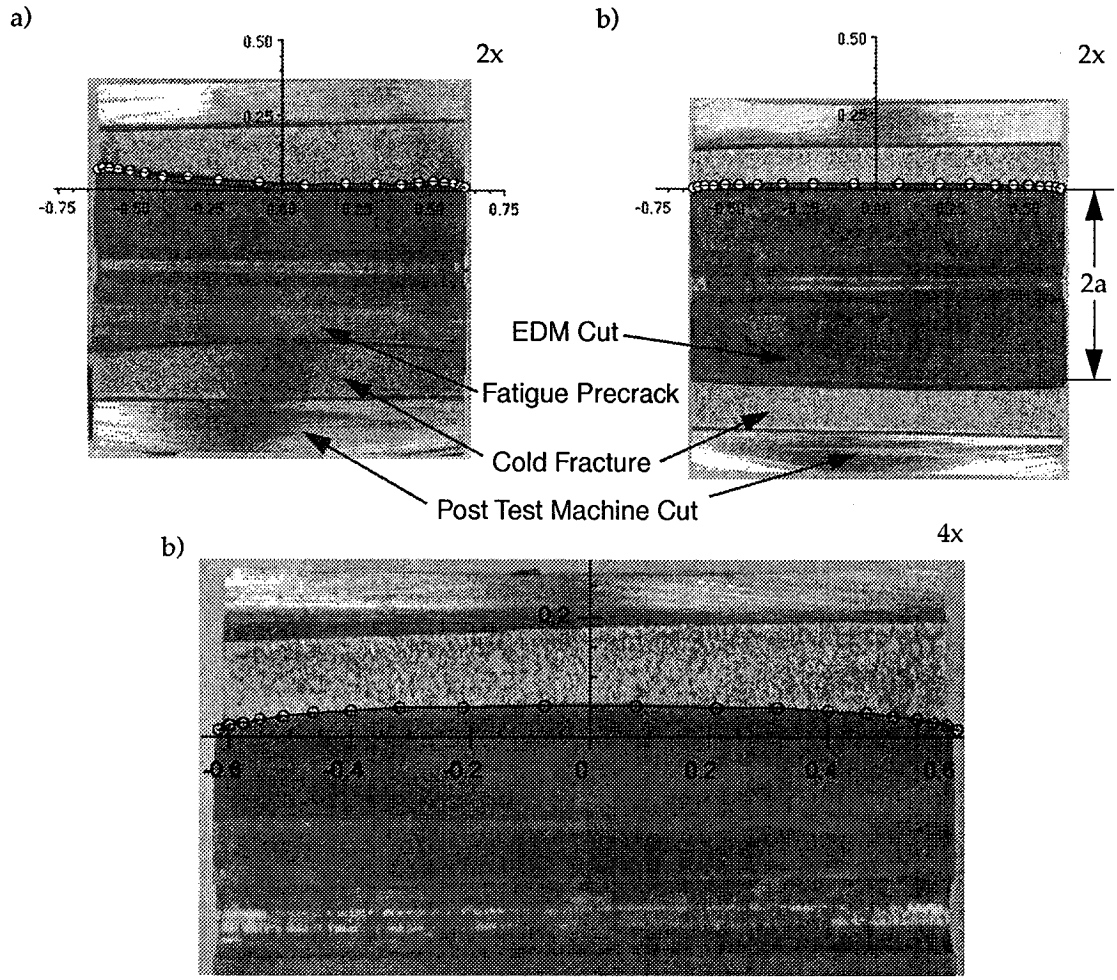

Figure 79: Center cracked panel predicted crack front superimposed on actual fracture surfaces. a) Fatigue cracked front, 0.04 inch (1.01 mm) CMOD, b) EDM notched crack front, 0.045 inch (1.14 mm) CMOD, c) EDM notched crack front, 0.06 inch (1.52 mm) CMOD. Dimensions in inches.

Chapter 9

Summary, Conclusions, and Discussion

The results of these experiments are very encouraging. The ability to model and predict crack growth in flawed welded specimens has been demonstrated. There were many lessons learned in conducting these experiments and some improvements in the methodology will be implemented to reflect this new knowledge.

9.1 Summary

The Warp3D implementation of the Gurson-Tvergaard void growth model was used to accurately predict ductile crack growth in welded fracture specimens and a realistic structural configuration. The structural configuration, a tension-tension loaded center cracked panel, simulating a longitudinal wind tunnel butt weld with a lack of penetration defect, was modeled in Warp3D. Predictions of crack growth, surface strain adjacent to the crack tip, and load-crack mouth opening displacement compared favorably with results from experimental testing.

In preparation of applying the methodology, material properties for the weld metal were determined. This included flow property determinations from tensile tests, material characteristic length determination from the stress modified critical strain failure criterion, and initial void volume fraction from J-R curve matching in compact tension fracture specimens.

The techniques utilized in the determination of material properties were straightforward and simple to apply. However, these techniques were not always

quick, as they required running many finite element models which consumed numerous computational hours.

Predictions of crack growth using Warp3D and the Gurson-Tvergaard void growth model provided very good results at low levels of crack growth, on the order of one-third of the crack front width. As the crack extended past this point, Warp3D failed to predict the amount of tunneling observed in experimental testing. This may be due to the difference in constraint between the midplane and outer surfaces of the model. (Plane strain vs. plane stress conditions.) This became clear as comparisons were made of the J-resistance curve, crack mouth opening displacement, and crack shape and size.

The measured J-resistance curves were nearly identical to those predicted by Warp3D, although the predicted crack mouth opening displacements were slightly depressed at larger values of CMOD. It is likely that this is the result of Warp3D overpredicting the amount of cracking, thereby decreasing the stiffness and load carrying capacity of the model.

9.2 Conclusions

During the course of this research, several important findings were made. These are summarized in the list below:

1. Warp3D performs optimally at crack lengths less than one third of the specimen thickness. This is based on predictions of crack growth on welded compact tension specimens, where Warp3D accurately predicted crack growths of this size.

2. For the geometries investigated, using the Kirk, et al. bimetallic weld assumption[31] (homogeneous properties in heat affected zone) performed acceptably.

3. The Gurson model predicts crack growth best in areas of high constraint. Warp3D accurately predicts crack growth at the center of

specimens, where the constraint is the highest. In lower constraint areas, such as near the surface, the accuracy of Warp3D predictions decreases. This is most likely the result of a decrease in constraint at the outer edges of the specimens, where the accuracy of the Gurson model, and void growth models in general, is limited.

4. The J-integral can be computed numerically in inhomogeneous structures as long as the J integration path does not pass though or contain materials of differing properties.[31] However, analysis shows that if the J integration path is taken too close to the modeled fusion line, that erroneous calculation of the J-integral can occur.

5. In situations where the J-integral must be obtained and the integration path would pass through dissimilar metals or too close to the modeled fusion line, the area integration method of ASTM E813, Section A2.5[10] can be utilized. However, this method requires a value for η, the J-integral energy coefficient, which is geometry dependent. Fortunately, the plastic eta factor, η, is not strongly material dependent[31] and can be used, with caution, to estimate the J-integral in structures consisting of dissimilar materials.

6. The fracture toughness, J_{Ic}, for the weld in a compact tension specimen allowed the crack initiation load in the single edged bend specimen to be accurately predicted, based on finite element computation of the J-integral.

7. The material characteristic length can be determined through the stress modified critical strain method demonstrated by Panontin.[41] Fracture surface microscopy can be used to determine the mean inclusion spacing, and since it is generally 1-2 times less than the characteristic length, can be used to verify or refine the SMCS determined characteristic length. In either case, the characteristic length can be verified by performing analysis of standard fracture specimens.

8. The optimal characteristic length for E7018 welds in A516-70 plate is 0.0075 inches (0.19 mm). This is nearly twice as large as the characteristic length for A516-70 steel.

9. Sizing of crack growth elements to match the characteristic length must be traded off for accuracy of stresses and strains at the crack tip. Sometimes, elements smaller than the characteristic length must be used to provide acceptable crack tip stresses and strains. When this is the case, characteristic length and initial void volume fraction must be balanced in the analysis. Therefore, if elements are sized smaller than the characteristic length, increasing porosity will produce similar results as an analysis performed with elements equal in size to the characteristic length. Similarly, if elements are sized larger than the characteristic

length, decreasing porosity will produce similar results as an analysis performed with elements equal in size to the characteristic length. However, both element size and initial void volume fraction should fall within a range that is physically meaningful.

10. The optimal element size for E7018 welds in A516-70 plate is 0.004 inches (0.1 mm).The optimal initial void volume fraction, based on this element size is 0.001. This is twice as large as the initial void volume fraction for A516-70 steel with the same element size.

9.3 Discussion Critique

9.3.1 Fabrication

Fabrication of the specimens proved to be a challenging effort in performing this research. Many of the specimens were designed to consist partially or completely of weld metal. Variation in the welding technique as well as geometric nonuniformity resulted in some specimens having to be reworked to remove plate metal from the test section. Additionally, the indexing of specimen blanks was critical and very difficult, since the weld had to line up with the intended crack plane. Problems in fabrication resulted in the reworking of the round-bar tensile and single edged bend specimens.

Problems arose in two of the compact tension tests wherein the crack tip may have entered the fusion zone at the center of the weld. This would have the effect of producing abnormally low results for crack growth resistance and crack mouth opening displacement.

In the future, fabrication guidelines should call for gouging out more material at the weld root during welding, thereby providing more weld metal at the weld center.

9.3.2 Experimentation

Precracking of the SE(B) specimens took longer and required more attention

because there was no way to automatically monitor the specimen crack length. A better approach, and one to be used in the future, would be to machine flat faced integral knife edges into the specimen, and attach a clip gage, thereby allowing in situ crack length measurements through the compliance method of Wu.[55] Since crack length could be constantly monitored, specimen precracking could also be performed at a constant ΔK.

Experimentation on the single edged bend specimens provided important information with respect to the weld material characteristic length. However, the objective was to load the specimen to the point of crack initiation, when the load or CMOD required to accomplish this was not precisely known. Initiation load was determined prior to testing, based on analysis of the J-resistance curve, a method which proved to be fairly accurate and straightforward. Once the specimen was tested, sectioned, and photographed, it was determined that the crack had initiated, but had not grown excessively. It was fortunate that the estimated initiation load was nearly exact, when considering the cost of multiple specimens and the high probability of missing initiation and getting too much crack growth or none at all.

Testing of the compact tension specimens provided satisfactory results. However, the crack fronts were not as straight as might have been achieved, had the crack fronts been chevroned per ASTM Standard E399 Section 7.3.1.[7] Regardless, the average crack length at the end of fatigue precracking was correct, suggesting that the compliance method of measuring crack length did work properly.

There were a couple lessons learned in the process of testing the center cracked panels. For the specimen cross section utilized, the clevis ends were barely adequate to handle the load and deformed slightly during the process of testing.

A smaller cross section, or larger specimen end is required to prevent this from happening in the future.

Initially, the center cracked panel crack tips were undercut, with the intention that fatigue precracks would be grown so that a crack aspect ratio of 0.5 was attained. Several different methods were utilized to try to grow straight, even cracks. Longitudinal bending in both the long and short transverse directions were tried. However, none of these methods produced satisfactory results. Bending in the short transverse direction yielded a higher stress intensity on the outer surface of the specimen rather than at the crack tip. In the long transverse direction, bending grew asymmetrical cracks at the outer edges of the two crack starter-notches. Finally, tension precracking could not be performed at acceptably high stress intensity levels when it was discovered that the load necessary produced stresses in excess of the endurance limit in the clevis pin holes. After attempting and failing to grow satisfactory cracks in three specimens, the decision was made to EDM cut the crack tips to an a/W of 0.5. This provided much better correlation of the data with predictions, and significantly reduced the specimen preparation time.

9.3.3 Finite Element Modeling

Although P3/PATRAN was used for all finite element model development, it may not be the best tool available, especially when considering the mesh refinement required along the crack front. Element transition routines utilized by P3/PATRAN are unsuitable for meshing crack geometry and produced non-uniform, often bizarre transitions. Instead alternate manual techniques were utilized for simplistic 4-2 transitions which were much better suited for crack analysis.

The complexity of the modeling and analysis of the tensile round-bar specimens was increased by the lack of an axisymmetric element in Warp3D. This feature has recently been added through the use of rotational boundary conditions, although this method still lacks the elegance of a truly axisymmetric model. Instead, a quarter model of the tensile specimen was utilized, and although it produced equally good results, the increased size of the model ballooned computational time by 50 times, increasing the run time on the Dec AlphaStation 250 from 6,000 seconds (1 hour, 40 mins.) to 315,000 seconds (3 days, 15 hours, 30 mins.).

The notched tensile round-bar model was used to determine the weld triaxiality failure criterion. However, the experimental data used in this process would not fit an exponential curve as proposed by MacKenzie.[34] This was inconsequential in the region of interest, although it is important to note that the linear curve fit is inappropriate at large values of triaxiality ($T > 3.5$). In this region, the linear curve predicts a negative equivalent plastic strain. The actual criterion should be asymptotic to the plot axes, a condition much better suited to an exponential curve.

9.4 Further Study

Further research is necessary to improve upon the results and ideas realized though these experiments. This research must include, but is not limited to, investigation into the effect that other void growth model parameters may have on crack growth prediction. In addition, prediction of crack growth from weld defects such as large glassy inclusions and other weld discontinuities is necessary. Finally, analysis of other weld geometries, heat affected zone effects, and the effect of residual stress would be essential to extend the approach developed herein.

The initial scope of this investigation included the modeling of tension and tension plus bending in welded bars. This is representative of welds in wind tunnels, which under pressurization loadings, are subjected to tension (longitudinal butt welds) and tension plus bending (circumferential butt welds near ring supports). The analysis of tension plus bending welds is left to future study. Specimens were designed as part of this research effort, and this information is included in Appendix B.

Reference List

1. Aihara, Shuji. "Influence of Mechanical Heterogeneity on Brittle Fracture Initiation Characteristic." Nippon Steel Technical Report n50 (1991): 30-36.

2. Anderson, T.L. Fracture Mechanics Fundamentals and Applications. Boca Raton: CRC Press, 1995.

3. ASME Boiler and Pressure Vessel Code. Section II: Material Specifications Part C – Welding Rods, Electrodes, and Filler. New York: American Society of Mechanical Engineers, 1986.

4. ASTM Standard E3. Standard Methods of Preparation of Metallographic Specimens. Philadelphia: American Society for Testing and Materials, 1991.

5. ASTM Standard E8. Standard Test Methods of Tension Testing of Metallic Materials. Philadelphia: American Society for Testing and Materials, 1989.

6. ASTM Standard E112. Standard Test Methods for Determining Grain Size. Philadelphia: American Society for Testing and Materials, 1991.

7. ASTM Standard E399. Standard Test Methods for Plane-Strain Fracture Toughness of Metallic Materials. Philadelphia: American Society for Testing and Materials, 1989.

8. ASTM Standard A516/A516M-86. Standard Specification for Pressure Vessel Plates, Carbon Steel, for Moderate- and Lower-Temperature Service. Philadelphia: American Society for Testing and Materials, 1991.

9. ASTM Standard E616-89. Standard Terminology Relating to Fracture Testing. Philadelphia: American Society for Testing and Materials, 1991.

10. ASTM Standard E813. Test Method for J_{Ic}, A Measure of Fracture Toughness. Philadelphia: American Society for Testing and Materials, 1989.

11. ASTM Standard E1290. Standard Test Method for Crack-Tip Opening Displacement (CTOD) Fracture Toughness Measurement. Philadelphia: American Society for Testing and Materials, 1989.

12. Barsom, John M. and Stanley T. Rolfe. Fracture and Fatigue Control in Structures. Englewood Cliffs: Prentice-Hall, Inc., 1987.

13. Berge, Stig, Oddvar I. Eide, and Masahiko Fujikubo. "Level-3 Crack-Tip Opening Displacement (CTOD) Assessment of Welded Wide Plates in Bending—Effect of Overmatching Weld Metal." Fracture Mechanics: Twenty-Third Symposium, ASTM STP 1189. Philadelphia: American Society for Testing and Materials, 1993, pp. 284-309.

14. Broek, David. Elementary Engineering Fracture Mechanics. Dorfrecht: Martinus Nijhoff Publishers, 1986.

15. Dodds, Robert H., Jr. Constraint Effects in Ductile Fracture. Presented at ASME International Mechanical Engineering Congress and Exposition, 1995.

16. Dodds, Robert H., Jr., Warp3D User Notes, unpublished, University of Illinois, 1995.

17. Dodds, Robert H., Jr., William C. Carpenter, and William A. Sorem. "Numerical Evaluation of a 3-D J-Integral and Comparison with Experimental Results for a 3-Point Bend Specimen." Engineering Fracture Mechanics v29 (1988): 275-285.

18. Ewalds, H.L. and R.J.H. Wanhill. Fracture Mechanics. London: Hodder & Stoughton, 1991.

19. Faucher, Bernard, and William R. Tyson. "Comparison of Toughness in Bending and in Tension of a Pipeline Steel." International Journal of Pressure Vessels and Piping v60 n1 (1994): 49-57.

20. Fu, B. "Elastic-Plastic Fracture Mechanics Analysis of Weld-Toe Surface Cracks in Fillet Welded T-Butt Joint." Proceedings of the 13th International Conference on Offshore Mechanics and Arctic Engineering v3 New York: American Society of Mechanical Engineers, 1994, pp. 257-266.

21. Fu, B. "Weld Magnification Factors for Semi-Elliptical Surface Cracks in Fillet Welded T-Butt Joint Models." International Journal of Fracture v63 n2 (1993): 155-171.

22. Gao, X., J. Faleskog, C. F. Shih, and R. H. Dodds. "Ductile Tearing in Part-Through Cracks: Experiments and Cell-Model Predictions." Unpublished.

23. Garrison, W.M., Jr., and N.R. Moody. "Ductile Fracture" Journal of Physics and Chemistry of Solids v48 n11 (1987): 1035-1074.

24. Giovanova, Jacques, and Steven W. Kirkpatrik. "Methodology for Evaluating Strength and Fracture Resistance of Weldments Using a Local Approach to Fracture." Pressure Vessel Integrity v250 New York: American Society of Mechanical Engineers, 1993, pp 157-171.

25. Gurson, A.L. "Continuum Theory of Ductile Rupture by Void Nucleation and Growth: Part I — Yield Criteria and Flow Rules for Porous Ductile Media." Journal of Engineering Materials and Technology v99 (1977): 2-15.

26. Hampton, Roy W. "Record of Industry Consultations in 1993 Regarding Possible Pressure Test of Unitary WT Shell" Internal Documentation, NASA-Ames Research Center, 1995.

27. Hicks, J.G. Welded Joint Design. New York: John Wiley & Sons, 1979.

28. Hutchinson, John W. A Course on Nonlinear Fracture Mechanics. Denmark: The Technical University of Denmark, 1979.

29. Jun, Sun, Deng Zengjie, and Tu Mingjing. "Plane Stress Elastic-Plastic Fracture Criteria and Constraint Intensity in Crack Tip Regions" Engineering Fracture Mechanics v37 (1990): 675-680.

30. Kirk, Mark T. and Robert H. Dodds, Jr. "The Influence of Weld Strength Mismatch on Crack-Tip Constraint in Single Edge Notch Bend Specimens." International Journal of Fracture v63 (1993): 297-316.

31. Kirk, Mark T., Robert H. Dodds, Jr., Ted L. Anderson, and Melinda T. Neligon. "Predictions of Constraint Effects on Elastic-Plastic Fracture in Welded Structures." Interim Report, Texas A&M University, 1992.

32. Koppenhoefer, Kyle C., Arne S. Gullerud, Caludio Ruggieri, and Robert H. Dodds. Warp3D - Dynamic Nonlinear Analysis of Solids Using A Preconditioned Conjugate Gradient Software Architecture" Department of Civil Engineering, University of Illinois, 1994.

33. Linnert, George E. Welding Metallurgy: Carbon and Alloy Steels. New York: American Welding Society, 1967.

34. MacKenzie, A. C., J. W. Hancock, and D. K. Brown. "On The Influence of State of Stress on Ductile Failure Initiation in High Strength Steels." Engineering Fracture Mechanics v9 (1977): 167-188.

35. Martin, Harold C. and Graham F. Carey. Introduction to Finite Element Analysis. New York: McGraw-Hill Book Company, 1973.

36. Matvienko, Yu. G. and E.M. Morozov. "Some Problems in Linear and Non-Linear Fracture Mechanics." Engineering Fracture Mechanics v28 (1987): 127-138.

37. Meyers, Marc André and Krishan Kumar Chawla. Mechanical Metallurgy: Principles and Applications. Englewood Cliffs: Prentice-Hall, Inc., 1984.

38. Moody, N.R., R. E. Stoltz, and M. W. Perra. "The Effect of Hydrogen on Fracture Toughness of the Fe-Ni_Co Superalloy IN903." Metallurgical Transactions A v18A (1987): 1469-1482.

39. Neilgon, Melinda T., Ted L. Anderson, and Robert H. Dodds. "Fracture Behavior of Shallow Cracks in Welded Structures." Fracture Mechanics: Applications and New Materials v260 (1993): 203-208.

40. Nevalainen, Markku and Robert H. Dodds, Jr. "Numerical Investigations of 3-D Constraint Effects on Brittle Fracture in SE(B) and C(T) Specimens." Ohio: Technical Research Centre of Finland, 1995. Photocopied.

41. Panontin, Tina L. "The Relationship Between Constraint and Ductile Fracture Initiation as Defined by Micromechanical Analyses." PH.D. diss., Stanford University, 1994.

42. Raghavendran, N.S. and M.E. Fourney. "Stress Analysis of a Welded Joint." Engineering Fracture Mechanics v48 n5 (1994): 619-627.

43. Ruggieri, Claudio, Tina L. Panontin, and Robert H. Dodds, Jr. "Numerical Modeling of Ductile Crack Growth in 3-D Using Computational Cell Elements." Illinois: University of Illinois at Urbana-Champaign, 1996. Photocopied.

44. Saarenheimo, A., H. Talja, R. Rintamaa, and others. "Verification of the Non-Linear Fracture Analysis by a Large-Scale Pressure Vessel Test." Fracture Mechanics Verification by Large-Scale Testing Edmunds: MEP, 203-221.

45. Schmitt, Winfried, and Johann G. Blauel. "Application of Micromechanical Material Models for the Evaluation of the Fracture Toughness of Primary Circuit Steel Components." Proceedings of the Symposium on Small Specimen Test Techniques Applied to Nuclear Reactor Vessel Thermal Annealing and Plant Life Extension, ASTM STP 1204. Philadelphia: American Society for Testing and Materials, 1993, pp. 106-117.

46. Schwalbe, Karl-Heinz. "On The Influence of Microstructure on Crack Propagation Mechanisms and Fracture Toughness of Metallic Materials." Engineering Fracture Mechanics v9 (1977): 795-832.

47. Schwalbe, Karl-Heinz. "Welded Joints with Non-Matching Weld Metal-Crack Driving Force Consideration on the Basis of the Engineering Treatment Model (ETM)." International Journal of Fracture v62 n1 (1993): 1-24.

48. Sih, G.C. "Some Basic Problems in Fracture Mechanics and New Concepts." Engineering Fracture Mechanics v5 (1973): 365-377.

49. Smith, E. "Effect of Residual Stresses on the Onset of Crack Extension in an Engineering Component." International Journal of Pressure Vessels and Piping v49 n3 (1992): 309-315.

50. Sorem, W.A., R.H. Dodds, Jr., and S.T. Rolfe. "A Comparison of the J-Integral and CTOD Parameters for Short Crack Specimen Testing." Welding Research Council Bulletin v351 (February 1990): 24-34.

51. Sorem, W.A., R.H. Dodds, Jr., and S.T. Rolfe. "An Analytical Comparison of Short Crack and Deep Crack CTOD Fracture Specimens of an A36 Steel." Welding Research Council Bulletin v351 (February 1990): 1-11.

52. Sorem, W.A., S.T. Rolfe, and R.H. Dodds, Jr. "The Effects of Crack Depth on Elastic-Plastic CTOD Fracture Toughness." Welding Research Council Bulletin v351 (February 1990): 12-23.

53. Sunwoo, A. J., and J. W. Morris Jr. "Influence of Intrinsic and Extrinsic Factors on Mechanical Properties of 2090 Aluminum Alloy Weldments." Materials Science and Technology, v7 n10 (1991): 965-971.

54. Tvergaard, Viggo. "Material Failure by Void Growth to Coalescence." Advances in Applied Mechanics v27 San Diego: Academic Press, Inc., 1990, pp 83-151.

55. Wu, S. X. "Crack Length Calculation Formula for Three-Point Bend Specimens." International Journal of Fracture, Vol 24, 1984, pp. R33-R35

56. Zhang, Y.H. and L.J. Wang. "Statistical Analysis of the Surface Fatigue Crack Growth in Welded Joints." Engineering Fracture Mechanics v46 n6 (1993): 1031-1035.

57. Zhang, Y.H., Y.W. Shi, and M.J. Tu. "Studies on the Fracture Mechanics Parameters of Weldment with Mechanical Heterogeneity." Engineering Fracture Mechanics v34 n5/6 (1989): 1041-1050.

Appendix A

Test Specimen Design

Tensile Round Bar Specimen

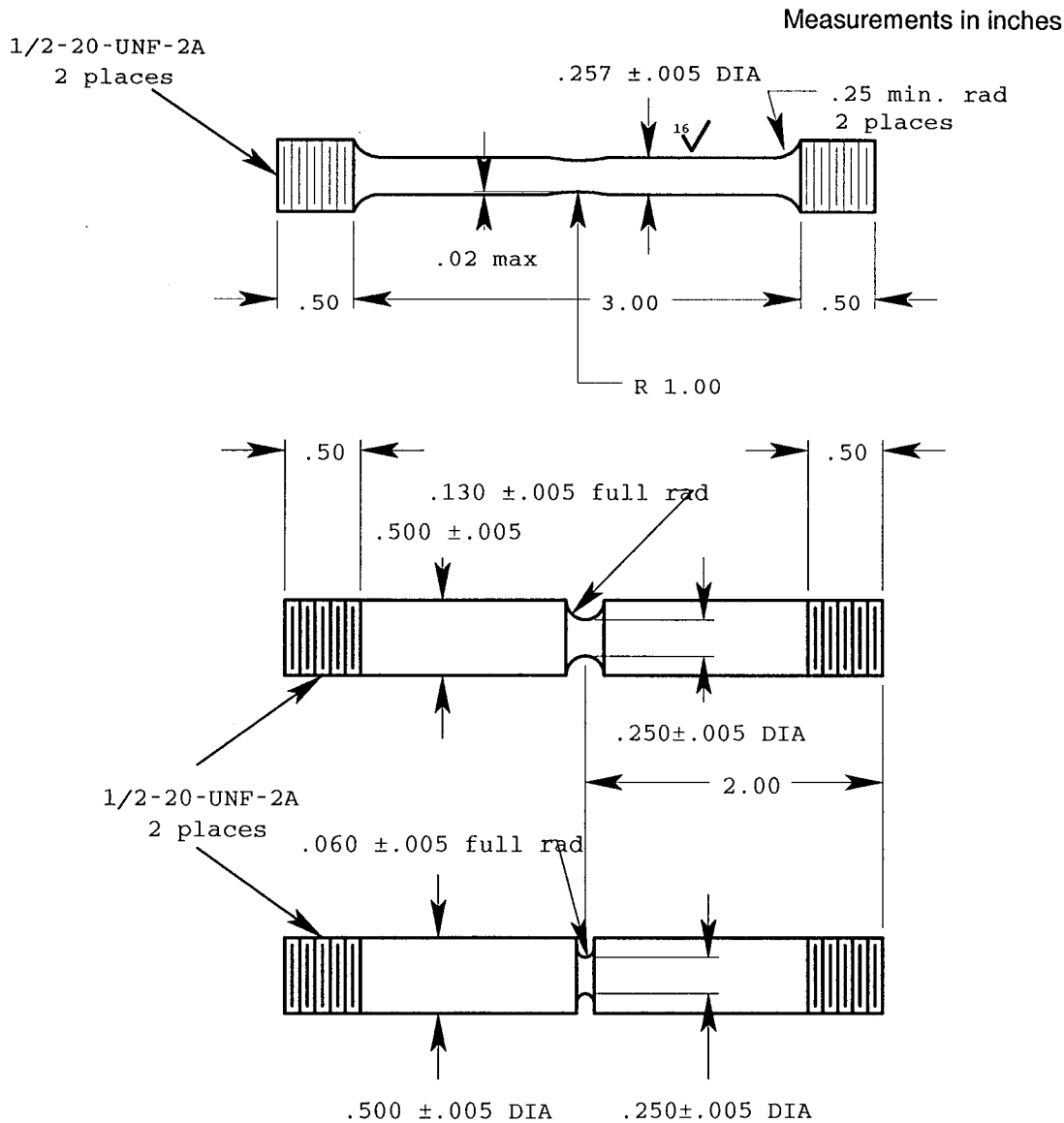

Figure A-1: Tensile Round Bar Specimen.

Single Edged Bend Specimens - Deep Notch

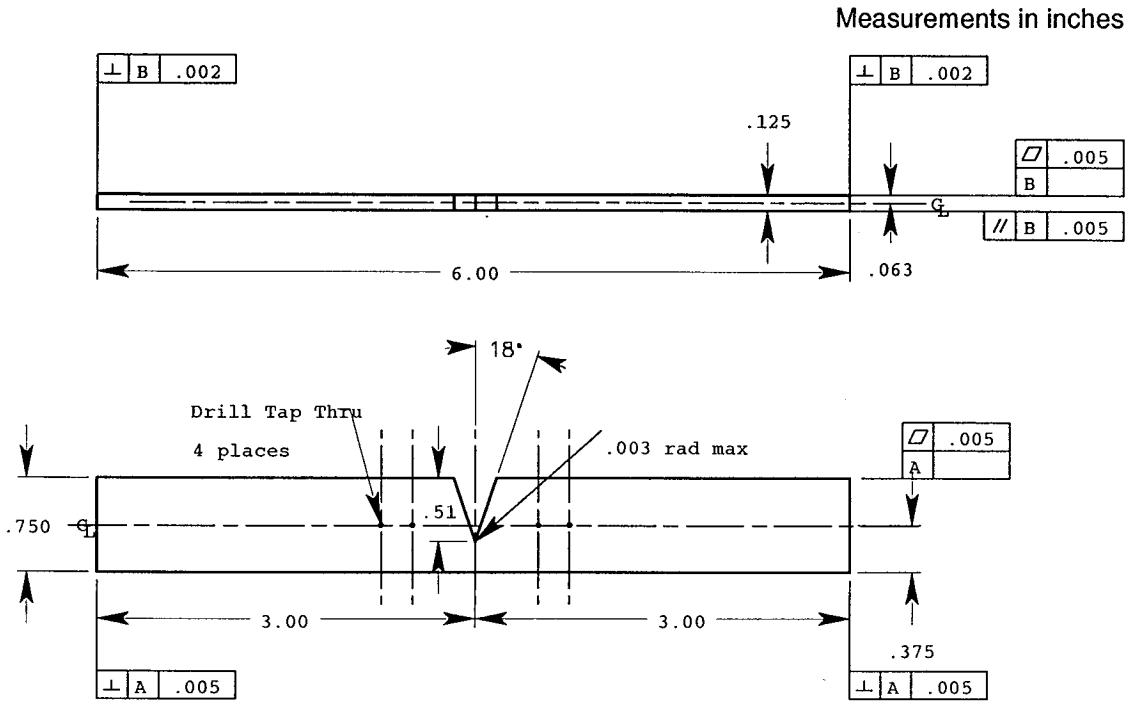

Figure A-2: Single edged bend specimen - deep notch.

Single Edged Bend Specimens - Shallow Notch

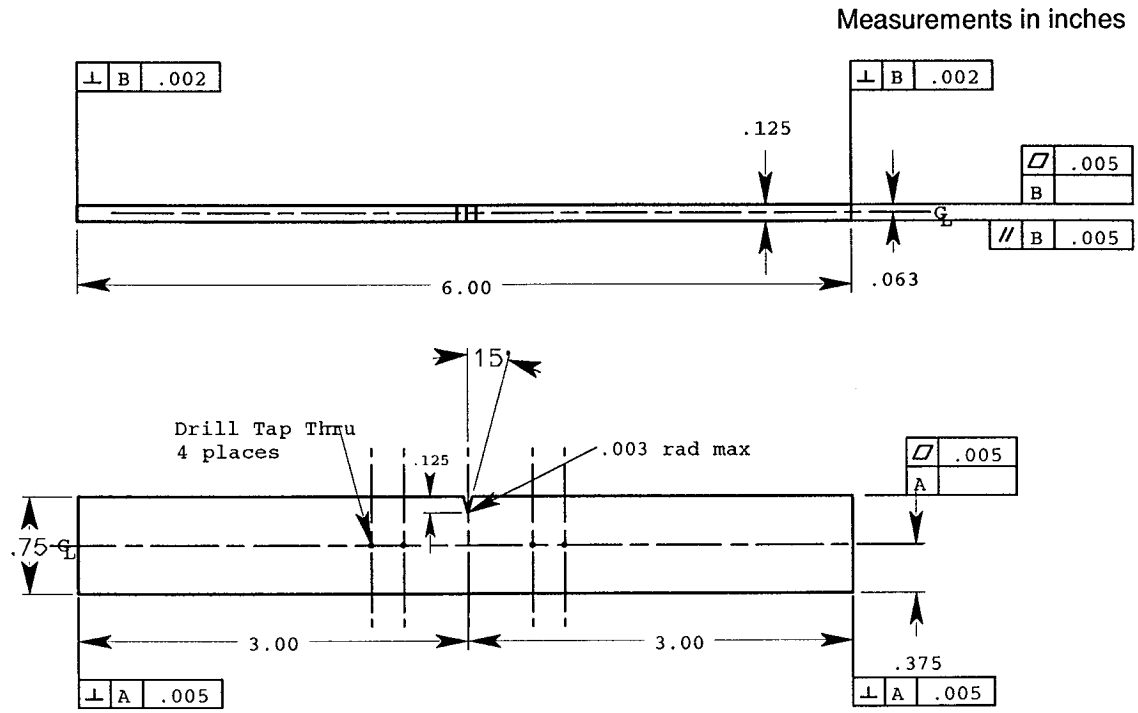

Figure A-3: Single edged bend specimen - shallow notch.

Compact Tension C(T) Specimen

Measurements in inches

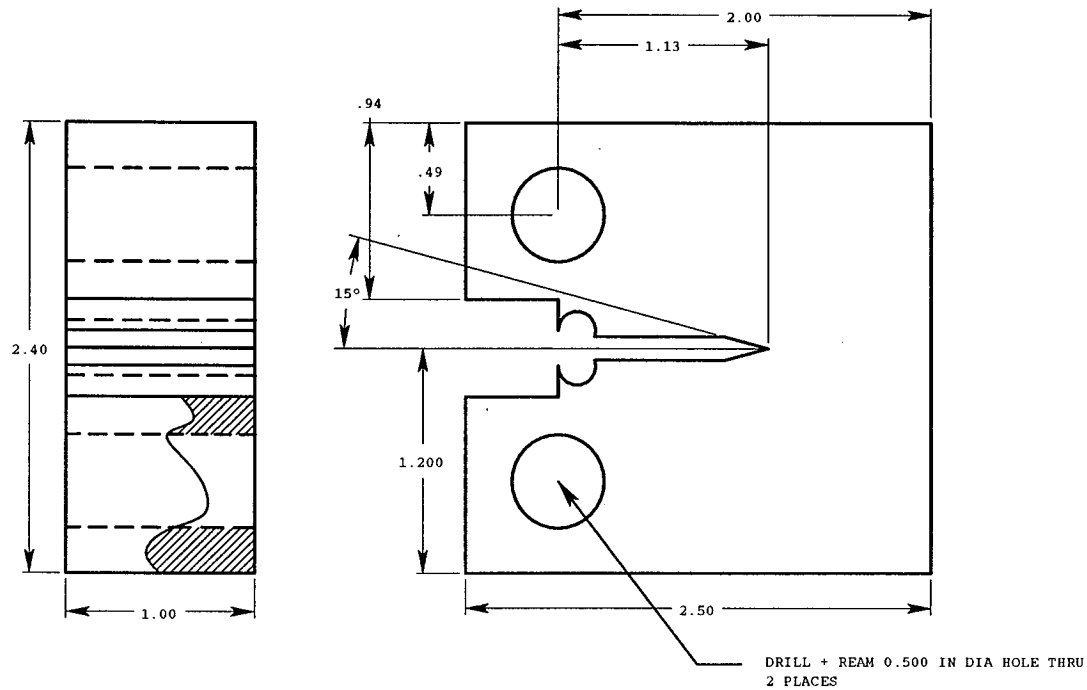

Figure A-4: Compact tension specimen.

Center Cracked Panel M(T) Specimen - Tension

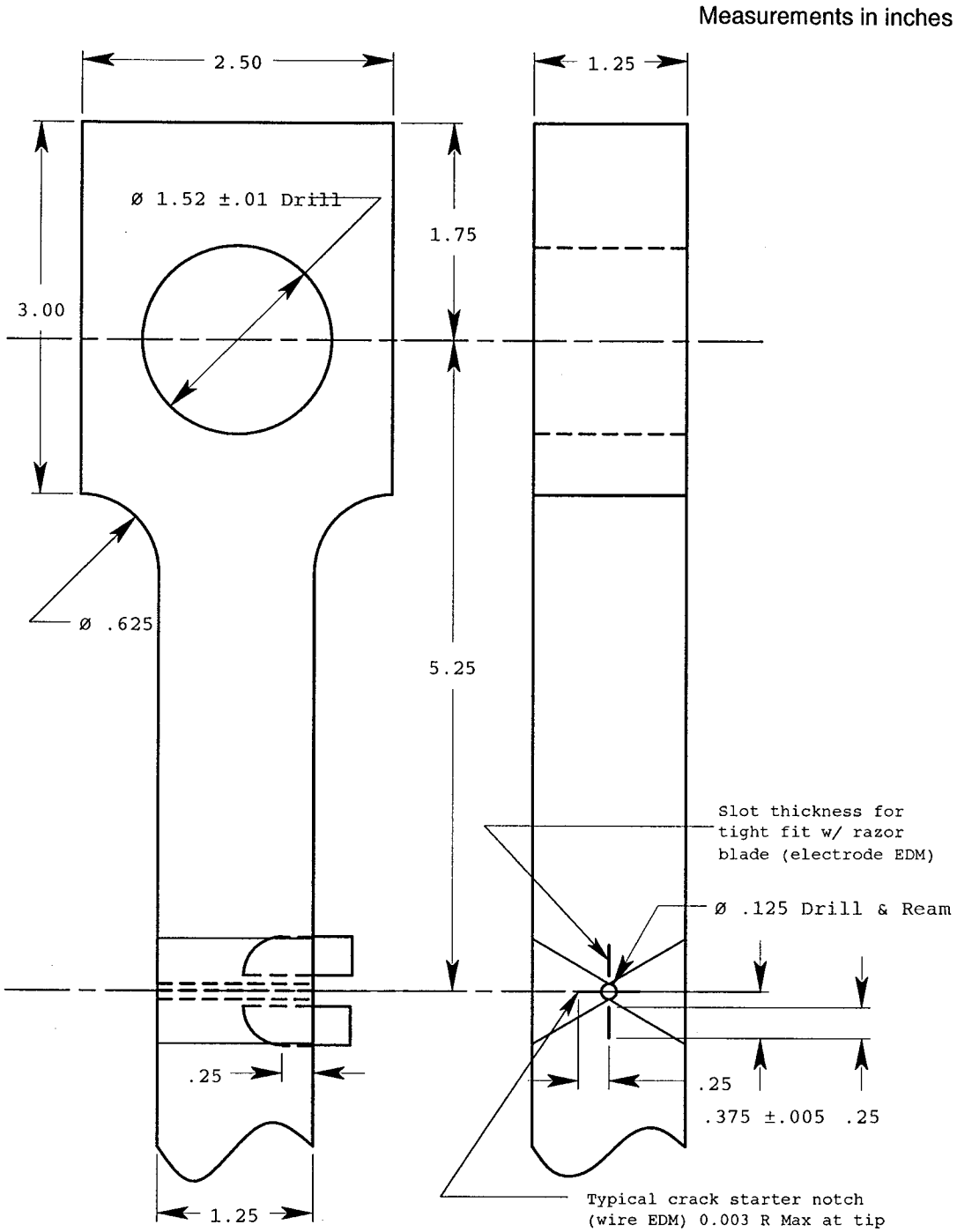

Figure A-5: Center cracked panel tension specimen.

Appendix B

Tension Plus Bending Specimen Design

Center Cracked Panel M(T) Specimen - Tension plus Bending

The tension plus bending specimen is different from the tension specimen in that the bending moment was incorporated into the model by curving the test specimen. This was done to accommodate the test, which would not allow the load point to be offset the required distance using the tension specimen design. Unlike the tension M(T) model, the tension plus bending model is a quarter model. This is due to the lack of geometric symmetry across the width of the specimen. This is shown in the finite element model of Figure B-1. The full specimen is shown in Figure B-2.

The problem with studying bending in this configuration is that bending introduces the problem of element contact at the crack faces on the compression half of the model.† Unlike the situation in the laboratory, finite element analysis is not concerned with material overlap - that is, two pieces of material occupying the same space.

†.This is similar to crack closure. However, without the use of contact elements, the crack face can actually move beyond the mirror plane, effectively resulting in two elements occupying the same space. (Continuity failure)

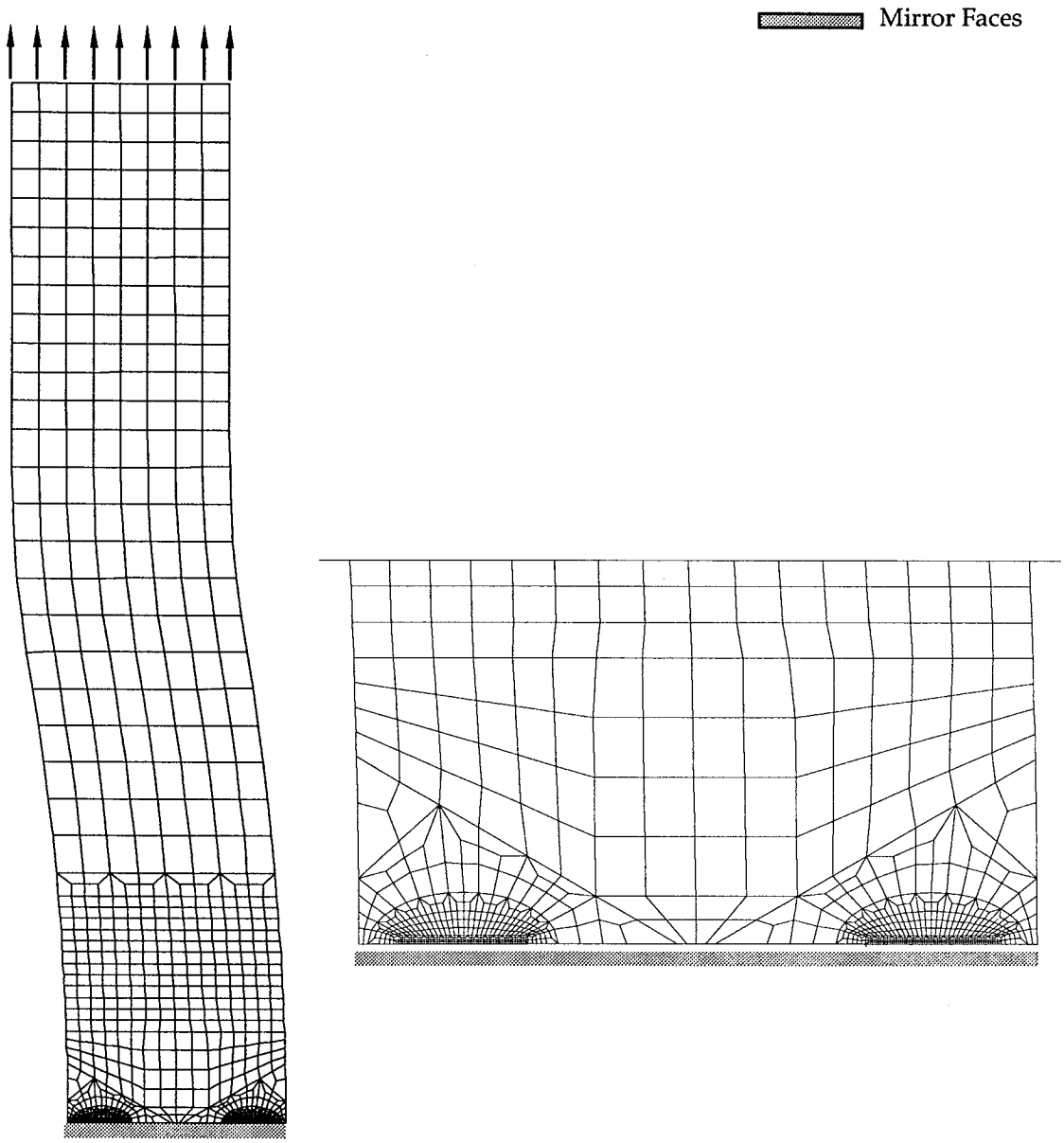

Figure B-1: Center cracked panel tension plus bending specimen model.

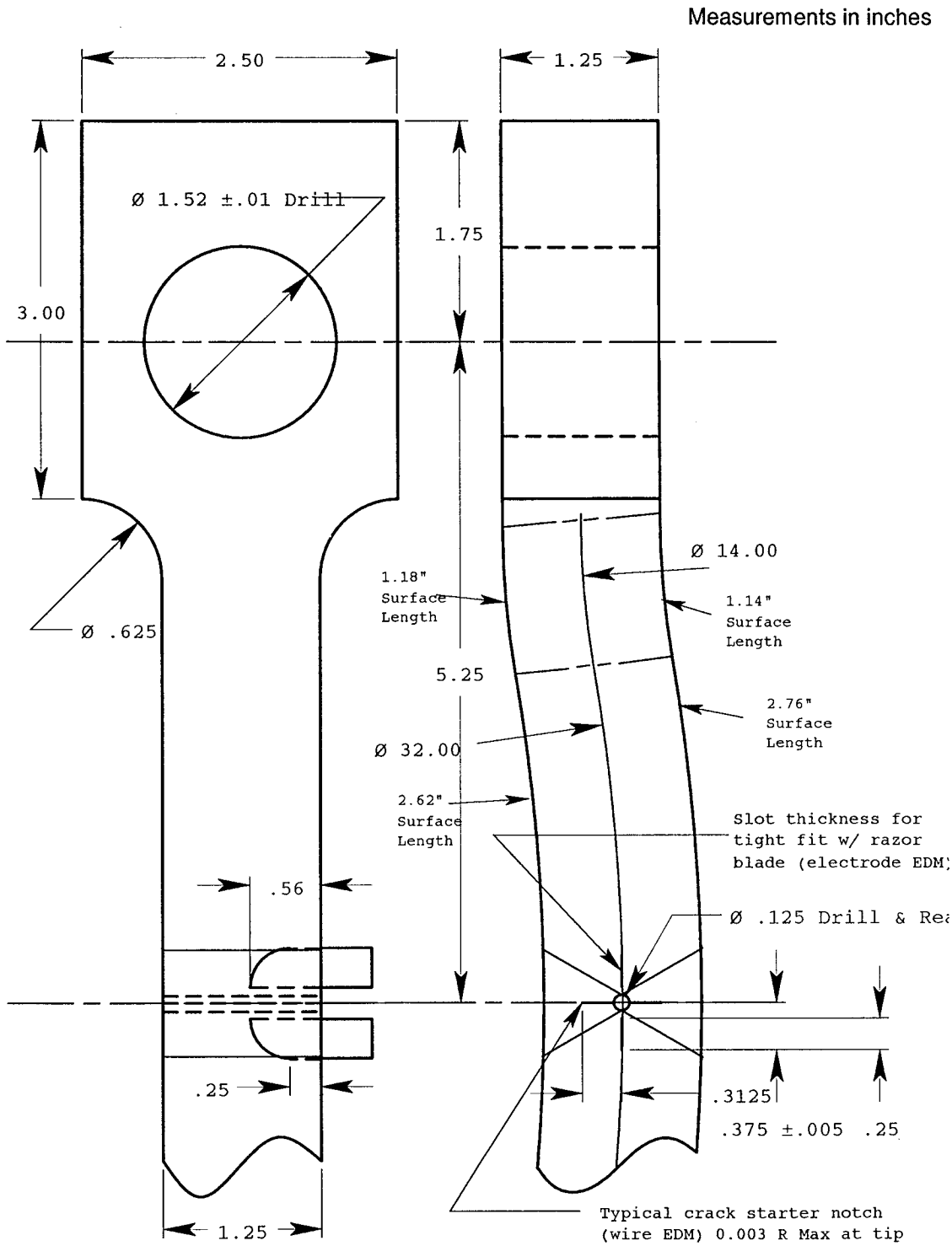

Figure B-2: Center cracked panel tension plus bending specimen.

Appendix C

Warp3D Parameters

Table C-1: Crack growth and weld material parameters for Warp3D model.

Property	Symbol	Value	Units
Young's Modulus	E	30,000,000	psi
Poisson's Ratio	ν	0.30	
Yield Stress	σ_0	69,533	psi
Hardening Modulus	E_T	54,847	psi
Power Law Exponent	n	7.0	
Initial Void Fraction	f_0	0.001	
Gurson-Tvergaard Parameter 1	q_1	1.25	
Gurson-Tvergaard Parameter 2	q_2	1.0	
Gurson-Tvergaard Parameter 3	q_3	1.5625	
Nucleation Parameter 1	f_n	0.04	
Nucleation Parameter 2	s_n	0.1	
Nucleation Parameter 3	e_n	0.3	
Stress Strain Curve		Piecewise Linear	
Reference Strain Rate	ε_{ref}	0.000064	in/sec

Table C-2: Material true stress-strain curves.

	A516-70 Steel		E7018 Weld	
	True Stress	True Strain	True Stress	True Strain
Point 1 (Yield)	50000	0.00167	69533	0.00232
Point 2	56000	0.02000	82064	0.05262
Point 3	68000	0.04000	89926	0.09974
Point 4	84000	0.10000	94595	0.14921
Point 5	93000	0.20000	99509	0.23639
Point 6	80800000	100.0000	5571220	100.00000
Point 7				
Point 8				
Point 9				
Point 10				

The following dynamic analysis parameters were utilized:

1. solution technique lnpcg
2. preconditioner type hughes-winget
3. lnr_pcg conv test res tol 0.01
4. maximum linear iterations 2000
5. stiffness updates before iterations all
6. maximum iterations 10
7. convergence test norm res tol 0.0001 max res load tol 0.001
8. adaptive on
9. extrapolate on
10. consistent q-matrix off
11. bbar stabilization factor 0.05
12. predict on

The following crack growth parameters were utilized:

5. critical porosity 0.15
6. type of crack growth element_extinction
7. force release type traction-separation
8. cell height 0.004
9. crack plane normal y coordinate 0.0
10. release fraction 0.1